The Tapes complex (Nico Pérez Terrane, Uruguay): Constraining the mesoproterozoic evolution of the Río de la Plata Craton

Claudio Gaucher, Robert Frei, Lucía Samaniego, Thomas M. Will, Farid Chemale, María Florencia Gargiulo, Daniel Poiré, Xiaoxiao Ling, Xian-Hua Li, Q.-L. Li

PII: S0895-9811(20)30449-1

DOI: https://doi.org/10.1016/j.jsames.2020.102906

Reference: SAMES 102906

To appear in: *Journal of South American Earth Sciences*

Received Date: 24 August 2020

Revised Date: 14 September 2020

Accepted Date: 15 September 2020

Please cite this article as: Gaucher, C., Frei, R., Samaniego, Lucí., Will, T.M., Chemale, F., Gargiulo, Marí.Florencia., Poiré, D., Ling, X., Li, X.-H., Li, Q.-L., The Tapes complex (Nico Pérez Terrane, Uruguay): Constraining the mesoproterozoic evolution of the Río de la Plata Craton, *Journal of South American Earth Sciences* (2020), doi: https://doi.org/10.1016/j.jsames.2020.102906.

CRediT author statement

Claudio Gaucher: Conceptualization, Methodology, Investigation, Writing-original draft, review & editing, Visualization, Supervision, Funding acquisition. **Robert Frei**: Investigation, Formal analysis, Resources, Writing-original draft, review & editing, Funding acquisition. **Lucía Samaniego**: Investigation, Formal analysis, Writing-original draft, Visualization. **Thomas M. Will**: Investigation, Formal analysis, Resources, Writing-original draft, review & editing, Funding acquisition. **Farid Chemale Jr.**: Investigation, Formal analysis, Writing-original draft. **María Florencia Gargiulo**: Investigation. **Daniel Poiré**: Investigation, Resources. **Xiaoxiao Ling**: Investigation, Resources, Formal analysis. **Xian-Hua Li**: Investigation, Formal analysis. **Qiu-Li Li**: Investigation, Formal analysis.

Dr. Claudio Gaucher

The Tapes Complex (Nico Pérez Terrane, Uruguay): constraining the Mesoproterozoic evolution of the Río de la Plata Craton

Claudio Gaucher[1*], Robert Frei[2], Lucía Samaniego[3,1], Thomas M. Will[4], Farid Chemale Jr. [5], María Florencia Gargiulo[6], Daniel Poiré[7], Xiaoxiao Ling[8]; Xian-Hua Li[8]; Q-L Li[8]

[1] *Instituto de Ciencias Geológicas, Facultad de Ciencias, Universidad de la República, Iguá 4225, 11400 Montevideo, Uruguay*

[2]*Department of Geosciences and Natural Resource Management, University of Copenhagen, Øster Voldgade 10, 1350 Copenhagen K, Denmark.*

[3] *Centro Regional para la Gestión de Aguas Subterráneas (CeReGAS), Rondeau 1665, 11100 Montevideo, Uruguay*

[4]*Institut für Geographie und Geologie der Universität Würzburg, Am Hubland, 97074 Würzburg, Germany.*

[5]*Universidade do Vale do Rio dos Sinos (UNISINOS), São Leopoldo (RS), Brazil*

[6]*Instituto Geológico del Sur (INGEOSUR-UNS-CONICET), Departamento de Geología, Universidad Nacional del Sur, Bahía Blanca, Argentina*

[7]*Centro de Investigaciones Geológicas – CONICET – FCNyM (UNLP), Diagonal 113 N°275, La Plata, Argentina*

[8]*State Key Laboratory of Lithospheric Evolution, Institute of Geology and Geophysics, Chinese Academy of Sciences, Beijing 100029, China*

**Corresponding author, e-mail: gaucher@chasque.net*

ABSTRACT

The Tapes Complex crops out in the southeastern Nico Pérez Terrane (NPT) of the Río de la Plata Craton and forms part of a NE-trending Mesoproterozoic belt together with the Calymmian (1.48-1.43 Ga) Parque UTE and Mina Verdún groups. The complex is characterized by interbedded/tectonically interleaved metasedimentary (mainly siliciclastic) and metaultramafic rocks, with subordinate intercalations of metabasites, carbonate and chert, all metamorphosed in the greenschist facies. The age of the Tapes Complex is constrained by: (i) a U-Pb SIMS age of 1360±12 Ma for the youngest detrital zircon, (ii) the K-Ar age of 1253±32 Ma for synkinematic muscovite of the Zapicán thrust, which affects the unit, and (iii) an Sm-Nd isochronic age of 1403±150 Ma for ultramafic and mafic rocks. The intruding Tapes Chico Syenite yielded a much younger U-Pb SIMS age of 601±5 Ma, associated with Brasiliano-Pan African tectonism, negative εHf values (mean=-31), $\delta^{18}O$ zircon ratios ranging between 5.45

and 6.68 ‰ V-SMOW and inherited zircons dated at 1774-1756 Ma. The best preserved mafic and ultramafic samples yielded Nd model ages (T_{DM}) between 1.55 and 1.68 Ga, close to the assumed crystallization age, and positive εNd(t). Nd model ages of metasedimentary vary between 1.8 and 3.1 Ga, which is interpreted as reflecting two contrasting sources: Archean units of the NPT and Mesoproterozoic mafic and ultramafic rocks, including fragments of oceanic crust. Chondrite-normalized REE patterns of metasedimentary rocks are characterized by LREE enrichment and lack of an Eu anomaly, similar to REE patterns of co-occurring metabasalts. High MgO concentrations, high Cr/V and low Y/Ni and Th/Sc ratios imply the involvement of ultramafic rocks in the source area, which is also supported by whole-rock Pb isotope data. A geodynamic evolution is envisaged, from an extensional tectonic setting between 1.48-1.43 Ga (rift or retroarc basin) into a compressional, retroarc foreland basin at ca. 1.25-1.20 Ga, the latter being probably related to the Kibaran Orogeny in the Namaqua-Natal Belt. It is proposed that the corresponding arc granites and high-grade metamorphic rocks are likely to be found in one of the several terranes in the Namaqua sector of the belt. The Apiaí Terrane (Ribeira Belt, Brazil) shows a similar geological record and evolution as the NPT, and maybe a fragment of the latter displaced to the NW by the Ibaré Shear Zone. The Tapes Complex is a key unit for understanding the assembly of the Río de la Plata and Kalahari cratons, and their incorporation into the Rodinia supercontinent.

Keywords: Rodinia, Grenvillian, Namaqua Belt, Kalahari Craton, Ectasian

1. Introduction

It was formerly thought that the Río de la Plata Craton (RPC) was rather homogeneous and largely composed of Paleoproterozoic rocks mainly formed during the Transamazonian orogenic cycle between 2.2 and 2.0 Ga (e.g. Almeida et al., 1973; Dalla Salda et al., 1988; Hartmann et al., 2002; Oyhantcabal et al., 2011). No Mesoproterozoic rocks were known to occur in the RPC. However, Bossi and Campal (1992) recognized the Nico Pérez Terrane (NPT), which is separated from the remainder of the RPC (Piedra Alta and Tandilia terranes) by the dextral Sarandí del Yí shear zone. According to ^{40}Ar-^{39}Ar data on mafic dykes deformed by the shear zone, accretion of the terrane to the RPC took place between 1370 and 1170 Ma (Teixeira et al., 1999). Bossi and Navarro (2001) report another ^{40}Ar-^{39}Ar age for the deformed dykes showing a significant plateau at 1240±5 Ma. This is corroborated by a K-Ar age of 1253±32 Ma for synkinematic muscovite growth associated with the SE-verging Zapicán Thrust that is exposed to the east of the Sarandí del Yi shear zone in the NPT (Figs. 1-2; Bossi et al., 1998; Bossi and Cingolani, 2009). Archean metatonalites south of Zapicán (Fig. 2), nearby the Zapicán thrust, yielded a U-Pb LA ICP MS zircon emplacement age of 3096±45 Ma and a lower an intercept age of 1252 Ma, suggesting partial Pb loss during the Mesoproterozoic event (Gaucher et al., 2011).

Detrital zircon ages of Ediacaran sandstones deposited at both sides of the Sarandí del Yí shear zone yielded significant Mesoproterozoic zircon populations (Gaucher et al., 2008a; Blanco et al., 2009; Cingolani, 2011), pointing to the occurrence of zircon-bearing rocks of that age in the western RPC, present-day Argentina. Gaucher et al. (2008a) proposed that the Mesoproterozoic Sunsás Belt extended southwards and bounded the RPC to the west, in what they called the "proto-Andean Mesoproterozoic belt". On the basis of the occurrence of several Mesoproterozoic basement inliers in the

Andean Orogen in Argentina (e.g. Fuck et al., 2008), Santos et al. (2008) also postulated the southward continuation of the Sunsás Belt. This implied that Amazonia and the RPC were already a coherent block in Mesoproterozoic times, and represented the counterpart of Laurentia in the Grenvillian Orogeny (Santos et al., 2008; Gaucher et al., 2009, 2011), a configuration that had already been proposed on the basis of paleomagnetic data (Dalziel et al., 2000; Powell et al., 2001; Meert and Lieberman, 2008).

Recent research has shown that the Río de la Plata Craton includes Mesoproterozoic rocks at its eastern and western margins, and also at its core. Gaucher et al. (2011, 2014a) reported U-Pb zircon ages for volcanic rocks in the NPT that range from 1.49 to 1.43 Ga (Calymmian). In addition, two metagabbro plutons were dated by U-Pb SIMS on zircon at 1392±11 Ma and 1193±8 Ma, which intrude the Paleoproterozoic core of the RPC (Santos et al., 2017). These ages are in the same range as the ^{40}Ar-^{39}Ar ages of the mafic dykes that were deformed by the Sarandí del Yí shear zone (Teixeira et al., 1999). Younger, Ediacaran ages reported for mylonites of the Sarandí del Yí Shear Zone indicate that it was reheated and/or reactivated at least once in the Ediacaran to Cambrian (Oriolo et al., 2016). However, this does not invalidate the hypothesis of an earlier Mesoproterozoic accretion of the NPT to the craton, because younger events usually reset older Ar-Ar or Rb-Sr ages of mylonites or their constituent minerals.

In this paper, we present the results of nearly two decades of geological observations in the area, combined with U-Pb, Sm-Nd and lithogeochemical data for the Tapes Complex, a volcanosedimentary succession cropping out in the NPT and mainly composed by ultramafic and siliciclastic rocks showing greenschist-facies metamorphism (Gaucher et al., 2014b). The unit was deposited in the Mesoproterozoic and likely records the generation of oceanic crust prior to the Grenvillian/Kibaran-age

closure of the basin, thus representing a key unit for our understanding of the Mesoproterozic evolution of the RPC. The main aims of this study are to constrain the age, sedimentary provenance and tectonic evolution of the Tapes Complex, and to contribute to the understanding of the Mesoproterozoic evolution of the RPC and its incorporation into the Rodinia supercontinent.

2. Geological setting

The first geological map of the "Tapes greenstones" was presented by Díaz et al. (1990), who described chlorite schists, tremolitites, actinolitites and talc schists as typical lithologies of the unit. Bossi et al. (1998) included the Tapes greenstones in the informal "Grenvillian Metamorphic Complex", to which they tentatively assigned a Mesoproterozoic depositional age. Gaucher et al. (2004) recognized the main outcrop areas and informally named the unit "siliciclastic-ultrabasic succession". Bossi and Schipilov (1998) described serpentinite and talc schist occurrences west of the "Tapes greenstones", in the Zapicán area (Figs. 1-2). Hartmann et al. (2001) proposed the La China Complex to include metatonalites and metagabbros dated by U-Pb SHRIMP between 3.4 and 2.7 Ga. Because of their spatial proximity, they included the metaultramafic rocks of the Zapicán area in the La China Complex, but without providing geochronological evidence of an Archean age.

More recently, Gaucher et al. (2014b) formally defined the Tapes Complex as integral part of the NPT and assigned it to the Ectasian (ca. 1.3 Ga). These authors reported the occurrence of serpentinites, tremolitites, chlorite-tremolite schists and talc schists, all of which formed from former ultramafic igneous rocks such as pyroxenite and/or peridotite. Furthermore, the authors also describe various metasedimentary rocks,

133 ranging from quartz-chlorite schist, quartz- and feldspathic metawacke, to subordinate
134 marl, carbonate and chert.

135 All contacts of the Tapes Complex with neighbouring units are tectonic, except for the
136 intruding Tapes Chico Syenite. In the west, Grenvillian, SE-verging thrusts predominate
137 (e.g. Zapicán Thrust). In the eastern NPT, late Ediacaran-Cambrian, NW-verging thrusts
138 with a significant transcurrent component are dominant (e.g. Cerro Partido Thrust,
139 Puntas del Pan de Azúcar Lineament: Figs. 1-2). It is conceivable, that these lineaments
140 reactivated older Mesoproterozoic thrusts during the late Neoproterozoic-Cambrian
141 final stages of the Brasiliano-Pan African orogeny, yet with the opposite sense-of-shear
142 and vergence. The basement of the complex is unknown, because its lower contact is
143 not exposed. Gaucher et al. (2014b) delineated two main outcrop areas of the Tapes
144 Complex (Figs. 1-2):

145 (a) A southeastern, N30°E-striking belt (Mariscala belt) comprising an area of ca. 300
146 km^2 and extending from just northeast of Minas to the town of Colón in the NE. This
147 belt is intruded by Neoproterozoic and Cretaceous plutons and dissected by NE- and
148 subordinate EW-trending faults, the most important of which is the NW-verging Cerro
149 Partido Thrust (Díaz et al., 1990; Gaucher et al., 2004; Fig. 2). These faults determine
150 four outcrops areas, from SW to NE (Fig. 2): Arroyo Perdido, Mariscala, Arroyo Tapes
151 and Colón (Gaucher et al., 2014b). The outcrop area of the Tapes Complex is confined
152 by the sinistral Puntas del Pan de Azúcar Lineament to the E (Fig. 1A-B, Oyhantcabal et
153 al., 2001; Gaucher et al., 2004), and by Cretaceous rift basins to the N and S.

154 (b) A northwestern, N70°E-striking belt (Zapicán belt, Fig. 2) with ca. 60 km^2 of
155 exposure is separated from the southeastern belt rock units belonging to the Archean La
156 China Complex and the overlying sedimentary cover of Neoarchean to Neoproterozoic

157 age (Hartmann et al., 2001). This segment of the Tapes Complex is limited to the NW
158 by the SE-verging, 1253±32 Ma Zapicán Thrust (Bossi et al., 1998; Bossi and
159 Cingolani, 2009; Fig. 2), along which Archean rocks of the La China Complex override
160 the Tapes Complex.

161 Both outcrop areas are lithologically very similar and the rocks were metamorphosed up
162 to the greenschist-facies conditions. The only difference is an overprint in the Mariscala
163 belt of late Brasiliano deformation associated with the sinistral Sierra Ballena Shear
164 Zone (Figs. 1-2). Thus, Gaucher et al. (2014b) considered the assignment of the Zapicán
165 belt to the La China Complex (Hartmann et al., 2001) as unwarranted because the latter
166 unit is mainly composed of Archean plutonic rocks metamorphosed up to amphibolite
167 facies conditions, which were not reached in the Zapicán area. Furthermore, as will be
168 shown below, the age of the Tapes Complex is over 2 Gyr younger than the La China
169 Complex.

170 Other Mesoproterozoic units of the Nico Pérez Terrane are the Parque UTE Group
171 (PUG) and Mina Verdún Group (MVG, Poiré et al., 2005; Chiglino et al., 2010;
172 Gaucher et al., 2011; Poiré, 2014), which occur to the SW of the Tapes Complex (Fig.
173 1A). These units were previously assigned to the Neoproterozoic and grouped under the
174 now obsolete terms "Lavalleja Group or Complex"and "Fuente del Puma Formation or
175 Group" (e.g. Bossi, 1966; Midot, 1984; Bossi et al., 1998; Sánchez Bettucci and Ramos,
176 1999; Oyhantçabal et al., 2001; see Chiglino et al., 2010 and Gaucher et al., 2014a for a
177 full discussion). Parque UTE and Mina Verdún groups are characterized by interbedded
178 volcanic rocks, carbonates and shales that were metamorphosed up to greenschist facies
179 conditions (Midot, 1984; Chiglino et al., 2010). Metabasalts and metagabbros occur at
180 the base of the PUG and were dated by U-Pb on zircon at 1492±4 Ma (Oyhantçabal et
181 al., 2005). The metabasic rocks are interbedded at the top with rhyolitic ignimbrites and

lapilli-tuffs, which yielded an U-Pb SIMS zircon age of 1462±4 Ma (Gaucher et al., 2014a). Acid volcanic rocks are mainly rhyolite and acid tuff and up to 300 m thick. These rocks predominantly occur at the top of the PUG and base of the MVG, and yielded U-Pb zircon ages of 1429±21 Ma and 1433±6 Ma, respectively (Oyhantçabal et al., 2005; Gaucher et al., 2011). Because of these age data and similar $\delta^{13}C$ curves for the carbonates, Gaucher et al. (2011) proposed that deposition of the MVG immediately postdates that of the PUG, and that both units were deposited in the same basin.

The contact between the Parque UTE and Mina Verdún groups and the Tapes Complex is tectonic, and no sedimentary contact has been observed so far. However, recent airborne geophysical surveys (Fig. 1B, DINAMIGE, 2015) strongly suggest a continuity of geological structures between both areas. Low-K, low-gamma-ray intensity ("total-count radiometry") anomalies coupled with magnetometric anomalies characterize a NE-trending band, 10 km wide by 100 km long, which includes the outcrop areas of the Mesoproterozoic units (Fig. 1B). The low-K anomalies are easily explained by the abundance of thick metabasic rocks and carbonates, characterized by low K_2O values between 0.1 and 0.9 % (mean=0.5%) for the metabasalts (Mallmann et al., 2007) and between 0.1 and 1.5% (mean=0.45%) for the carbonates (Chiglino, 2008). In the Tapes Complex, thick bands of metaultramafic rocks occur, which yielded very low K_2O values <0.05% (Bossi and Schipilov, 2007; Table 1). The magnetometric anomalies related to the mafic and ultramafic rocks of the PUG and Tapes Complex are caused by disseminated magnetite in these rocks. The continuity of the low-K anomalies is interpreted as indicating an uninterrupted, NE-trending Mesoproterozoic belt that includes the PUG and MVG in the SW and the Tapes Complex in the NE. At its southwestern termination against the Sarandí del Yí shear zone, the belt is folded (Road Nr. 81 synform sensu Midot, 1984). This is here interpreted as a drag folding that

formed during the main, dextral movement along the fault (Fig. 1C) at ca.1.25 Ga (e.g. Bossi and Cingolani, 2009). A K-Ar whole rock age of 1208±10 Ma of a metabasic rock close to the fault (Fig. 1C; Gómez Rifas, 1995) is consistent with a Mesoproterozoic tectonothermal event affecting the region. The crystallization age of these PUG metabasic rocks has been recently constrained by a zircon U-Pb LA ICP-MS age of 1479±4 Ma (Oriolo et al., 2019). Pb-Pb ages on galena from deposits hosted in the PUG also suggest metamorphism and deformation around 1.25 Ga (Bossi and Navarro, 2001; see section 8.1).

The Tapes Chico Syenite is important to constrain the depositional age of the Tapes Complex, because it shows clear intrusive relationships with the supracrustal units of the latter unit at its northern edge (Figs.1A-B, 2A). The pluton was mapped by Díaz et al. (1990) and named "Tapes Chico Granite". As will be shown below, despite the occurrence of syenogranite, the most common lithology is quartz-syenite; therefore we propose the name " Tapes Chico Syenite" instead. It is bounded to the NW by the Cerro Partido Thrust, and to the south by a secondary, N-verging thrust fault (Fig. 2) which overthrusts muscovite-bearing quartzite and chlorite schist (Cerro del Águila) onto the pluton (Díaz et al., 1990; Samaniego and García, 2013). To the east, the Tapes Chico Syenite is in contact with Cretaceous alkaline rocks of the Valle Chico Complex (ca. 130 Ma, Cernuschi et al., 2015).

3. Materials and methods

3.1. Petrography

A total of 128 petrographic thin sections (30 μm thick) of metasedimentary, metaultramafic and metabasic rocks were carried out using conventional techniques (Humphries, 1994) at the laboratories of the Facultad de Ciencias (Montevideo, Uruguay) and Centro Universitario Regional Este (CURE, Treinta y Tres, Uruguay). Thin sections were analyzed with a Leica DMLP polarizing microscope and documented with a Leica DFC 290HD digital camera and corresponding LAS software. Quantification of mineralogical composition was carried out using Leica Phase Expert software and by point counting (>300 points/section) for minerals that could not be distinguished on the basis of a different colour.

X-Ray diffractometry (XRD) analyses were carried out at the Centro de Investigaciones Geológicas (La Plata, Argentina) on 9 metaultramafic and metasedimentary rocks, after milling with an agate pestle and mortar to reach 5-10 μm grain size. Analyses were performed directly on the powders ("whole rock"), and also in the clay fraction material (<2 μm) separated using differential settling in water (Moore and Reynolds, 1989). Aliquots of the clay fraction were measured as such ("natural sample"), after glycolation with ethylene glicol vapours and finally after calcination to 550 °C. All samples were measured with a PANalytical X´Pert PRO diffractometer, with Cu lamp (kα=1.5403 Å) operated at 40 mA and 40 kV. The samples were measured from 2 to 40° 2θ, in steps of 0.02°/2 s.

3.2. Lithogeochemistry

Fourteen samples were analyzed at ACTLABS (Ancaster, Canada) using the packages 4LITHO and 4LITHORES, the latter for ultramafic rocks because of the lower detection limit for Rare Earth Elements (REE). Major elements were determined using an Inductively Coupled Plasma-Optical Emission Spectrophotometer (ICP-OES) and trace

253 elements by an Inductively Coupled Plasma-Mass Spectrometer (ICP-MS). In both
254 cases, a fusion bead was prepared with lithium metaborate/tetraborate and then digested
255 in diluted nitric acid. The solution was analyzed by a Perkin Elmer Sciex ELAN 6000,
256 6100 or 9000 ICP-MS. Calibration is performed using ten synthetic calibration
257 standards. A set of 10 certified reference material is run before and after every batch of
258 samples. Duplicates are fused and analyzed every 17 samples. The instrument is
259 recalibrated every 2 trays of samples.

260

261 *3.3. Sm-Nd, Sr and Pb isotopes*

262 Whole-rock samples were analyzed for Sm-Nd, Rb-Sr and Pb isotope ratios at the
263 Department of Geosciences and Natural Resource Management, University of
264 Copenhagen (Denmark). For a number of samples (indicated in Table 2) Sm-Nd
265 analyses were carried out at the Universidade Federal do Rio Grande do Sul, Porto
266 Alegre (Brazil). Rock powders were dissolved using concentrated HNO_3, HCl and HF
267 within Savillex^{TM} beakers on a hotplate at 130°C (reaction time: 72 hours). Sm and Nd
268 were separated after adding a $^{149}Sm/^{150}Nd$ spike, and REE were separated with
269 chromatographic columns charged with 12 ml AG50 W-X 8 (100–200 mesh) cation
270 resin. Subsequently, Sm and Nd were chromatographically separated using columns
271 containing Eichrom's^{TM} LN resin SPS (Part#LN-B25-S). As for Sr, the separation was
272 achieved on conventional cation exchange columns, followed by extraction in miniature
273 columns filled with 200 µL of an intensively precleaned, 50-100 mesh, SrSpec^{TM} resin
274 (Eichrome Inc./Tristchem) and following elution procedures using pure deionized water
275 (Horwitz et al., 1992).

Nd isotopes were determined using a Thermal Ionization Mass Spectrometer (TIMS) VG Sector 54 IT (Copenhagen) and VG Sector 54 (Porto Alegre) set on a static multi-collection mode for Sm isotopes and on a multi-dynamic routine for Nd isotopes, both using a triple Ta–Re–Ta filament assembly. The measured Nd isotope ratios were corrected for mass bias using $^{146}Nd/^{144}Nd = 0.7219$. The mean value of $^{143}Nd/^{144}Nd$ ratios for the JNdi standard runs during the period in which the samples were analyzed was 0.512105 ± 5 (2r; n = 8). Precision for $^{147}Sm/^{144}Nd$ ratios is better than 2% (2r).

1-stage Nd model ages (T_{1DM}^{Nd}) were calculated using a linear $^{143}Nd/^{144}Nd$ evolution of the depleted mantle from $\varepsilon_{Nd} = 0$ at 4600 Ma to a present-day ε_{Nd} of +10 (Goldstein et al., 1984). The following formula was used:

$$T_{1DM}^{Nd} = (1/\lambda) * ln[\{((^{143}Nd/^{144}Nd)_{Sample} - 0.51316)/((^{147}Sm/^{144}Nd)_{Sample} - 0.214)\} + 1],$$

where $\lambda = 6.54 \times 10^{-12}$ yr^{-1} (DePaolo, 1988), 0.51316 is the present-day $^{143}Nd/^{144}Nd$ of the depleted mantle, 0.214 is the $^{147}Sm/^{144}Nd$ depleted mantle (McCulloch and Black, 1984), and $^{143}Nd/^{144}Nd_{Sample}$ and $^{147}Sm/^{144}Nd_{Sample}$ are the measured, respective calculated present-day isotope ratios.

For samples with $^{147}Sm/^{144}Nd > 0.13$ the two-stage model of Keto and Jacobsen (1987) was used for the calculation of Nd model ages, i.e.:

$$T_{2DM}^{Nd} = T_{1DM}^{Nd} - (T_{1DM}^{Nd} - T_{assumed\ age}) * [(f_{CC} - f_{Sample})/(f_{CC} - f_{DM})],$$

where $f = f_{Sm/Nd} = [(^{147}Sm/^{144}Nd)_{Sample}/^{147}Sm/^{144}Nd)^{0}_{CHUR}]-1$. $f_{DM} = 0.08592$ is the value of the depleted mantle reservoir and $f_{CC} = -0.4$ is that of the continental crust according to Goldstein et al. (1984). Initial ε_{Nd} values were calculated from the present-day parameters of the Chondritic Uniform Reservoir (CHUR), assuming $^{147}Sm/^{144}Nd = 0.1967$ and $^{143}Nd/^{144}Nd = 0.512638$.

A Ta_2O_5–H_3PO_4–HF activator solution was used to dissolve Sr in order to load samples onto outgassed 99.98% single Re filaments. Measurements were done at 1250–1300 °C in dynamic multi-collection mode of a VG Sector 54 IT TIMS. The measured $^{87}Sr/^{86}Sr$ ratios were corrected using the offset relative to the certified NIST SRM 987 value of 0.710250.

Pb extraction was performed using conventional glass stem anion exchange columns containing 1 mL of 100–200 mesh Bio-Rad AG 1-8 resin followed by another extraction step in similar miniature glass exchange columns filled with the same type of resin. Pb isotopes were determined in a TIMS (VG Sector 54 IT) run on a static multi-collection mode. Repeated analysis of the NBS 981 standard enabled control fractionation, which was, on average 0.105 ± 0.008% (2r, n = 5) per amu. Total procedural blanks remained below 200 pg Pb.

3.4. U-Pb SIMS zircon geochronology, Hf and O isotopes

Two samples were dated by U-Pb Secondary Ions Mass Spectrometry (SIMS), one at the NordSIM facility in Stockholm (Sweden) and the other at the Institute of Geology and Geophysics, Chinese Academy of Sciences (Beijing). Zircons were separated following standard procedures, involving crushing and milling, panning, heavy-liquid and magnetic separation and hand picking under a stereomicroscope (Strong and Driscoll, 2016).

At the Beijing laboratory, zircon from sample U16-21 was analyzed using a Cameca IMS-1280HR SIMS. The detailed operating and data processing procedures were described by Li et al. (2009). The primary O_2– ion beam has a spot size of about 20×30 μm and an intensity of ca. 8nA. In the secondary ion beam optics, a mass resolution of

c. 7000 (at 50 % peak height) was used to separate Pb+ peaks from isobaric interferences. An electron multiplier was used to measure secondary ion beam intensities by peak jumping mode. Analyses of the unknown zircon grains were interspersed with the Plešovice zircon standard ($^{206}Pb/^{238}U$ age=337 Ma; Sláma et al., 2008). A second zircon standard (Qinghu: Li et al., 2013) was alternately analyzed as an unknown together with the zircon grains to monitor the uncertainties related to the Plešovice standard. A long-term uncertainty of 1.5 % (1σ RSD) for $^{206}Pb/^{238}U$ measurements of the standard zircons was propagated through the unknowns (Li et al., 2010a). Zircon oxygen isotopic compositions were measured with a Cameca IMS-1280 SIMS, following standard procedures (Li et al., 2010b; Tang et al., 2015).

At the NordSIM facility in Stockholm, detrital zircon from sample MAR 27 was analyzed using a Cameca IMS-1270 SIMS following the same procedures described above. Ages were calculated with Isoplot 3.75 (Ludwig, 2012).

In-situ zircon Hf isotopic analysis (sample U16-21) was carried out in Beijing, using a Neptune multi-collector ICP-MS, equipped with a 193 nm laser; the analytical procedures were similar to those described by Wu et al. (2006). The zircon Lu–Hf isotope composition was determined, whenever possible, at the same spot as in the SIMS U–Pb analyses, with a spot size of 65 μm and an 8 Hz pulse frequency.

4. Petrography

Samaniego (2016) described in detail the different lithologies that make up the Tapes Complex (Figs. 3-5). Three different lithologies can be distinguished: hydrated ultramafic (metaultramafic), metabasic and metasedimentary rocks (including

subordinate metamarl and carbonates). It is worth noting that the contacts between these lithologies are generally tectonic; thus no field criteria can be applied to determine their stratigraphic relationships. Except for limited areas, for example, just south of Mariscala (Figs. 1-2), the primary sedimentary structures have been obliterated by deformation and the lack of way-up criteria prevents the determination of the original sequence. Therefore, the term "complex" applied by Gaucher et al. (2014b) is justified.

Metamorphism reached the greenschist facies in the whole Tapes Complex, as shown by the following parageneses (e.g. Bucher and Frey, 1994; Winter, 2001, 2014):

Metaultramafic rocks: serpentine + tremolite + chlorite + magnetite ± talc

Metabasic rocks: actinolite + epidote + clinozoisite + sphene + chlorite + albite ± tremolite

Metapelite and metawacke: quartz + chlorite + tremolite ± epidote ± biotite

Metamarl: calcite + epidote + tremolite ± chlorite ± sphene

Below we describe the petrography of the main rock types, and also of the intruding Tapes Chico Syenite.

4.1. Metaultramafic rocks

The different lithologies in this assemblage can be explained by the metamorphism and/or metasomatism of peridotitic and pyroxenitic protoliths.

Tremolitite is the most common rock, and is typically light green, with nematoblastic texture and crystal size reaching 2 cm. They consist typically of >70 vol. % tremolite, with varying amounts of magnesium chlorite, serpentine and/or talc (Figs. 4A-C).

Relics of olivine (up to 15% in volume) occur in a few samples, mainly in coarse-grained tremolitite (e.g. sample 011021/8, Fig. 4A-B). Tremolite is rarely zoned, with a pleochroic actinolitic core and tremolitic rim. In coarse-grained tremolitites, chlorite (5%) crystallizes in the interstices between centimeter-large crystals of tremolite (95%), perhaps replicating an original cumulate texture (Fig. 4C). Olivine crystals show reaction rims composed of serpentine, chlorite and tremolite (Fig. 4B), which may also be present along crystals fractures (Fig. 4B, Samaniego, 2016).

Tremolitite occurs as meter-scale intercalations between metasedimentary rocks or as bodies a few hundred meters thick and several kilometers long, that are locally associated with regional thrusts (Fig. 2B). The massive tremolitite bodies are interpreted as being derived from a harzburgitic and dunitic protolith (Bossi and Schipilov, 2007; Samaniego, 2016). High Cr and Ni concentrations (up to 1920 and 1730 ppm respectively) and high MgO contents of up to 27 wt. % corroborate an ultramafic protolith.

Serpentinite is composed of serpentine showing interpenetrating texture, talc, tremolite, chlorite, dolomite and magnetite (Fig. 4D). Accessory minerals include spinel and vesuvianite, the latter found near the contact with intrusive granitoids (Samaniego, 2016). Serpentine could be classified as antigorite on the basis of XRD analyses, specifically through the identification of the three strongest peaks at 7.27, 3.62 and 2.53 Å (Whittaker and Zussman, 1956). The rock is typically dark grey, black or dark green in colour. Serpentinites usually occur as pods a few meters wide surrounded by well-developed, concentric zones of talc schist (Figs. 3F, H), tremolitite (not always observed) and dark chloritite (Fig. 4F), the latter possibly representing blackwall alteration (e.g. Karlsen et al., 2000; Winter, 2001, 2014). Pods dip from 45° to vertical

(Fig. 3H) and are arranged in the same manner as the beads of a rosary, which can be followed for several kilometers along strike.

Talc schist has been mined in the area for nearly a century and there are good exposures at several open-pit mines. It is made up of up to 98 vol. % talc (Gaucher et al., 2014b), and variable amounts of magnesian chlorite (penninite or clinochlore; Fig. 4E). Tremolite also occurs, either disseminated or as large porphyroblasts (Fig. 3G) at the expense of talc. The main accessory minerals are hematite (up to 5 vol. %) and rutile (up to 1.5 vol. %). The purest talc schist is generally associated with fault zones, since both high pressures and the circulation of fluids through the fault favor the formation of talc (Pohl, 1992). In many cases it is observed that the talc bodies have a thickness of 1-5 m and are interbedded with chlorite schist (metapelite) and metawacke (Fig. 2B), possibly indicating a volcanic or subvolcanic (i.e. sills) origin for the protolith.

The protolith of the talc schist must have been an ultramafic rock, because of the very high magnesium contents (27-32% MgO, Table 1) and high concentrations of Cr (up to 2430 ppm, Table 1) and Ni (up to 3280 ppm: Gaucher et al., 2014b). Talc pods typically preserve relicts of serpentinite inside, a common feature of ultramafic rock assemblages (e.g. Karlsen et al., 2000). Thus, an ultramafic protolith and its hydrothermal alteration at probably low temperatures explain the genesis of the talc schists.

Chlorite-tremolite-talc schist is quite common and may grade into the pure end-members: tremolitite and talc schist. The main difference from sedimentary chlorite schists (metapelite) is the absence of quartz and feldspars, and the abundance of tremolite and/or talc, which may comprise up to 30-50 vol. % of the rock. It is clear that chlorite-tremolite-talc schist was formed at the expense of ultramafic rocks, as

suggested by the absence of quartz, MgO contents of up to 32 wt. % and very high Ni concentrations (>2000 ppm, Table 1).

4.2. Metabasic rocks

Metabasic rocks are comparatively rare in the Tapes Complex. They are grano- to nematoblastic, poorly foliated rocks characteristically composed of actinolite, tremolite, epidote, clinozoisite, sphene, chlorite and albite (Figs. 4G-H). At point CPA 80 (Fig. 2) a 2m-thick actinolitite intercalation between metasedimentary units occurs, which is made up of 57 vol. % actinolite, 43 vol. % chlorite and trace amounts of tremolite and rutile. The observed parageneses are typical of greenschist-facies metabasic rocks (e.g. Winter, 2014). Geochemical data imply a basaltic protolith (see below).

4.3. Metasedimentary rocks

The most common metasedimentary rocks of the Tapes Complex are siliciclastic: metawackes and quartz-chlorite schists. The latter rock type should not be confused with the chlorite-tremolite-talc schist (see above) that formed from an ultramafic precursor rock. Subordinate carbonate rocks occur in the form of limestone and metamarl.

Meta(grey)wacke is very common, yellowish or orange in outcrop (greenish grey or green when fresh: Fig. 3B) and has a banded appearance. Size grading into metapelite is observed in the least deformed areas (Fig. 3B). *Quartz-metawacke* contains more or less elongated (stretched) clasts of polycrystalline quartz (49-38 vol. %) that occur in a lepidoblastic matrix of chlorite (49-62 vol. %). Well-rounded and undeformed

orthoclase clasts are also present. In one sample, granitic lithoclasts were observed. Accessory minerals include hematite (up to 2 vol. %) and rutile (up to 1 vol. %). *Feldspathic metagreywacke* also occurs and is made up of plagioclase, orthoclase and quartz clasts in a chlorite-carbonate matrix. Sample MAR 27 (=080204/3), which was used for U-Pb zircon dating, is composed of 30 vol. % plagioclase clasts and plagioclase-bearing (basic) lithoclasts that are up to 2 mm in diameter, 60 vol. % chlorite + quartz matrix, 7 vol. % epidote and 3 vol. % sphene + opaque minerals (Fig. 5A-B). To the south of Mariscala, *lithic metagraywacke* occurs, which contain well-preserved ophitic basalt clasts (Fig. 5C-D), with plagioclase laths surrounded by large epidote crystals. Normal size grading in beds 5-20 cm thick is observed, suggesting that the Tapes metagreywackes are of turbiditic origin, as postulated for the majority of these rocks elsewhere (e.g. Pettijohn et al., 1987; Tucker, 2001). Stratabound pyrite is locally abundant, suggesting an euxinic depositional environment.

Quartz-chlorite schist is the most abundant metasedimentary rock. The rocks are green and well foliated (Fig. 3A), showing lepidoblastic texture under the microscope. The main component (95-45 vol. %) is magnesian chlorite (penninite). Quartz (5-43 vol. %) is fine-grained and occurs mainly as mm-thick laminae. Accessory minerals include magnetite, hematite and rutile and, less commonly, tremolite and talc (up to 4 vol. % and 2.5 vol. % respectively). According to composition and texture, the protoliths are interpreted as pelites and cherts. Outcrops to the south of Mariscala preserve the original (sedimentary) lamination (Figs. 3D, 5E-F). Two such well-preserved metapelite samples yielded modal compositions of: 56 vol. % chlorite, 34 vol. % quartz and 10 vol. % magnetite (sample MAR 52D), and 51 vol. % chlorite, 43 vol. % quartz and 7 vol. % magnetite (sample MAR 52E). These rocks are interbedded there with metamarl (see below).

Metamarl (Fig. 3E, 5G) is composed of 40-55 vol. % fine-grained calcite (100-150 μm), 5-30 vol. % epidote (clinozoisite), 10-30 vol. % quartz, 7-20 vol. % tremolite and lesser amounts of chlorite, feldspar clasts and sphene. Metamarl occurs either as single beds up to a couple of meters in thickness or, more commonly, as marl-pelite rhythmites (Fig. 3E). In the latter, cm- to mm-thick laminae of metamarl alternate with metapelite (mainly quartz-chlorite schist), indicating a quiet depositional environment below wave-base. This is corroborated by high organic matter contents and disseminated pyrite in the metapelites, suggesting anoxic conditions.

Limestone is a subordinate component of the Tapes Complex, but in the Mariscala area reaches 200 m in thickness. The rocks are dark grey and fine-grained, showing dm- to cm-thick bedding. Their modal composition is 80 vol, % calcite (grain size: 100 μm), 15 vol. % tremolite and 5 vol. % quartz.

Chert occurs as mm- to dm-thick intercalations in metapelite or as several meter-thick beds. Microscopically, they are composed of microcrystalline quartz. In a few outcrops, stratabound pyrite occurs (Fig. 3C), suggesting euxinic depositional conditions.

4.4. Tapes Chico Syenite

This pluton is characterized by isotropic, coarse grained and undeformed rocks, except for minor cataclastic rocks faults (Fig. 6A-B). Both quartz syenite (the most common lithology) and syenogranite (Fig. 6E) have been observed, quartz contents ranging between 13-26 vol. %. The rocks are rather homogeneous, porphyritic, with phenocrysts of up to 5 cm long (Fig. 6A) composed mainly of perthitic orthoclase, microcline and less commonly of plagioclase with oscillatory zoning (Fig. 6 D). Mafic minerals make

up between 10 and 17 vol %, and are typically hornblende and green biotite. Plagioclase is consistently oligoclase and its content varies between 13 and 21 vol %. Sphene, always associated with amphibole, is ubiquitous as an accessory mineral and reaches 1.5 % in volume (Fig. 6F). At the contact with supracrustals of the Tapes Complex, the Tapes Chico Syenite develops a chilled margin with subvolcanic rocks of trachytic composition and texture, characterized by elongate phenocrysts of alkali feldspar in a fine-grained, greenish matrix. Xenoliths of mafic and ultramafic rocks occur in the pluton (Fig. 6B).

U16-21 (site MAR 51, Fig. 6), is a coarse-grained, porphyric syenite, which was used for zircon U-Pb SIMS age dating. The syenite is unmetamorphosed and consists of cm-sized perthitic K-feldspar phenocrysts (46 vol. % orthoclase and 18 vol. % microcline), plagioclase (13 vol. % oligoclase) with oscillatory zoning, green biotite (3 vol. %), calcic amphibole (9 vol. %) and quartz (11 vol. %) with undulose extinction. Sphene, minor opaque phases and zircon are accessory phases. Sphene is closely associated with amphibole and either occurs within amphibole or at its grain boundaries.

In accordance with its modal composition, the sample plots in the trachyte field in the total alkali versus SiO_2 (TAS) classification diagram (Fig. 7G). In the molar $Al_2O_3/(CaO+Na_2O+K_2O)$ versus molar $Al_2O_3/(Na_2O+K_2O)$ diagram (Shand, 1943), the sample plots in the metaluminous field.

5. Whole-rock geochemistry

Except for the pilot studies of Bossi and Schipilov (2007) and Gaucher et al. (2014b; Table 1) the geochemistry of metaultramafic rocks of the Tapes Complex has not been studied in detail so far. Our new ICP data allow a much better characterization of both

metaultramafic and metasedimentary rocks. Furthermore, two samples yielded a composition suggesting a basaltic protolith, which was previously unknown for the Tapes Complex.

5.1. Metasedimentary rocks

As expected, metasedimentary rocks have much lower MgO values (<11.2 wt. %, mean=6.9 wt. %), higher Na_2O+K_2O (up to 5.5 wt. %, mean=3.4 wt. %) and higher Al_2O_3 concentrations (mean=13.5 wt. %) than the associated metaultramafic rocks (Fig. 7). Greywackes exhibit high Na_2O concentrations between 3.2 and 4.1 wt. %, which are most likely the result of the high content of albitic feldspar (Pettijohn et al., 1987). In addition, metasedimentary rocks are characterized by lower Cr (<540 ppm, mean=210 ppm) and Ni (<600 ppm, mean=176 ppm) concentrations and higher V values (up to 183 ppm, mean=129 ppm) compared to metaultramafic rocks.

REE+Y concentrations compared to PAAS (Post Archean Australian Shale, Taylor and McLennan, 1985) are similar for all clastic rocks (metapelites and metawackes), exhibiting strong positive Eu, negative Ce and slightly negative Y anomalies (Fig. 8A). Metamarl sample MAR 22 shows no Eu anomaly, a negative Ce anomaly and a strong, positive Y anomaly. Not surprisingly, the metamarl REE+Y values are the closest to modern seawater (Alibo and Nozaki, 1999), including heavy REE (HREE) enrichment relative to light REE (LREE), Y and Ce anomalies (Fig. 8A). It is worth noting that clastic rocks of the Tapes Complex (black lines in Figs. 8A-B) yield a REE+Y distribution that closely resembles that of co-occurring metabasites (green lines in Figs. 8A-B), including a large, positive Eu anomaly when normalized against PAAS (Fig. 8A, samples 080204/6 and MAR 44b). Chondrite-normalized REE patterns of

metasedimentary rocks (Fig. 8B) exhibit compositions bracketed between that of E-MORB and OIB basalts, with moderate to strong LREE enrichment, which increases in coarser-grained rocks (metagreywackes). No significant Eu anomaly is observed, and HREEs present a flat distribution.

Low average Th (2.0 ppm) and U (0.4 ppm) concentrations in siliciclastic metasedimentary rocks are more than 5 times lower than the UCC (Upper Continental Crust) average of 10.7 and 2.8 ppm, respectively (McLennan et al., 2006). Th/U ratios range between 4 and 6 (mean=5.2), near or slightly above the average UCC composition (McLennan, 1989)

Th/Sc varies between 0.03 and 0.78 (mean=0.25), lower than the UCC value of 0.78 (McLennan et al., 2006) and similar to active margin turbidite ratios (McLennan et al., 1993). Sc concentrations reach 22 ppm, and except for one sample all exceed the UCC mean of 11 ppm, showing the influence of a less evolved source.

Zr/Sc ranges between 2.5 and 20.5 (mean=9.7), again similar to active margin turbidites and indicating a low degree of sedimentary reworking (McLennan et al., 1993), in line with the available petrographic evidence for sandstones (immature, feldspathic greywackes). In the Th-Sc-Zr/10 and Th-Co-Zr/10 diagram of Bhatia and Crook (1986), samples plot within or near the ocean island arc field (see Fig. 16A), probably due to a mafic/ultramafic source.

Mean Cr/V and Y/Ni ratios equal 1.7 and 0.35 and hint at the influence of a mafic/ ultramafic source (McLennan et al., 1993). A high average MgO concentration of 6.5 wt. % (maximum=11.2 wt. %), several times the mean shale values (Hu and Gao, 2008) also points in this direction.

The Chemical Index of Alteration (CIA: Nesbitt and Young, 1982) was calculated for four samples (metapelite and metawacke) using the correction proposed by McLennan (1993) for CaO*. The obtained values fall within a narrow range of 66-75 (mean=69), indicating little weathering (e.g. Bahlburg and Dobrzinski, 2011).

5.2. Metaultramafic and metabasic rocks

Metaultramafic rocks have high MgO concentrations between 21.4 and 35.1 wt. % (mean=28.3 wt. %; Table 1, Fig. 7) and silica concentrations of 38.4 to 57.4 wt. % (Fig. 7). Al_2O_3 concentrations are very variable between 0.27 and 12.8 wt. % (mean=3.55 wt. %), the highest values were measured for chlorite schists. Total iron ranges between 5.4 and 15.9 wt. % (mean=9.0 wt. %); the highest concentrations were observed in the Zapicán area.

High Cr (up to 1920 ppm, mean=954 ppm) and Ni values (up to 2570 ppm, mean=1804 ppm) were determined. Chloritic talc-schist samples analyzed by Gaucher et al. (2014b) yielded the highest Cr and Ni concentrations of 2430 ppm and 3280 ppm, respectively (Table 1). Chondrite-normalized REE distribution of metaultramafic rocks is characterized by LREE enrichment, a negative Eu anomaly and negative or no Ce anomaly (Fig. 8C-D). Whereas HREE show near-chondritic concentrations, LREE are enriched 2 to 10-fold (one sample up to 37-fold) compared to chondritic values (Fig. 8C-D). Similar REE distributions have been reported for different types of ultramafic and metaultramafic rocks, including ocean floor peridotites, serpentinized harzburgites and dunites, and metakomatiites (Frey et al., 1971; Frey, 1984; Remus et al., 1993). In the study of Deschamps et al. (2013), subducted serpentinites show REE patterns similar to that reported here for the Tapes Complex. Other characteristics of subducted

582 serpentinites (Deschamps et al., 2013) found in the Tapes serpentinites are Yb and Ti
583 enrichment and lower loss on ignition (LOI <11.2 %).

584 Two metabasite samples analyzed plot in the basalt field in the total alkali vs silica
585 (TAS) diagram (Fig. 7G) and in the Zr/Ti vs Nb/Y diagram of Winchester and Floyd
586 (1977, modified by Pearce, 1996, not shown). These rocks can be distinguished from
587 ultramafic rocks by lower MgO values (up to 10 wt. %) and higher concentrations of
588 Al_2O_3 (6.3-16.8 wt. %), CaO (14.3-15.9 wt. %), Fe_2O_3 (8.3-16.8 wt. %) and Na_2O
589 (0.25-1.2 wt. %, see Fig. 7A-F). Cr (70-210 ppm) and Ni (50-80 ppm) concentrations
590 are more than one order of magnitude lower than in metaultramafic rocks. Chondrite-
591 normalized REE distribution shows a marked LREE enrichment and a negative Ce
592 anomaly, which is analogous to samples with ultramafic protolith (Fig. 8C-D). The
593 metabasic rocks have significantly higher REE concentrations than the ultramafic rocks
594 and a positive Eu anomaly (Fig. 8C-D).

595

596 **6. Sm-Nd, Sr and Pb isotopes**

597 *6.1. Sm-Nd isotopes*

598 A total of 34 Sm and Nd whole-rock isotope analyses were carried out on 31 samples of
599 the Tapes Complex, including 16 metaigneous and 15 metasedimentary samples (Table
600 2).

601 Metasedimentary rocks (Fig. 9C-D) yielded Archean to Paleoproterozoic model ages
602 between 3.1 and 1.8 Ga (mean=2.56 Ga), and negative εNd (t) values (for t=1300 Ma)
603 between -21 and -0.6 (mean=-8.7). The youngest model ages (1.8 to 2.3 Ga) and least
604 negative εNd(t) values (-0.6 to -6) correspond to limestone and marl, which are

605 characterized by a smaller, subordinate detrital component and a major chemogenic
606 (seawater) component. Meta(grey)wackes and metapelitic rocks have mainly Archean
607 T_{DM} values (64%) and less commonly (36%) Paleoproterozoic model ages between 2.2
608 and 2.4 Ga.

609 Metaultramafic and metabasic rocks yielded Nd model ages and εNd (t=1400 Ma)
610 values that can be divided into three different groups (Fig. 9A-B): (1) Late
611 Paleoproterozoic-Mesoproterozoic, between 1.55 and 1.68 Ga, with positive εNd (t)
612 between 2.5 and 5 (n=2), (2) Early Paleoproterozoic between 2.41 and 2.46 Ga and
613 εNd(t) consistently around -6 (mean=-6.0, n=5), and (3) Archean, with T_{DM} between 2.6
614 and 3.3 Ga and negative εNd (t) between -6.7 and -17 (mean=-13.9, n=11). Group 1,
615 with the youngest T_{DM}, includes one metaperidotite with olivine relicts, which is the
616 best-preserved ultramafic rock in the Tapes Complex (Fig. 4A-B).

617 Group 2, of 5 mafic and ultramafic samples with T_{DM} consistently between 2.41-2.46
618 Ga and εNd (t) around -6 yield an Sm-Nd isochron of 1403 Ma ± 150 Ma (r=0.998; Fig.
619 10). Despite the relatively large error, the age is here considered geologically significant
620 because it is similar to U-Pb crystallization ages of bimodal volcanism in the PUG in
621 the southern NPT (Gaucher et al., 2011, 2014; Oriolo et al., 2019; see below), and
622 supports a Mesoproterozoic intrusion age of these rocks.

623

624 *6.2. Sr isotopes*

625 A total of 18 samples were analyzed for their $^{87}Sr/^{86}Sr$ ratios: three limestone and marls
626 samples, four metawackes, two metabasic and ten metaultramafic rocks (Fig. 11).

Limestone and marl yielded high $^{87}Sr/^{86}Sr$ values of 0.7125 to 0.7244, which are too high to represent coeval seawater values (e.g. Shields, 2007) and cannot be used for geochronology. The lowest $^{87}Sr/^{86}Sr$ ratios were measured for a metabasic rock (0.7048), a metapelite (0.7057) and a metagreywacke (0.7063, Table 3). The similar Sr isotope ratios of basic and siliciclastic rocks may be explained by derivation of the metawackes from basic volcanic rocks, as also indicated by the REE+Y data and Nd isotopes (see above). This heritage is not surprising as the metagreywackes contain lithoclasts of basic volcanic rocks.

Ultramafic rocks have a large variation in $^{87}Sr/^{86}Sr$ ratios (0.7078 to 0.7518), with most values close to 0.72. These values do neither represent primary (mantle) ratios nor do the measured Sr isotope ratios represent interaction with seawater, given $^{87}Sr/^{86}Sr$ seawater values of ca. 0.7050 for the 1.45-1.30 Ga period (Kuznetsov et al., 2014). Interaction with more radiogenic fluids during metamorphism and hydrothermal alteration is a possible explanation for the high values observed. When plotted in a εNd (t) vs. $^{87}Sr/^{86}Sr$ diagram (Fig. 11A) all samples, regardless of their origin, show decreasing εNd (t) with increasing $^{87}Sr/^{86}Sr$, which can be regarded as an alteration trend during metamorphism and/or metasomatism. Moreover, $^{87}Sr/^{86}Sr$ values of mafic and ultramafic samples increase markedly with decreasing Sr concentrations (Fig. 11B), which has been regarded as the result of enhanced fluid flux during hydrothermal alteration both for mafic/ultramafic rocks (Delacour et al., 2008) and carbonates (Jacobsen and Kaufman, 1999).

6.3. Pb isotopes

650 Pb isotope ratios were determined for 18 samples (Table 3), including metasedimentary,
651 metaultramafic and metabasic rocks. Except for two samples with $\mu > 10$, the majority
652 of samples show $^{206}Pb/^{204}Pb$ values ranging between 16.50 and 19.62, $^{207}Pb/^{204}Pb$ from
653 15.17 to 15.67 and $^{208}Pb/^{204}Pb$ between 36.86 and 41.43.

654 Both metasedimentary and metaigneous samples plot in the lower crust field of the
655 Zartman and Doe (1981) diagram (Fig. 12A-B). The lower crust is characterized by
656 lower U/Pb and μ ($=^{238}U/^{204}Pb$) ratios than the upper crust, leading to lower $^{206}Pb/^{204}Pb$
657 and $^{207}Pb/^{204}Pb$ ratios (Zartman and Doe, 1981). The Tapes Complex igneous samples
658 show a clear lower crustal signature, which could be due to contamination during
659 magma ascent through the crust. Interestingly, metasedimentary samples plot in the
660 same field and show little scatter towards the upper crust field (Fig. 12). The similar Pb
661 isotope composition of metasedimentary and metabasic rocks in combination with
662 similar REE+Y patterns (Fig. 8A), similar εNd (t) and Nd model ages (Fig. 9) and
663 $^{87}Sr/^{86}Sr$ ratios strongly support provenance of the siliciclastic rocks from a source area
664 dominated by basic volcanic rocks.

665 Six basic and ultrabasic samples from both the Mariscala and Zapicán belts define a
666 linear array with a high correlation coefficient (r=0.983) in a $^{207}Pb/^{204}Pb$ vs. $^{206}Pb/^{204}Pb$
667 diagram (Fig. 12C), meaning that they likely derive from the same Pb reservoir and are
668 possibly cogenetic. The calculated μ value for this source is 9.808, which is similar to
669 the average continental crust value of 9.735 (Stacey and Kramers, 1975). The time of
670 separation from their source is indicated by the lower intercept of the regression line
671 with the μ curve at ca. 2.1 Ga.

672

673 **7. U-Pb SIMS zircon geochronology**

We dated two samples by U-Pb SIMS to constrain the age of the Tapes Complex. Sample U16-21, from site MAR 51 to the north of Mariscala (Fig. 2), is a coarse-grained quartz syenite (see above; Fig. 6) of the Tapes Chico Syenite, which intrudes the Tapes Complex. Zircon crystals are euhedral, prismatic and strongly zoned, with Th/U values between 0.70 and 3.14 (mean=1.49). Twelve analyses (cores) determine a concordant age of 601 ± 5 Ma (2σ, 95 % confidence level, Fig. 13), which is interpreted as the crystallization age of the syenite and the minimum age of the Tapes Complex. $\delta^{18}O$ values on zircon range between 5.45 and 6.68 ‰ V-SMOW (Fig. 13, Table 4), with 12 of 13 analyses outside the mantle field of 5.3 ± 0.3 ‰ (Valley et al., 2005). Zircon εHf(t) values vary between -52 and -26, with a mean of -31. Corresponding T_{DM} model ages range between 4.22 and 2.84 Ga, with a mean of 3.09 Ga (Table 4). Two xenocrysts were also dated, which yielded Pb-Pb ages of 1774±10 Ma and 1756±11 Ma, and Archean Hf model ages, which match the crystallization age and model ages of rapakivi granites of the NPT (Mallmann et al., 2007; Oriolo et al., 2019).

A reconnaissance U-Pb detrital zircon study was carried out on sample MAR 27 (Table 4), which is a coarse-grained, epidote-rich, feldspathic metagreywacke (Fig. 5A-B) of the Tapes Complex cropping out just south of Mariscala (Fig. 2). Zircons are scarce and well rounded, showing that they are detrital in nature (Fig. 14). Nine grains yielded concordant U-Pb SIMS ages, the youngest of which is 1360±12 Ma (^{206}Pb-^{238}U, >95% concordant), providing a maximum age constraint for deposition of the metasedimentary rocks of the Tapes Complex. The main population clusters around 1.46 Ga, matching the age of bimodal volcanic rocks of the PUG (Gaucher et al., 2011, 2014a). The oldest concordant analyses yielded ages of 1579±14 Ma and 1624±14 Ma (Fig. 14), which do not match any known units in the NPT or elsewhere in Uruguay. It is worth pointing out that according to Dickinson and Gehrels (2009) the youngest

699 single detrital grain age is compatible with depositional age in >90% of the studied
700 units, and therefore can be confidently used to constrain the maximum depositional age
701 of the Tapes Complex.

702

703 **8. Discussion**

704 *8.1. Age of the Tapes Complex and regional correlations*

705 The age of metagreywackes of the Tapes Complex is constrained between the U-Pb age
706 of the youngest detrital zircon (1360±12 Ma, Fig. 14) and the K-Ar age of the Zapicán
707 Thrust (1253±32 Ma, Bossi and Cingolani, 2009), which cross-cuts the unit. The Sm-
708 Nd isochron of 1403 Ma ± 150 Ma (Fig. 10) obtained for mafic and ultramafic samples
709 of group 2 (Fig. 9) corroborates a Mesoproterozoic, probably Ectasian age for the bulk
710 of the Tapes Complex, in contrast to earlier propositions of a late Neoproterozoic age
711 for the metasedimentary succession. The U-Pb age of the intrusive Tapes Chico Syenite
712 of 601±5 Ma fails to provide a more precise minimum age constraint. However, it
713 shows that the NW-verging Cerro Partido Thrust (Fig. 2) and other subparallel
714 structures are late Ediacaran or early Cambrian in age, because they cross-cut the
715 pluton. Furthermore, $\delta^{18}O$ ratios higher than mantle values (12 of 13 analyses), very
716 negative εHf values and Archean model ages are consistent with a derivation of the
717 magma from partial melting of Archean basement (e.g. La China Complex) and/or
718 metasedimentary units (Tapes Complex?), as shown for I-type granites in Australia
719 (Kemp et al., 2007). A contribution of Statherian rapakivi granites is indicated by
720 inherited ages around 1.75 Ga. The highly enriched Hf isotope composition (Table 4) is
721 typical for melts that experienced substantial crustal assimilation and/or contamination.

722 The question arises if some of the mafic or ultramafic bodies, which in some cases are
723 tectonically interleaved with the metasedimentary rocks of the Tapes Complex, could be
724 older. The PUG farther to the south in the NPT is characterized by bimodal magmatism,
725 including a thick pile of basalts and gabbros (Cañada Espinillo Formation: Chiglino et
726 al., 2010), which according to Midot (1984) reaches 800 m in thickness. The basic rocks
727 were dated by U-Pb LA ICP-MS on zircon at 1482±6 and 1479±4 Ma (Oriolo et al.,
728 2019), and the acid pyroclastic rocks associated with the top of the basic volcanic pile
729 (Nueva Carrara Formation) yielded a U-Pb SIMS zircon age of 1462±4 Ma (Gaucher et
730 al., 2014a). Because of the large uncertainty, our Sm-Nd isochron does not allow us to
731 distinguish between these Calymmian ages and younger, Ectasian ones. Nevertheless,
732 detrital zircon ages show that the 1.48-1.43 Ga volcanic rocks acted as a source of the
733 metagreywackes of the Tapes Complex, and therefore they must pre-date them.
734 Furthermore, ultramafic rocks are very rare in the PUG, with metabasalts and
735 metagabbros dominating the assemblage (Midot, 1984; Sánchez Bettucci and Ramos,
736 1999; Mallmann et al., 2007). The opposite is true in the Tapes Complex, where
737 metaultramafic rocks are the dominant igneous lithology (e.g. Fig. 2B).

738 The metasedimentary succession of the PUG and MVG also differs markedly from that
739 of the Tapes Complex. Whereas in the former units shallow-water, stromatolitic
740 limestone and dolostone dominate the succession (Poiré et al., 2005; Chiglino et al.,
741 2010; Gaucher et al., 2011) the Tapes metasedimentary succession is dominated by
742 immature siliciclastic rocks such as metagreywackes of probable turbiditic origin.
743 Carbonates in the Tapes Complex are very subordinate and were likely deposited in a
744 deeper water environment, as exemplified by marl-pelite rhythmites (Fig. 3E).

745 The metamorphic overprint of the PUG and MVG is constrained by a K-Ar whole rock
746 age of 1208±10 Ma of a metagabbro (Gómez Rifas, 1995), which yielded a U-Pb zircon

crystallization age of 1480 Ma (Oriolo et al., 2019, see above). Bossi and Navarro (2001) presented Pb isotope data for four different galena deposits hosted in the PUG, which we processed using Isoplot (Ludwig, 2012). The analyses define a linear array (an isochron), which intercepts the growth curve at 1.28 Ga. Two analyses (La Oriental and Valencia mines) lie on the Pb growth curve and yielded two-stage Pb-Pb ages (Stacey and Kramers, 1975) of 1267 and 1218 Ma. Taken together, they define an intercept with the growth curve at 1242 Ma (Fig. 15), which is essentially the same as the whole-rock K-Ar age of metagabbros of the PUG and the K-Ar age of synkinematic muscovite of the Zapicán Thrust. It is worth noting that the Valencia Mine galena mineralization is unconformable, occurring as veins that cross-cut the host rocks (Bossi, 1978), showing a post-depositional origin and/or metamorphic remobilization. As for the La Oriental Mine, although the main mineralization is stratabound, Midot (1984) suggests that extensive tectonic remobilization took place, as shown by the occurrence of carbonate-sulfide stockworks. Thus, the Tapes Complex and the PUG and MVG were likely metamorphosed and deformed during the same Mesoproterozoic tectonic event, which is also responsible for mafic dyke deformation west of the Sarandí del Yí Shear Zone (Teixeira et al., 1999).

Summing up, it is clear that the Tapes Complex represents a stratigraphic unit distinctively different from the older PUG and MVG. However, the U-Pb zircon age of acid pyroclastic rocks at the base of the MVG (1433±6 Ma: Gaucher et al., 2011) shows that deposition probably lasted until the end of the Calymmian, which is just 40 Myr older than the maximum possible age of the Tapes Complex. Furthermore, we have shown above that airborne geophysical data support continuity between both units, suggesting that they may have been deposited in the same basin, yet at different times, with the Tapes Complex postdating the other units. The sedimentary provenance and the

isotopic data of metaigneous rocks also support a link between these units (see below). In any case, metamorphism and deformation of all these units took place at 1.20-1.25 Ga, with a second Ediacaran-Cambrian event affecting mainly the eastern outcrops.

8.2. Sedimentary provenance

Nd model ages of metasedimentary rocks show large variability, between late Paleoproterozoic and Mesoarchean. The youngest T_{DM} model ages (1.8 to 2.3 Ga) and least negative εNd(t) values (-0.6 to -6) were determined for carbonate samples, and are interpreted as the result of a reduced detrital input rather than a different source area. The younger model age group of the siliciclastic rocks ranges from ca. 2.3 to 2.4 Ga (Fig. 9D).

The observed model age distribution of the metasedimentary rocks (Fig. 9C-D) is interpreted as the result of the mixing of two different crustal sources of Paleoproterozoic and Archean model ages, respectively. Archean rocks are widespread in the NPT and near the Tapes Complex (Figs. 1-2), and are a potential source of detritus. The La China Complex yielded U-Pb SHRIMP ages between 3.4 and 2.7 Ga (Hartmann et al., 2001; Gaucher et al., 2011), with T_{DM} values of more than 3 Ga and εNd(t) values between -2 and +3 (Mallmann et al., 2007; Gaucher et al., 2010). Thus, these rocks probably represent the older, Archean source area of the Tapes Complex.

The younger source with Paleoproterozoic crustal residence might be the ultramafic rocks of the Tapes Complex and mafic rocks of the PUG. The former yielded model ages as young as 1.55 Ga (group 1) and a significant number of analyses cluster around 2.45 Ga (group 2, Fig. 9). Metabasic rocks of the PUG yielded late Paleoproterozoic

795 T_{DM} model ages between 1.6 and 2.1 Ga (Mallmann et al., 2007). As stated above, a
796 contribution of these magmatic rocks is confirmed by our detrital zircon data, which
797 closely match the crystallization ages of bimodal volcanics of the PUG. Therefore,
798 mixing of these younger sources with the Archean ones can explain the broad range of
799 model ages determined for the Tapes Complex.

800 A basic volcanic to ultramafic source for the Tapes Complex is further indicated by
801 different lines of evidence. Basalt clasts are widespread and well preserved in a number
802 of metagreywacke samples (Fig. 5A-D). PAAS-normalized REE+Y patterns of
803 siliciclastic rocks closely resemble that of associated basic rocks, including a large,
804 positive Eu anomaly (Fig. 8A). Similar, low $^{87}Sr/^{86}Sr$ ratios (0.705-0.706) were
805 measured for a metagreywacke, a metabasic and a metapelitic rock of the Tapes
806 Complex. In the Pb isotope plots (Fig. 12A-B), metasedimentary samples show
807 unradiogenic values similar to samples with ultramafic and/or mafic protoliths.
808 Lithogeochemical data of siliciclastic rocks also support provenance from a less
809 evolved, ophiolitic source, including high MgO concentrations, high Cr/V and low Y/Ni
810 and Th/Sc ratios (McLennan et al., 1993).

811 Thus, if the mafic and ultramafic rocks of the PUG and Tapes Complex were the detrital
812 sources for the metasedimentary rocks of the Tapes Complex, a suitable mechanism
813 must be found to explain the exhumation of rocks that were originally deposited in a
814 marine setting and/or represent slivers of oceanic crust. This will be dealt with in the
815 next section.

816

817 *8.3. Tectonic setting and basin evolution*

The Mesoproterozoic rock record in the NPT begins with bimodal volcanic rocks and thick carbonates of the 1.48-1.43 Ga PUG (Gaucher et al.., 2011 and references therein). Basic volcanic rocks in the unit have a predominantly MORB signature, with a few samples resembling OIB (Sanchez Bettucci et al., 2001; Mallmann et al., 2007; Oriolo et al., 2019). Detrital zircon of sandstones from the PUG yielded 60% Archean and 33% early Paleoproterozoic ages, with the youngest grain some 450 Myr older than the depositional age (Mallmann et al., 2007). Thus, an extensional tectonic environment, maybe a rift setting, seems the most plausible scenario (Gaucher et al., 2014a; Oriolo et al., 2019).

On the other hand, Sanchez Bettucci et al. (2001) pointed out that basalts of the PUG are, compared to MORB, depleted in Cr, Ni, Co, Nb and Ta, significantly enriched in LREE, and have lower Ti/Zr and higher Ti/V and Ti/Sc ratios, which they interpreted as indicating a back arc tectonic setting. According to Poiré et al. (2005) trace element contents in shales of the lower MVG (<1.43 Ga), above the PUG, plot mainly in the field of continental island arc in the Th-Sc-Zr triangular diagram of Bathia and Crook (1986; Fig. 16), which led Poiré et al. (2005) to suggest a back arc setting, probably on the opposite side of the active arc. Therefore, two different models were proposed for the PUG and MVG, but both propose an extensional origin for the basin.

According to Samaniego (2016), two metabasic samples of the Tapes Complex also plot in the MORB field in the Th/Yb vs. Nb/Yb diagram of Pearce (2008), but the data are insufficient to draw any conclusions. The Nd and Pb isotope data of metasedimentary rocks, on the other hand, point at two different sources, one of which must have been a less evolved, possibly ophiolitic source, and the other one were Archean rocks of the NPT. A compressional tectonic setting is necessary to explain the exhumation and erosion of ultramafic rocks, which probably represent obducted oceanic crust, and of

843 marine volcanosedimentary successions (Parque UTE and Mina Verdún groups)
844 deposited some 100 Myr earlier.

845 In the proposed scenario, the deposition of the Tapes Complex was coeval (syntectonic)
846 with the Grenvillian-Namaqua tectonism that affected the NPT at ca. 1.25 Ga. A fast
847 erosion and sedimentation rate is indicated by the immaturity of sandstones and by the
848 low CIA of 69 (average), suggesting little chemical weathering. The ages of detrital
849 zircons analyzed are almost exclusively Mesoproterozoic (Fig. 14), which is consistent
850 with provenance from an active orogen. Nd isotope data, however, show that rocks with
851 Archean crustal residence age also acted as a source. The Archean La China Complex
852 and Cebollatí Group were affected by the 1.25 Ga event, as shown by lower intercepts
853 in U-Pb zircon ages (1252 Ma: Gaucher et al., 2011) and by the Zapicán Thrust
854 affecting these units (Hartmann et al., 2001; Figs. 1-2). Therefore, the source area
855 probably comprised deformed and uplifted Mesoproterozoic rocks (PUG and MVG) as
856 well as older, Archean basement units (Fig. 19).

857 Regarding the position of the Tapes basin in such a compressional setting, it is worth
858 noting that: (1) the highest metamorphic grade observed reaches only greenschist facies,
859 (2) no Mesoproterozoic granitoid intrusions associated with the 1.2 Ga orogenic event
860 are known in the NPT, and (3) a strong strike-slip component is evidenced by the large-
861 scale, dextral Sarandí del Yí shear Zone. To account for these facts, it is necessary to
862 consider that the Tapes Complex was formed during closure and inversion of a back-arc
863 or retroarc basin (sensu Einsele, 2000). A retroarc foreland basin, developed behind an
864 active continental margin (Fig. 19), would better explain the strong influence of nearby
865 Archean rocks, which must have been part of a continental mass in the Calymmian-
866 Ectasian. A transition from an extensional (rift or retroarc) regime into a compressional

basin, possibly a retroarc foreland basin (Einsele, 2000), closer to the magmatic arc, is suggested by the following data (Figs. 16-18):

(a) Whereas pelites of the 1.43 Ga lower MVG plot essentially in the field of continental island arc in the Th-Sc(Co)-Zr diagrams of Bathia and Crook (1986; Poiré et al., 2005), the Tapes Complex pelites and greywackes plot within or very close to the oceanic island arc field (Fig. 16A). This may show that the Tapes Complex was receiving detritus from obducted oceanic crust, the remnants of which occur in the same complex, which was not available as a source for the older units.

(b) Pb isotopes are in line with this assumption for the Tapes Complex, as metasedimentary rocks plot in the unradiogenic lower crust field of Zartman and Doe (1981, Fig. 12).

(c) The presence of an Eu anomaly is a useful proxy for provenance studies, and is expressed as $Eu/Eu^*=Eu_N/[(Sm_N)(Gd_N)]^{1/2}$, where the subscript "N" indicates chondrite-normalized concentrations (Kato et al., 2006). According to Poiré et al. (2005), pelitic rocks of the lower MVG have a marked negative Eu anomaly (Eu/Eu* 0.59-0.67, Fig. 16B). In contrast, Tapes pelites and greywackes do not show this anomaly (mean Eu/Eu*=1.02, range: 0.79-1.22), which according to McLennan et al. (1993) is interpreted as the result of increased detrital input from undifferentiated, possibly mantle-derived materials.

(d) Detrital zircon age spectra for sandstones of the 1.48-1.43 PUG are dominated by Archean (60%) and Paleoproterozoic (40%) ages, the youngest of which yielded an age of 1932±13 Ma (Mallmann et al., 2007), 450 Myr older than the oldest possible depositional age (Fig. 16C). In the ca. 1.3 Ga Tapes Complex, detrital zircon ages shift dramatically toward younger ages (Figs. 15-16C), including a significant population

between 1.48 and 1.43 Ga derived from the PUG and MVG, and the youngest zircon 1.36 Ga. Despite the small number of analyzed zircons, the data unambiguously show a shift to source areas comprising already exhumed Calymmian units (e.g. PUG), more proximal to the magmatic arc and farther away from the Archean cratonic rocks.

Whether the Calymmian volcanosedimentary succession was deposited in a rift or a back arc/retroarc basin is difficult to ascertain with the available data (Fig. 19A_1 and A_2). However, no magmatic arcs in the 1.48-1.40 Ga range are known, neither in southern Africa (e.g. Cornell et al., 2006, Macey et al., 2018) nor Uruguay and nearby areas in South America. In the Namaqua-Natal Belt, the earliest Mesoproterozoic orogenic events start at 1.33 Ga in the Konkiep Terrane (Cornell et al., 2015). The only coeval Calymmian orogen described in South America is located at the southwestern boundary of the Amazon Craton (=Amazonia), some 2000 km to the north of the studied area (Bettencourt et al., 2010; Teixeira et al., 2020). The possible correlations with units in South America and southern Africa will be dealt with in the next two sections.

8.4. Correlations with South American units

8.4.1. Apiaí Terrane (Ribeira Belt)

The Apiaí Terrane is a tectonostratigraphic unit of the southern Ribeira Belt in southeastern Brazil. It is bounded to the southeast by the dextral Lancinha-Cubatão shear zone (Passarelli et al., 2011; Fig. 17B), and it is covered to the northwest by thick deposits of the Paraná Basin (Fig. 17B). The Apiaí Terrane is made up of 1.77-1.75 anorogenic granite, Mesoproterozoic supracrustal successions and Ediacaran granites and siliciclastic units, including glaciogenic diamictites of Gaskiers age (Iporanga Formation: Campanha et al., 2008). Of especial interest here are the Mesoproterozoic

915 units, namely: the 1.49-1.40 Votuverava Group, Água Clara and Betara Formations, the
916 1.20-0.88 Ga Lajeado Group and the 1.0-0.9 Ga Itaiacoca Group (Fuck et al., 2008;
917 Siga Jr. et al., 2011; Campanha et al., 2015).

918 The Votuverava Group is made up of rhythmic metapelite, interpreted as distal
919 turbidites, interbedded with metabasic rocks (Faleiros et al., 2011). The latter yielded U-
920 Pb zircon ages which fall into two groups: (a) Calymmian ages of 1488±4 and 1479±12
921 (Siga Jr. et al., 2011; Campanha et al., 2015), and (b) Ectasian ages of 1299±6 and
922 1279±11 Ma (Campanha et al., 2019). These ages closely match the age of basic
923 magmatism of the PUG (1482±6 to 1462±4 Ma, see above) and the Ectasian age
924 proposed here for the Tapes Complex, including its basic and ultrabasic rocks (1.36-
925 1.25 Ga). As in the PUG, the geochemistry of the Votuverava metabasic rocks points to
926 an extensional setting (Siga Jr. et al., 2011), possibly a back-arc basin (Faleiros et al.,
927 2011; Campanha et al., 2015, 2019). Furthermore, a tectonothermal overprint between
928 1283±28 and 1120±70 Ma in the Apiaí Terrane is recognized in Ar-Ar and Rb-Sr ages
929 (Campanha et al., 2015), which match the age of the main dextral movement of the
930 Sarandí del Yí Shear Zone in the RPC (see sections 1-2). Galena in Pb-Zn-Cu-Pb
931 deposits in the Votuverava Group yielded Pb-Pb ages of 1270 and 1303 Ma (Campanha
932 et al., 2015 and references therein), which are very similar to the ages of galena in the
933 PUG (Bossi and Navarro, 2001, Fig. 15).

934 There is a striking similarity between the stratigraphy and evolution of the Apiaí
935 Terrane and that of the NPT (Fig. 17A). Both include ca. 1.75 anorogenic granites (e.g.
936 Illescas Batholith in the NPT: Fig. 1), Calymmian to Ectasian volcanosedimentary
937 successions deposited in a back-arc, extensional setting, glacial rocks of Gaskiers age
938 (Las Ventanas Formation in the NPT: Gaucher et al., 2008b) and Ediacaran granitic
939 magmatism. Santos et al. (2017, 2019) proposed a larger extension of the RPC to

include the Luís Alves, Curitiba and Apiaí terranes. It is conceivable that the Ibaré Shear Zone (sinistral: Cerva-Alves et al., 2020) could have displaced the NPT some 150 km to the NW (Fig. 17B), in which case the Apiaí Terrane would represent its continuation in the Ribeira Belt, supporting the hypothesis of Santos et al. (2019). This displacement must have taken place before the late Ediacaran-Cambrian docking of Arachania, probably during the ca. 720 Ma São Gabriel Orogeny (Philipp et al., 2018). More work is needed to test the Nico Pérez-Apiaí correlation, which would have profound implications for our understanding of SW-Gondwana amalgamation.

8.4.2. A connection with the Amazon Craton?

In Brazil and Bolivia, the Santa Helena Orogeny (Santos et al., 2008) or Alto Guaporé/ Alto Central Brazil Orogeny (Teixeira et al., 2020) matches the age of the Calymmian volcanosedimentary units of the NPT. This orogeny is characterized by an accretionary phase between 1.47 and 1.43 Ga and a later collisional stage at 1.35 Ga associated to the amalgamation of the Paraguá Block to Amazonia (Rizzotto et al., 2013; Teixeira et al., 2020). The orogen is currently located some 2000 km to the NNW of our study area, but a continuation to the south, reaching the margin of the RPC, was already postulated by Santos et al. (2008). Likewise, based on detrital zircon age patterns of Neoproterozoic sandstones, Gaucher et al. (2008a, 2011) suggested a linkage between the Mesoproterozoic rocks in western Amazonia (Sunsás Belt) and the western RPC as part of a proto-Andean margin.

A volcanosedimentary succession very similar to the MVG crops out in Vallemí (Rio Apa Terrane, NE Paraguay), which includes sandstone, shale and basalt, overlain by oolitic and stromatolitic, *Conophyton*-bearing carbonates (Warren et al., 2019). The unit

964 has been grouped with *bona fide* Ediacaran carbonates rich in fossils into the Itapucumí
965 Group (Warren et al., 2019). However, the Vallemí succession lacks Ediacaran index
966 fossils (e.g. *Cloudina*) and exhibits a stratigraphic sequence and $\delta^{13}C$ values of
967 carbonates (0 to 2.5 ‰ VPDB), which are indistinguishable from those of the MVG
968 (Gaucher et al., 2011; Poiré, 2014). Furthermore, the unit is more intensely deformed
969 than the flat-lying Ediacaran carbonates and shows an opposite, E-directed vergence
970 (Campanha et al., 2010), which is compatible with that observed for the Calymmian
971 units in the NPT in Uruguay (Figs. 1-2). This led Poiré (2014) to suggest a correlation,
972 which would imply a northward continuation of the NPT and a connection of the latter
973 with the Rio Apa Terrane already in the Calymmian. Absolute ages for the Vallemí
974 successions are needed to confirm or discard this correlation, which may have important
975 implications for our understanding of the southward continuation of the long-lived
976 Mesoproterozoic orogens in SW Amazonia, and their relationship -or lack thereof- with
977 Calymmian units in the Apiaí and Nico Pérez terranes.

978

979 *8.5. Correlations with the Namaqua-Natal Belt*

980 The NPT is juxtaposed along the Sierra Ballena Shear Zone to the Cuchilla Dionisio
981 Terrane (CDT), which is the core of the Arachania paleocontinent (Figs. 1, 17), an
982 allochthonous block of Kalahari Craton affinity amalgamated to the RPC in the latest
983 Ediacaran and Cambrian (Gaucher et al., 2009, Frimmel et al., 2011). The oldest known
984 rocks in the CDT (Cerro Olivo Complex, Figs. 17-18) are Tonian to Cryogenian,
985 granulite-facies orthogneisses which protholiths intruded a volcanosedimentary
986 succession of probable late Mesoproterozoic age (e.g. Hartmann et al., 2002; Basei et
987 al., 2011; Lenz et al., 2011; Konopásek et al., 2018; Will et al., 2019, 2020). The 780-

760 granitic magmatism of the CDT matches in age the anorogenic Richtersveld Igneous Complex, which intruded the Kalahari Craton (Richtersveld Terrane; see Will et al., 2020 and references therein), marking the separation of Arachania from the Kalahari Craton.

Gaucher et al. (2009, 2011) proposed that, prior to Tonian rifting, the Kalahari Craton, the RPC (including the NPT) and the basement of the CDT (core of Arachania) formed a coherent crustal unit and were an integral part of Rodinia (e.g. Fig. 19D). The connection between the basement of Arachania and the NPT in the late Mesoproterozoic has been recently confirmed by U-Pb detrital zircon ages of metasandstones of the Cerro Olivo Complex, which were likely deposited between 0.75 and 1.0 Ga (Konopásek et al., 2018). These metasandstones have age peaks (in order of decreasing importance) of 2.05-2.0 Ga (Transamazonian), 1.75 Ga, 1.45-1.50 Ga, 1.1 Ga and subordinate Archean peaks at 2.7 and 3.0 Ga (Konopásek et al., 2018). Except for the 1.1 Ga zircons, all other peaks can be explained by provenance from the NPT, and possibly also from the western RPC, where Transamazonian rocks are best exposed. Provenance from the Congo or Kalahari cratons is less likely because sandstones of comparable age show different age peaks (Foster et al., 2015). If a provenance from the NPT is assumed, the occurrence of a 1.45-1.50 Ga peak shows that the Calymmian volcanosedimentary succession was already exhumed and available as a source at ca. 1.0 Ga.

The question arises as to how the amalgamation between the Kalahari Craton and RPC might have proceeded. The elucidation of this process (Fig. 19) is hampered by Neoproterozoic tectonics overprinting older events, and by the recognition that Arachania is sandwiched between both cratons (Fig. 18). However, striking similarities can be observed between the Mesoproterozoic evolution of the eastern RPC and the

Namaqua-Natal Belt of the Kalahari Craton, including the dominance at both sides of dextral shear zones, which in a Gondwana pre-drift configuration are parallel to each other (Fig. 18). Furthermore, the main Namaqua (Kibaran) phase of compressional tectonics took place at 1.25-1.20 Ga (Macey et al., 2018), which matches the available ages in the NPT.

Another interesting feature is the occurrence, at the Kalahari side, of high-grade, ca. 1.2-1.3 Ga metamorphic complexes (e.g. Gordonia Subprovince: Miller, 2008; Kakamas Terrane: Bial et al., 2015; Fig. 18) and extensive, late Ectasian Namaqua intrusions, for example the 1.23-1.18 Ga Little Namaqua Suite in the Bushmanland Terrane (Macey et al., 2018) and the 1.26-1.20 Ga arc magmatism in the Konkiep Terrane (Cornell et al., 2015; Fig. 18). These terranes could conceivably represent the arc, behind which the Tapes Complex was deposited (Fig. 19B), given the lack of comparable rocks in the RPC.

Alternatively, the basement of the CDT (Cerro Olivo Complex), which was metamorphosed to granulite-facies conditions during the Brasiliano-Pan African orogeny (e.g. Gross et al., 2009; Masquelin et al., 2012; Will et al., 2020), may represent the arc (Fig. 19B). The Cerro Olivo Complex contains rocks with Mesoproterozoic protoliths (e.g., Basei et al., 2011) and hosts a large amount of Mesoproterozoic zircon inheritance (Lenz et al., 2011), with the main age population clustering around 1.30-1.22 Ga (Lenz et al., 2011). Will et al. (2019) proposed, based on lithogeochemistry, Nd isotopes and zircon Hf and $\delta^{18}O$ data, that the Cerro Olivo orthogneisses were formed by re-melting of Namaqua-age arc rocks, which have similar εHf and T_{DM} values as the Namaqua terranes exposed in southwestern Africa (Konopásek et al., 2018; Will et al., 2019). Thus, both the age and the geochemical signature of the Cerro Olivo protoliths are consistent with the existence of a

Mesoproterozoic arc in the proto-CDT, which may or may not have acted as one of the source of detritus for the Tapes Complex at 1.35-1.25 Ga.

On the one hand, the proposed neighbouring positions of the NPT and the proto-CDT in Rodinia at ca. 1.0 Ga (Fig. 19D) support this proposition. On the other hand, the lack of Archean crustal residence ages in the CDT (Will et al., 2019, 2020), which are typical of the NPT in general and the Tapes Complex in particular (Fig. 9), militates against this possibility. The only Namaqua terrane with significant Archean inheritance is the Richtersveld Terrane, as evidenced by detrital zircon ages between 3.2 and 2.55 Ga and a significant peak at ca. 2.7 Ga (Macey et al., 2017). Corresponding Nd model ages of Paleoproterozoic rocks in the Richtersveld Terrane range between 2.8 and 2.15 Ga (Reid, 1997; Macey et al., 2017) and partially overlap with model ages obtained for the NPT and the Piedra Alta and Tandilia terranes (Fig. 9). At present, the complexity of the amalgamation of the Namaqua-Natal Orogen and the remaining uncertainties associated with its formation, as well as its extensive Neoproterozoic overprint, prevent a more precise reconstruction.

9. Conclusions

Parts of a Mesoproterozoic belt are exposed in the southeastern Nico Pérez Terrane (Río de la Plata Craton), which includes the Calymmian Parque UTE and Mina Verdún Groups (1.48-1.43 Ga) and the Ectasian Tapes Complex. The age of the Tapes Complex is constrained between 1360±12 Ma and 1253±32 Ma by the U-Pb age of the youngest detrital zircon and the K-Ar muscovite age of cross-cutting thrusts. An Sm-Nd isochron age of 1403 Ma ± 150 Ma for associated mafic and ultramafic rocks is broadly consistent with this age assignment. The U-Pb SIMS age of of 601±5 Ma for the

intruding Tapes Chico Syenite shows that this intrusion represents an unrelated, much younger and probably anorogenic event.

The Tapes Complex consists of a marine volcanosedimentary succession dominated by siliciclastic and ultramafic protoliths, with subordinate intercalations of carbonate, chert and basalt. The unit experienced greenschist facies metamorphism and a main deformation event at 1.2 Ga and a later reworking during the late Brasiliano-Pan African tectonism, which is especially evident in the eastern part of the Tapes Complex.

The best-preserved mafic and ultramafic samples have positive εNd (t) values and Nd model ages of 1.55 to 1.68 Ga, which are close to the assumed crystallization age. Other samples provide geochemical evidence for metamorphic and/or metasomatic alteration, which is corroborated by high $^{87}Sr/^{86}Sr$ ratios of the samples. The Nd model ages of the metasedimentary rocks range from late Paleoproterozoic to Mesoarchean, which is interpreted to indicate two different source areas, the Archean La China Complex and Mesoproterozoic mafic and ultramafic rocks, that include fragments of oceanic crustal material. Pb isotopes data point to derivation from the unradiogenic lower crust. This is also supported by high MgO concentrations, high Cr/V and low Y/Ni and Th/Sc ratios as well as the lack of an Eu anomaly in the REE patterns.

An evolution is postulated starting with an extensional basin between 1.48 and ca. 1.40 Ga, corresponding to a rift or a retroarc basin, in which the Calymmian units were deposited. The basin infill must have been exhumed together with slivers of oceanic crust by the time of deposition of the Tapes Complex, in order to account for the drastic changes in provenance, as shown for example by U-Pb detrital zircon ages. The Tapes Complex was probably deposited in a retroarc foreland basin during the ca. 1.25 Ga

Kibaran event, which matches the age of deformation and metamorphism in the Nico Pérez Terrane.

It is concluded that the Kibaran arc associated with the Tapes basin can be found in the Namaqua sector of the Namaqua-Natal Belt. The Konkiep and Bushmanland terranes are characterized by high-grade metamorphism and arc magmatism at ca. 1.3-1.2 Ga, which match the ages in the Nico Pérez Terrane. The basement of the Cuchilla Dionisio Terrane in Uruguay also comprises a Kibaran arc strongly reworked during the Brasiliano-Pan African orogeny and could also be a potential source area for the Tapes Complex. However, only the Richtersveld Terrane in the Namaqua sector contains Archean rocks, which makes it a potential source of the Tapes Complex, but evidence of a Kibaran arc, such as high-grade metamorphic rocks, is still lacking in the Richtersveld Terrane. This notwithstanding the Tapes Complex is a key area for our understanding of the assembly of the Río de la Plata and Kalahari cratons and their amalgamation to the Rodinia supercontinent. The Mesoproterozoic Apiaí Terrane in the Ribeira Belt and the Nico Pérez Terrane show a similar stratigraphy and tectonic evolution between the late Paleo- and Neoproterozoic. The Apiaí Terrane may be a fragment of the Nico Pérez Terrane displaced to the NW by the Ibaré Shear Zone. Further to the north, carbonate units of the Rio Apa Terrane in NE Paraguay may correlate with Calymmian units in the Nico Pérez Terrane, but more work is needed to prove or disprove this idea.

Acknowledgements

This work is dedicated to the memories of Gustavo Paglia, who encouraged and actively supported early geological research in the area, and Valdroir Silveira, who provided access to important outcrops near Colón and collaborated during field work. Enrique

Ramírez is thanked for valuable assistance during field work and sampling. Our recognition goes to the late Prof. Jorge Bossi for his invaluable insight and fruitful discussions. We are indebted to Martin Whitehouse for valuable help with U-Pb SIMS dating at NordSIM (Stockholm). Valuable comments of anonymous reviewers helped improve an earlier version of the manuscript. Research grants from ANII and PEDECIBA Geosciences (Uruguay) to LS are gratefully acknowledged. A research project ("*Terreno Nico Pérez: geología y recursos minerales*") funded by CSIC (Uruguay) helped finance field work and other expenses. This work was also supported by the Deutsche Forschungsgemeinschaft (grant Wi 1225/8) and the Chinese State Key Research and Development Program (grant 2016YFE0203000).

References

Alibo, D.S., Nozaki, Y., 1999. Rare earth elements in seawater: particle association, shale normalization, and Ce oxidation. Geochimica et Cosmochimica Acta 63, 363–372.

Almeida, F.F.M.de, Amaral, G., Cordani, U.G. and Kawashita, K., 1973. The Precambrian evolution of South American cratonic margin south of the Amazon River. In: Nairn, A.E.M. and Stehli, F.G. (Eds.), The ocean basins and margins. Vol. 1: The South Atlantic. Plenum, New York, pp. 411-446.

Bahlburg, H., Dobrzinski, N., 2011. A review of the Chemical Index of Alteration (CIA) and its application to the study of Neoproterozoic glacial deposits and climate transitions. Geological Society, London, Memoirs, 36(1), 81-92.

Ballivián Justiniano, C.A.B., Basei, M.A., Sato, A.M., González, P.D., Benítez, M.E., Lanfranchini, M.E. (2020). The Neoproterozoic basement of the Sauce Chico Inlier (Ventania System): Geochemistry and U–Pb geochronology of igneous rocks with African lineage in central-eastern Argentina. Journal of South American Earth Sciences 98, 102391.

Basei, M.A.S., Peel, E., Sánchez Bettucci, L., Preciozzi, F., Nutman, A.P., 2011. The basement of the Punta del Este Terrane (Uruguay): an African Mesoproterozoic fragment at the eastern border of the South American Río de la Plata Craton. International Journal of Earth Sciences 100, 289-304.

Bettencourt, J.S., Leite Jr., W., Payolla, B., Ruiz, A.S., Matos, R.S., Tosdal, R.M., 2010. The Rondonian-San Ignacio Province in the SW Amazonian Craton: an overview. Journal of South American Earth Sciences 29, 28–46.

Bhatia, M. R, Crook, K.A.W, 1986. Trace element characteristics of graywackes and tectonic setting discrimination of sedimentary basins. Contributions to Mineralogy and Petrology 92, 181-193.

Bial, J., Büttner, S. H., Schenk, V., Appel, P., 2015. The long-term high-temperature history of the central Namaqua Metamorphic Complex: Evidence for a Mesoproterozoic continental back-arc in southern Africa. Precambrian Research 268, 243-278.

Blanco, G., Rajesh, H.M., Gaucher, C., Germs, G.J.B., Chemale Jr., F. 2009. Provenance of the Arroyo del Soldado Group (Ediacaran to Cambrian, Uruguay): Implications for the paleogeographic evolution of southwestern Gondwana. Precambrian Research, 171, 57-73.

Bossi, J. 1966., Geología del Uruguay. Departamento Publicaciones Universidad de la República, Montevideo.

Bossi, J. 1978. Recursos minerales del Uruguay. Ediciones Daniel Aljanati, Montevideo, pp. 1-348.

Bossi, J., Campal, N., 1992. Magmatismo y tectónica transcurrente durante el Paleozoico Inferior en Uruguay. In: J. G. Gutierrez- Marco, J. Saavedra, I. Rabano (Editors): Paleozoico Inferior de Iberoamérica. Universidad de Extremadura, Mérida, pp 343- 356.

Bossi, J., Ferrando, L., Montaña, J., Campal, N., Morales, H., Gancio, F., Schipilov, A., Piñeyro, D., Sprechmann, P., 1998. Carta geológica del Uruguay. Escala 1:500.000. Geoeditores, Montevideo.

Bossi, J., Schipilov, A., 1998. Rocas ígneas básicas del Uruguay. Volumen I. Facultad de Agronomía, Montevideo,

Bossi, J., Navarro, R., 2001. Grupo Carapé: su reivindicación. Revista de la Sociedad Uruguaya de Geología 8, 2-12.

Bossi, J., Schipilov, A., 2007. Rocas ígneas básicas del Uruguay. Facultad de Agronomía, Montevideo, 364 pp.

Bossi, J., Cingolani, C.A. 2009. Extension and general evolution of the Río de la Plata Craton. In: Gaucher, C., Sial, A.N., Halverson, G.P., Frimmel, H.E. (Eds.), Neoproterozoic-Cambrian tectonics, global change and evolution: a focus on southwestern Gondwana. Developments in Precambrian Geology 16: 73–85.

Bucher, K., Frey, M. 1994. Petrogenesis of Metamorphic Rocks. Complete revision of Winkler´s Textbook. 6th Edition. Springer-Verlag, Berlin, pp. 1-318.

Campanha, G.A.C., Basei, M.S., Tassinari, C.C.G., Nutman, A.P., Faleiros, F.M., 2008. Constraining the age of the Iporanga Formation with SHRIMP U-Pb zircon: implications for possible Ediacaran glaciation in the Ribeira Belt, SE Brazil. Gondwana Research 13, 117-125.

Campanha, G.A.C., Warren, L., Boggiani, P.C., Grohmann, C.H., Cáceres, A.A., 2010. Structural analysis of the Itapucumí Group in the Vallemi region, northern Paraguay: Evidence of a new Brasiliano/Pan-African mobile belt. Journal of South American Earth Sciences 30, 1–11.

Campanha, G.A.C., Faleiros, F.M., Basei, M.A.S., Tassinari, C.C.G., Nutman, A.P., Vasconcelos, P.M., 2015. Geochemistry and age of mafic rocks from the Votuverava Group, southern Ribeira Belt, Brazil: evidence for 1490 Ma oceanic back-arc magmatism. Precambrian Research 266, 530-550.

Campanha, G.A.C., Faleiros, F.M., Cawood, P.A., Cabrita, D.I.G., Ribeiro, B.V., Basei, M.A.S., 2019. The Tonian Embu Complex in the Ribeira Belt (Brazil): revision, depositional age and setting in Rodinia and West Gondwana. Precambrian Research 320, 31-45.

Cernuschi, F., Dilles, J.H., Kent, A.J.R., Schroer, G., Raab, A.K., Conti, B., Muzio, R. 2015. Geology, geochemistry and geochronology of the Cretaceous Lascano East intrusive complex and magmatic evolution of the Laguna Merín basin, Uruguay. Gondwana Research 28, 837–857.

Cerva-Alves, T., Hartmann, L.A., Remus, M.V.D., Lana, C. 2020. Integrated ophiolite and arc evolution, southern Brasiliano Orogen. Precambrian Research 341, 105648.

Chiglino, L. 2008. Quimioestratigrafía de sequências meso e neoproterozóicas do Terreno Nico Pérez: idade, ambiente de sedimentaçao e correlaçoes. Unpublished MSc Thesis, Universidade Federal de Pernambuco, Recife, Brazil, pp. 1-81.

Chiglino, L., Gaucher, C., Sial, A.N., Bossi, J., Ferreira, V.P., Pimentel, M.M., 2010. Chemostratigraphy of Mesoproterozoic and Neoproterozoic carbonates of the Nico Pérez Terrane, Río de la Plata Craton, Uruguay. Precambrian Research, 182, 313-336.

Cingolani, C., 2011. The Tandilia System of Argentina as a southern extension of the Río de la Plata craton: an overview. International Journal of Earth Sciences, 100, 221-242.

Cornell, D.H., Thomas, R.J., Moen, H.F.G., Reid, D.L., Moore, J.M., Gibson, R.L., 2006. The Namaqua-Natal Province. In: Johnson, C.A., Anhaeusser, C.R., Thomas, R.J. (Eds.), The Geology of South Africa. Geological Society of South Africa, Johannesburg, pp. 325-379.

Cornell, D. H., van Schijndel, V., Simonsen, S. L., Frei, D., 2015. Geochronology of Mesoproterozoic hybrid intrusions in the Konkiep Terrane, Namibia, from passive to active continental margin in the Namaqua-Natal Wilson Cycle. Precambrian Research 265, 166-188.

Dalla Salda, L.H., Bossi, J., Cingolani, C.A. 1988. The Río de la Plata cratonic region of southwestern Gondwana. Episodes 11, 263–269.

Dalziel, I. W. D., Mosher, S., Gahagan, L. M. 2000. Laurentia‐Kalahari Collision and the Assembly of Rodinia. The Journal of Geology, 108(5), 499–513.

Delacour, A., Früh-Green, G. L., Frank, M., Gutjahr, M., Kelley, D. S., 2008. Sr-and Nd-isotope geochemistry of the Atlantis Massif (30 N, MAR): implications for fluid fluxes and lithospheric heterogeneity. Chemical Geology, 254, 19-35.

DePaolo, D. J. 1988. Age dependence of the composition of continental crust: evidence from Nd isotopic variations in granitic rocks. Earth and Planetary Science Letters 90, 263-271.

DePaolo, D.J., Wasserburg, G.J., 1976. Inferences about magma sources and mantle structure from variations of $^{143}Nd/^{144}Nd$. Geophysical Research Letters 3, 743–746.

Deschamps, F., Godard, M., Guillot, S., Hattori, K., 2013. Geochemistry of subduction zone serpentinites: A review. Lithos, 178, 96-127.

Diaz, R., Albanell, H., Bossi, J. 1990. Carta Geológica del Uruguay, Hoja F-24 Cerro Partido, Escala 1:100.000. Memoria explicativa.- Montevideo, Facultad de Agronomía.

Dickinson, W.R., Gehrels, G.E. 2009. Use of U–Pb ages of detrital zircons to infer maximum depositional ages of strata: a test against a Colorado Plateau Mesozoic database. Earth and Planetary Science Letters 288, 115-125.

DINAMIGE (Dirección Nacional de Minería y Geología), 2015. Relevamiento Aerogeofísico de Magnetometría y de Espectrometría de Rayos Gamma. Ministerio de Industria, Energía y Minería, Montevideo.

Einsele, G., 2000. Sedimentary basins. Evolution, facies and sediment budget. Springer, Berlin, pp. 1-792.

Faleiros, F.M., Ferrari, V.C., Costa, V.S., Campanha, G.A.C., 2011. Geoquímica e petrogênese de metabasitos do Grupo Votuverava (Terreno Apiaí, Cinturão Ribeira Meridional): Evidências de uma bacia retroarco calimiana. Geologia USP-Série Científica 11, 135–155.

Foster, D. A., Goscombe, B.D., Newstead, B., Mapani, B., Mueller, P.A., Gregory, L.C., Muvangua, E. 2015. U–Pb age and Lu–Hf isotopic data of detrital zircons from the Neoproterozoic Damara Sequence: Implications for Congo and Kalahari before Gondwana. Gondwana Research 28, 179-190.

Frey, F.A., 1984. Rare earth element abundances in upper mantle rocks. In: Henderson, P. (Ed.), Developments in Geochemistry, vol. 2, pp. 153-203, Elsevier.

Frey, F. A., Haskin, L. A., Haskin, M.A., 1971. Rare-Earth abundances in some ultramafic rocks. Journal of Geophysical Research, 76(8), 2057-2070.

Frimmel, H.E., Basei, M.A.S., Gaucher, C., 2011. Neoproterozoic geodynamic evolution of SW-Gondwana: a southern African perspective. International Journal of Earth Sciences 100, 323-354.

Frimmel, H.E., Basei, M.A.S., Correa, V.X., Mbangula, N., 2013. A new lithostratigraphic subdivision and geodynamic model for the Pan-African western Saldania Belt, South Africa. Precambrian Research 231, 218– 235.

Fuck, R.A., Brito Neves, B.B., Schobbenhaus, C., 2008. Rodinia descendants in south America. Precambrian Research 160, 108-126.

Gaucher, C., Chiglino, L., Pecoits, E., 2004. Southernmost exposures of the Arroyo del Soldado Group (Vendian to Cambrian, Uruguay): palaeogeographic implications for the amalgamation of W-Gondwana. Gondwana Research, 7, 701-714.

Gaucher, C., Frimmel, H.E., Germs, G.J.B. 2005. Organic-walled microfossils and biostratigraphy of the upper Port Nolloth Group (Namibia): implications for the latest Neoproterozoic glaciations. Geological Magazine 142, 539-559.

Gaucher, C., Finney, S.C., Poiré, D.G., Valencia, V.A., Grove, M., Blanco, G., Pamoukaghlián, K., Gómez Peral, L., 2008a. Detrital zircon ages of Neoproterozoic sedimentary successions in Uruguay and Argentina: insights into the geological evolution of the Río de la Plata Craton. Precambrian Research, 167, 150-170.

Gaucher, C., Blanco, G., Chiglino, L. Poiré, D.G., Germs, G.J.B., 2008b. Acritarchs of Las Ventanas Formation (Ediacaran, Uruguay): implications for the timing of coeval rifting and glacial events in western Gondwana. Gondwana Research 13, 488-501.

Gaucher, C., Frimmel, H.E., Germs, G.J.B. 2009. Tectonic events and palaeogeographic evolution of southwestern Gondwana in the Neoproterozoic and Cambrian. In: Gaucher, C., Sial, A.N., Halverson, G.P., Frimmel, H.E. (Eds): Neoproterozoic-Cambrian Tectonics, Global Change and Evolution: a focus on southwestern Gondwana. Developments in Precambrian Geology 16, Elsevier, pp. 295-316.

Gaucher, C., Chemale Jr., F., Bossi, J., Castiglioni, E.A. 2010. Grupo Cebollatí, Terreno Nico Pérez: definición y edad. In: VI Congreso Uruguayo de Geología, Minas, pp. 1-8.

Gaucher, C., Frei, R., Chemale Jr., F., Frei, D., Bossi, J., Martínez, G., Chiglino, L., Cernuschi, F., 2011. Mesoproterozoic evolution of the Río de la Plata Craton in Uruguay: at the heart of Rodinia? International Journal of Earth Sciences, 100, 273-288.

Gaucher, C., Bossi, J., Martínez, G., Chiglino, L., Frei, R., Sial, A.N. 2014a. Grupo Parque UTE. In: Bossi, J., Gaucher, C. (Eds.) Geología del Uruguay. Tomo 1: Predevónico. Polo, Montevideo, pp. 215-232.

Gaucher, C., Bossi, J., Samaniego, L., Frei, R. 2014b. Complejo Tapes. In: Bossi, J., Gaucher, C. (Eds.) Geología del Uruguay. Tomo 1: Predevónico. Polo, Montevideo, pp. 253-264.

Gaucher, C., Sial, A.N., Frei, R., Ferreira, V.P., Frei, D., Bossi, J., Cabrera, J., 2014c. Magmatismo Anorogénico Ediacárico. In: Bossi, J., Gaucher, C. (Eds.) Geología del Uruguay. Tomo 1: Predevónico. Polo, Montevideo, pp. 283-298.

Goldstein, S.L., O'Nions, R.K., Hamilton, P.J., 1984. A Sm–Nd study of atmospheric dusts and particulates from major river systems. Earth and Planetary Science Letters 70, 221–236.

Gómez Rifas, C., 1995. A zona de cizalhamento sinistral de “Sierra Ballena” no Uruguai. PhD Thesis, Instituto de Geociencias, Universidade de Sao Paulo, pp. 1-244.

Gross, A.O.M.S., Droop, G.T.R., Porcher, C.C., Fernandes, L.A.D., 2009. Petrology and thermobarometry of mafic granulites and migmatites from the Chafalote Metamorphic Suite: new insights into the Neoproterozoic P-T evolution of the Uruguayan-Sul Rio Grandes shield. Precambran Research 170, 157-174.

Hall, W.S., Hitzman, M.W., Kuiper, Y.D., Kylander-Clark, A.R., Holm-Denoma, C.S., Moscati, R. J., Plink-Björklund, P., Enders, M.S., 2018. Igneous and detrital zircon U-Pb and Lu-Hf geochronology of the late Meso-to Neoproterozoic northwest Botswana rift: Maximum depositional age and provenance of the Ghanzi Group, Kalahari Copperbelt, Botswana and Namibia. Precambrian Research 318, 133-155.

Hartmann, L.A., Campal, N., Santos, J.O., Mac Naughton, N. J., Schipilov, A. 2001. Archean crust in the Río de la Plata Craton, Uruguay: SHRIMP U-Pb reconnaissance geochronology. Journal of South American Earth Sciences, 14, 557-570.

Hartmann, L.A., Santos, J.O.S., Cingolani, C.A., McNaughton, N.J. 2002. Two Paleoproterozoic Orogenies in the Evolution of the Tandilia Belt, Buenos Aires, as evidenced by zircon U-Pb SHRIMP geochronology. International Geology Review, 44: 528-543.

Horwitz, E.P., Chiarizia, R., Dietz, M.L., 1992. A novel Strontium-selective extraction chromatographic resin. Solvent Extraction and Ion Exchange 10, 313-336.

Hu, Z., Gao, S., 2008. Upper crustal abundances of trace elements: a revision and update. Chemical Geology, 253, 205-221.

Humphries, D.W., 1994. Methoden der Dünnschliffherstellung. Enke, Stuttgart, pp. 1-85.

Jacobsen, S.B., Wasserburg, G.J., 1980. Sm–Nd isotopic evolution of chondrites. Earth Planetary Science Letters, 50, 139–155.

Jacobsen, S.B., Kaufman, A.J., 1999. The Sr, C and O isotopic evolution of Neoproterozoic seawater. Chemical Geology 161, 37–57.

Karlsen, T.A., Rian, E., Olesen, O., 2000. Overview of talc resources in the Altermark talc province, northern Norway, and possible uses of the talc ore. NGU Bulletin, 436, 93-102.

Kato, Y., Yamaguchi, K. E., Ohmoto, H. 2006. Rare earth elements in Precambrian banded iron formations: Secular changes of Ce and Eu anomalies and evolution of atmospheric oxygen. Geological Society of America Memoir 198, 269-289.

Kemp, A.I.S., Hawkesworth, C.J., Foster, G.L., Paterson, B.A., Woodhead, J.D., Hergt, J.M., Gray, C.M., Whitehouse, M.J., 2007. Magmatic and crustal differentiation history of granitic rocks from Hf-O isotopes in zircon. Science 315, 980-983.

Keto, L.S., Jacobsen, S.B., 1987. Nd and Sr isotopic variations of Early Paleozoic oceans. Earth and Planetary Science Letters 84, 27–41.

Konopásek, J., Janoušek, V., Oyhantçabal, P., Sláma, J., Ulrich, S., 2018. Did the circum-Rodinia subduction trigger the Neoproterozoic rifting along the Congo–Kalahari Craton margin? International Journal of Earth Sciences 107, 1859-1894.

Kuznetsov, A. B., Semikhatov, M. A., Gorokhov, I. M., 2014. The Sr isotope chemostratigraphy as a tool for solving stratigraphic problems of the Upper Proterozoic (Riphean and Vendian). Stratigraphy and Geological Correlation 22, 553-575.

Le Maitre, R.W., Bateman, P., Dubek, A., Keller, J., Lameyre, J., Le Bas, M.J., Sabine, P.A., Schimid, R., Sorensen, H., 1989. A Classification of Igneous Rocks and Glossary of Terms: Recommendations of the Inter-national Union of Geological Sciences Subcommission on the Systematics of Igneous Rocks. Blackwell, Oxford.

Lenz, C., Fernandes, L.A.D., McNaughton, N.J., Porcher, C.C., Masquelin, H., 2011. U–Pb SHRIMP ages for the Cerro Bori Orthogneisses, Dom Feliciano Belt in Uruguay: Evidences of a ~800Ma magmatic and ~650Ma metamorphic event. Precambrian Research 185, 149–163.

Li, X.H., Liu, Y., Li, Q.L., Guo, C.H., Chamberlain, K.R., 2009. Precise determination of Phanerozoic zircon Pb/Pb age by multi-collector SIMS without external standardization. Geochememistry Geophysics Geosystems 10, Q04010.

Li, Q.L., Li, X.H., Liu, Y., Tang, G.Q., Yang, J.H., Zhu, W.G., 2010a. Precise U-Pb and Pb- Pb dating of Phanerozoic baddeleyite by SIMS with oxygen flooding technique. Journal of Analytical Atomic Spectrometry 25, 1107–1113.

Li, X.H., Long, W.G., Li, Q.L., Liu, Y., Zheng, Y.F., Yang, Y.H., Chamberlain, K.R., Wan, D.F., Guo, C.H., Wang, X.C., Tao, H., 2010b. Penglai zircon megacryst: a potential new working reference for microbeam analysis of Hf-O isotopes and U-Pb age. Geostandard Geoanalytical Research 34, 117–134.

Li, Q.L., Li, X.H., Lan, Z., Guo, C., Yang, Y., Liu, Y., Tang, G., 2013. Monazite and xenotime U-Th–Pb geochronology by ion microprobe: dating highly fractionated granites at Xihuashan tungsten mine, SE China. Contributions to Mineralogy and Petrology 166, 65–80.

Ludwig, K.R., 1988. ISOPLOT - A plotting and regression program for radiogenic isotope data for IBM-PC compatible computers. U.S. Geological Survey Open-File Report 88-557, 32 pp.

Ludwig, K.R., 2012. User manual for Isoplot 3.75. A geochronological toolkit for Microsoft Excel. Berkeley Geochron. Center Spec. Publ. 5, 1–75.

Macey, P.H., Thomas, R.J., Minnaar, H.M., Gresse, P.G., Lambert, C.W., Groenewald, C.A., Miller, J.A., Indongo, J.I., Angombe, M., Shifotoka, G., Frei, D., Diener, J.F.A., Kisters, A.F.M., Dhansay, T., Smith, H., Doggart, S., le Roux, P., Hartnady, M.I., Tinguely, C., 2017. Origin and evolution of the ~1.9 Ga Richtersveld Magmatic Arc, SW Africa. Precambrian Research 292, 417–451.

Macey, P.H., Bailie, R., Miller, J.A., Thomas, R.J., De Beer, C., Frei, le Roux, P., 2018. Implications of the distribution, age and origins of the granites of the Mesoproterozoic Spektakel Suite for the timing of the Namaqua Orogeny in the Bushmanland Subprovince of the Namaqua-Natal Metamorphic Province, South Africa. Precambrian Research 312, 68–98.

Masquelin, H., D'Avila Fernandes, L. A., Lenz, C., Porcher, C.C., McNaughton, N.J. 2012. The Cerro Olivo complex: a pre-collisional Neoproterozoic magmatic arc in Eastern Uruguay. International Geology Review 54, 1161-1183.

Mallmann, G., Chemale, F., Avila, J.N., Kawashita, K., Armstrong, R.A. 2007. Isotope geochemistry and geochronology of the Nico Pérez Terrane, Río de la Plata Craton, Uruguay. Gondwana Research 12, 489-508.

McCulloch, M.T., Black, L.P., 1984. Sm-Nd isotopic systematics of Enderby Land granulites and evidence for the redistribution of Sm and Nd during metamorphism. Earth and Planetary Science Letters 71, 46-58.

McLennan, S.M., 1989. Rare earth elements in sedimentary rocks: influence of provenance and sedimentary processes. Mineralogical Society of America Reviews in Mineralogy, 21: 169-200.

McLennan, S. M., 1993. Weathering and global denudation. The Journal of Geology, 101(2), 295-303.

McLennan, S.M., Hemming, S., McDaniel, D.K., Hanson, G.N., 1993. Geochemical approaches to sedimentation, provenance and tectonics. In: Johnsson, M.J., Basu, A., (Eds.), Processes Controlling the Composition of Clastic Sediments. Geological Society of America, Special Paper, 284, 21-40.

McLennan, S.M., Taylor, S.R., Hemming, S.R., 2006. Composition, differentiation, and evolution of continental crust: constrains from sedimentary rocks and heat flow. In: Brown, M., Rushmer, T. (Eds.), Evolution and differentiation of the continental crust, pp. 92-134.

Meert, J.G., Lieberman, B.S. 2008. The Neoproterozoic assembly of Gondwana and its relationship to the Ediacaran–Cambrian radiation. Gondwana Research, 14(1-2), 5-21.

Midot, D., 1984. Etude Geologique et diagnostic metallogenique pour l'exploration du Secteur de Minas (Uruguay). PhD Thesis, Université Pierre et Marie Curie, París, pp. 1-175.

Miller, R.McG., 2008. Namaqua Metamorphic Complex. In: Miller, R.McG. (Ed.) The Geology of Namibia. Volume I: Archean to Mesoproterozoic. Geological Survey of Namibia, Windhoek, pp. 1-55.

Moore, D.M., Reynolds Jr., R.C., 1989. X-Ray Diffraction and the Identification and Analysis of Clay Minerals. Oxford University Press. pp. 1-329.

Nesbitt, H.W., Young, G.M., 1982. Early Proterozoic climates and plate motions inferred from major element chemistry of lutites. Nature, 199: 715-717.

Oriolo, S., Oyhantçabal, P., Wemmer, K., Basei, M. A., Benowitz, J., Pfänder, J., Hannich, F., Siegesmund, S. 2016. Timing of deformation in the Sarandí del Yí Shear Zone, Uruguay: Implications for the amalgamation of western Gondwana during the Neoproterozoic Brasiliano-Pan-African Orogeny. Tectonics 35, 754-771.

Oriolo, S., Oyhantçabal, P., Konopásek, J., Basei, M. A., Frei, R., Sláma, J., Wemmer, K., Siegesmund, S., 2019. Late Paleoproterozoic and Mesoproterozoic magmatism of the Nico Pérez Terrane (Uruguay): Tightening up correlations in southwestern Gondwana. Precambrian Research, 327, 296-313.

Oyhantçabal, P., Spoturno, J., Goso, E., Heimann, A., Bergalli, L., 2001. Asociaciones litológicas en las supracrustales del Grupo Lavalleja y sus intrusiones asociadas en la Hoja Fuente del Puma (Sur de Minas). III Congreso Uruguayo de Geología and XI Congreso Latinoamericano de Geología, Montevideo, Nr. 246 (CD-ROM).

Oyhantçabal, P.B., Sanchez Bettucci, L., Peçoits, E., Aubet, N., Peel, E., Preciozzi, F., Basei, M.A.S., 2005. Nueva propuesta estratigráfica para las supracorticales del Cinturón Dom Feliciano (Proterozoico, Uruguay). XII Congreso Latinoamericano de Geología, Quito.

Oyhantçabal, P., Siegesmund, S., Wemmer, K. 2011. The Río de la Plata Craton: a review of units, boundaries, ages and isotopic signature. International Journal of Earth Sciences 100, 201-220.

Pamoukaghlián, K., Gaucher, C., Frei, R., Poiré, D. G., Chemale, F., Frei, D., Will, T. M., 2017. U-Pb age constraints for the La Tuna Granite and Montevideo Formation (Paleoproterozoic, Uruguay): Unravelling the structure of the Río de la Plata Craton. Journal of South American Earth Sciences 79, 443-458.

Passarelli, C. R., Basei, M. A. S., Wemmer, K., Siga, O., Oyhantçabal, P., 2011. Major shear zones of southern Brazil and Uruguay: escape tectonics in the eastern border of Rio de La Plata and Paranapanema cratons during the Western Gondwana amalgamation. International Journal of Earth Sciences 100, 391-414.

Pearce, J.A. 1996. A User´s guide to basalt discrimination diagram. In: Wyman, D.A. (Ed.), The Trace Element Geochemistry of Volcanic Rocks: Applications for Massive

Sulphide Exploration. Geological Assocation of Canada, Short Course Notes 12, 79-113.

Pearce, J.A. 2008, Geochemical fingerprinting of oceanic basalts with applications to ophiolite classification and the search for Archean oceanic crust. Lithos 100, 14–48.

Pettijohn, F.J.; Potter, P.E. Siever, R., 1987. Sand and sandstone. Second edition. Springer, New York, pp. 1-553.

Philipp, R.P., Pimentel, M.M., Basei, M.A.S. 2018. The tectonic evolution of the São Gabriel terrane, Dom Feliciano belt, southern Brazil: the closure of the Charrua ocean. In: Siegesmund, S., Basei M., Oyhantçabal P., Oriolo S. (Eds) Geology of Southwest Gondwana. Regional Geology Reviews, Springer, Cham, pp. 243-265.

Pohl, W. 1992. Lagerstättenlehre. Eine Einführung in die Wissenschaft von den mineralischen Bodenschätzen. 4. Auflage. E. Schweizerbart'sche, Stuttgart, 504 pp.

Poiré, D.G., González, P.D., Canalicchio, J.M., García Repetto, F., Canessa, N.D., 2005. Estratigrafía del Grupo Mina Verdún, Proterozoico de Minas, Uruguay. Latin American Journal of Sedimentology and Basin Analysis, 12: 125-143.

Poiré, D.G., 2014. Grupo Mina Verdún. In: Bossi, J., Gaucher, C. (Eds.) Geología del Uruguay. Tomo 1: Predevónico. Polo, Montevideo, pp. 233-251.

Powell, C. M., Jones, D.L., Pisarevsky, S., Wingate, M.T.D. 2001. Palaeomagnetic constraints on the position of the Kalahari craton in Rodinia. Precambrian Research 110, 33-46.

Ramos, R.C., Koester, E., Vieira, D.T., Porcher, C.C., Gezatt, J.N., Silveira, R.L., 2018. Insights on the evolution the Arroio Grande Ophiolite (Dom Feliciano Belt, Brazil) from Rb-Sr and SHRIMP U-Pb isotopic geochemistry. Journal of South American Earth Sciences 86, 38–53.

Reid, D.L., 1997. Sm-Nd age and REE geochemistry of Proterozoic arc-related igneous rocks in the Richtersveld Subprovince, Namaqua mobile belt, southern Africa. Journal of African Earth Sciences 24, 621–633.

Remus, M. V., Hartmann, L. A., Formoso, M.L., 1993. Os padrões de Elementos Terras Raras (ETR) e a afinidade geoquímica komatiítica dos xistos magnesianos e rochas associadas do Complexo Cambaizinho, São Gabriel/RS. Revista Brasileira de Geociências, 23(4), 370-387.

Rizzotto, G. J., Santos, J. O. S., Hartmann, L. A., Tohver, E., Pimentel, M. M., McNaughton, N. J., 2013. The Mesoproterozoic Guaporé suture in the SW Amazonian Craton: geotectonic implications based on field geology, zircon geochronology and Nd–Sr isotope geochemistry. Journal of South American Earth Sciences 48, 271-295.

Samaniego, L., 2016. Petrografía y geoquímica del Complejo Tapes (Terreno Nico Pérez) y minerales asbestiformes asociados. Unpublished degree thesis, Facultad de Ciencias, Montevideo.

Samaniego, L., García, G., 2013. Mapa geológico del norte de Mariscala, Departamento de Lavalleja. VII Congreso Uruguayo de Geología, Actas, pp. 273-279, Montevideo.

Sánchez Bettucci, L., Ramos, V.A., 1999. Aspectos geológicos de las rocas metavolcánicas y metasedimentarias del Grupo Lavalleja, sudeste de Uruguay. Revista Brasileira de Geociências 29, 557-570.

Sánchez Bettucci,L., Cosarinsky, M., Ramos, V.A., 2001. Tectonic setting of the Late Proterozoic Lavalleja Group (Dom Feliciano Belt), Uruguay. Gondwana Research 4, 395-407.

Santos, J.O.S., Rizzotto, G.J., Potter, P.E., McNaughton, N.J., Matos, R.S., Hartmann, L.A., Chemale Jr., F., Quadros, M.E.S., 2008. Age and autochthonous evolution of the Sunsás Orogen in West Amazon Craton based on mapping and U–Pb geochronology. Precambrian Research 165, 120-152.

Santos, J. O., Chernicoff, C. J., Zappettini, E. O., McNaughton, N. J., Greau, Y., 2017. U-Pb geochronology of Martín García, Sola, and Dos Hermanas Islands (Argentina and Uruguay): Unveiling Rhyacian, Statherian, Ectasian, and Stenian of a forgotten area of the Río de la Plata Craton. Journal of South American Earth Sciences 80, 207-228.

Santos, J.O.S., Chernicoff, C.J., Zappettini, E.O., McNaughton, N.J., Hartmann, L.A., 2019. Large geographic and temporal extensions of the Rio de la Plata Craton, South America and its metacratonic eastern margin. International Geology Review 61, 56-85.

Shand, S.J., 1943. The eruptive rocks. 2nd ed. John Wiley & Sons, New York.

Shields, G., 2007. The marine carbonate and chert isotope records and their implications for tectonics, life and climate on the early Earth. In: van Kranendonk, M.J., Smithies, R.H., Bennett, V.C. (Eds.) Earth's oldest rocks. Developments in Precambrian Geology 15, Elsevier, 971-983.

Siga Jr, O., Basei, M.A.S., Sato, K., Passarelli, C.R., Nutman, A., McReath, I., dos Prazeres Filho, H.J., 2011. Calymmian (1.50–1.45 Ga) magmatic records in Votuverava and Perau sequences, south-southeastern Brazil: Zircon ages and Nd–Sr isotopic geochemistry. Journal of South American Earth Sciences, 32, 301-308.

Sláma, J., Košler, J., Condon, D.J., 11 others, 2008. Plešovice zircon - a new natural reference material for U-Pb and Hf isotopic microanalysis. Chemical Geology 249, 1–35.

Stacey, J.S., Kramers, J.D., 1975. Approximation of terrestrial lead isotope evolution by a two-stage model. Earth and Planetary Science Letters, 26, 207-221.

Strong, T.R., Driscoll, R.L., 2016, A process for reducing rocks and concentrating heavy minerals. U.S. Geological Survey Open-File Report 2016–1022, Reston, pp. 1-16.

Sun, S. S., McDonough, W. F., 1989. Chemical and isotopic systematics of oceanic basalts: implications for mantle composition and processes. Geological Society, London, Special Publications 42, 313-345.

Tang, G.Q., Li, X.H., Li, Q.L., Liu, Y., Ling, X.X., Yin, Q.Z., 2015. Deciphering the physical mechanism of the topography effect for oxygen isotope measurements using a Cameca IMS-1280 SIMS. Journal of Analytical Atomic Spectrometry 30, 950–956.

Teixeira W., Renne, P., Bossi. J., Campal, N., D'Agrella, F., 1999. $^{40}Ar/^{39}Ar$ and Rb/Sr geochronology of the Uruguayan dike swarm, Río de la Plata Craton and implications for Proterozoic intraplate activity in western Gondwana. Precambrian Research, 93, 153-180.

Teixeira, W., Cordani, U.G., Faleiros, F.M., Sato, K., Maurer, V.C., Ruiz, A.S., Azevedo, E.J.P., 2020. The Rio Apa Terrane reviewed: UPb zircon geochronology and provenance studies provide paleotectonic links with a growing Proterozoic Amazonia. Earth-Science Reviews 202, 103089.

Taylor, S.R., McLennan, S.M., 1985. The Continental Crust: Its Composition and Evolution. Blackwell, Oxford.

Todt, W., Cliff, R.A., Hansen, A., Hofmann, A. W., 1996. Evaluation of a ^{202}Pb-^{205}Pb double spike for high-precision lead isotope analysis. In: Hart, S.R., and Baso, A. (eds.), Earth Processes: Reading the Isotope Code, Amcan Geophyscal Union, Geophyscal Monograph Series 95, 429-437.

Tucker, M.E. 2001. Sedimentary Petrology. Third Edition. Blackwell, Oxford, pp. 1-262.

Valley, J. W., Kinny, P. D., Schulze, D. J., Spicuzza, M. J., 1998. Zircon megacrysts from kimberlite: oxygen isotope variability among mantle melts. Contributions to Mineralogy and Petrology 133, 1-11.

Valley, J.W., Lackey, J.S., Cavosie, A.J., Clechenko, C.C., Spicuzza, M.J., Basei, M.A.S., Bindeman, I.N., Ferreira, V.P., Sial, A.N., King, E.M., Peck, W. H., Sinha, A.K., Wei, C.S., 2005. 4.4 billion years of crustal maturation: oxygen isotope ratios of magmatic zircon. Contributions to Mineralogy and Petrology, 150, 561-580.

Warren, L. V., Freitas, B. T., Riccomini, C., Boggiani, P. C., Quaglio, F., Simões, M. G., Fairchild, T.R., Giorgioni, M., Gaucher, C., Poiré, D.G., Cáceres, A.A., Sial, A.N., 2019. Sedimentary evolution and tectonic setting of the Itapucumi Group, Ediacaran, northern Paraguay: from Rodinia break-up to West Gondwana amalgamation. Precambrian Research 322, 99-121.

Whittaker, E. J. W., Zussman, J., 1956. The characterization of serpentine minerals by X-ray diffraction. Mineralogical Magazine and Journal of the Mineralogical Society, 31, 107-126.

Will, T. M., Gaucher, C., Ling, X.X., Li, X.H., Li, Q. L., Frimmel, H.E., 2019. Neoproterozoic magmatic and metamorphic events in the Cuchilla Dionisio Terrane,

Uruguay, and possible correlations across the South Atlantic. Precambrian Research 320, 303-322.

Will, T.M., Höhn, S., Frimmel, H.E., Gaucher, C., le Roux, P.J., Macey, P.H. 2020. Petrological, geochemical and isotopic data of Neoproterozoic rock units from Uruguay and South Africa: Correlation of basement terranes across the South Atlantic. Gondwana Research 80, 12-32.

Winchester, J.A., Floyd, P.A., 1977. Geochemical discrimination of different magma series and their differentiation products using immobile elements. Chemical Geology 20: 325-343.

Winter, J.D., 2001. An introduction to igneous and metamorphic petrology. Prentice-Hall, New Jersey, pp. 1-700.

Winter, J.D., 2014. Principles of igneous and metamorphic petrology. Second Edition. Pearson, Harlow, pp. 1-738.

Wu, F.Y., Yang, Y.H., Xie, L.W., Yang, J.H., Xu, P., 2006. Hf isotopic compositions of the standard zircons in U-Pb geochronology. Chemical Geology 234, 105–126.

Zartman, R.E., Doe, B.R., 1981. Plumbotectonics –the model. Tectonophysics, 75, 135-162.

Figure captions

Fig. 1. (**A**) Geological sketch map of the Nico Pérez Terrane showing the main units (modified from Bossi and Cingolani, 2009). (**B**) Total count airborne radiometry (DINAMIGE, 2015) of the area indicated in A, showing the main lineaments and a NE-trending, low gamma-ray intensity, continuous band (blue colors) which corresponds to the Mesoproterozoic volcanosedimentary succession. 1208±10 Ma: K-Ar age of metabasic rocks (Gómez Rifas, 1995). Most felsic rocks are characterized by bright red colours. (**C**) Potassium concentration, airborne gamma-ray spectrometric image (DINAMIGE, 2015) of the area indicated in B. Note the folding and deformation of the low-K Mesoproterozoic succession (in blue) against the dextral Sarandí del Yí Shear Zone (SYSZ), interpreted here as a drag fold. The SYSZ was sinistrally reactivated in the latest Ediacaran-Cambrian (e.g. Bossi and Campal, 1992, Oriolo et al., 2016).

Fig. 2. (**A**) Geological map of the studied area, modified from Gaucher et al. (2014b), showing the location of the main outcrops. Lineaments: CPT: Cerro Partido Thrust, PPAL: Puntas Pan de Azúcar Lineament, SBSZ: Sierra Ballena Shear Zone, SSSZ: Sierra de Sosa Shear Zone, ZT: Zapicán Thrust. Ages indicated are: (1) Zapicán Thrust (K-Ar on muscovite, Bossi and Cingolani, 2009), (2) Puntas del Santa Lucía Batholith (U-Pb SHRIMP on zircon, Hartmann et al., 2002), (3) Lavaderos Granite (U-Pb SIMS on zircon, Gaucher et al., 2014c). (**B**) AA' cross section of the Tapes Group indicated on the map, located to the SW of Mariscala.

Fig. 3: Outcrops of the Tapes Complex. (**A**) Metapelitic quartz-chlorite schist at MAR 52. (**B**) Normal size grading between greywacke (Gw) and pelite (Pl), same outcrop as previous. (**C**) Banded chert mit stratabound pyrite, site MAR 26. Height of sample: 7 cm. (**D**) Metapelitic quartz-chlorite schist with preserved sedimentary lamination, MAR 13. Scale is divided in mm. (**E**) Marl-pelite metarhythmite, point MAR 52. (**F**) Serpentinite (Sp) passing into talc schist (Ts), La Serrana quarry (site CPA 146=CPA 148, Fig. 2). Shown hammer is 40 cm long. (**G**) Chloritic talc schist with cm-sized tremolite porphyroblasts, CPA 146. Shown scale (left) is divided in mm. (**H**) Serpentinite (Sp) pod dipping 45° to the left and surrounded by talc schist (Ts), CPA 148. Length of hammer in the center: 1 m.

Fig. 4. Microphotographs of thin sections of metaultramafic and metabasic rocks of the Tapes Complex, except for G all in crossed nicols. (**A**) Olivine relict (Ol) surrounded by tremolite (Tr) and talc (Tc) in tremolitite, sample 011021/8. (**B**) Same sample as previous, showing reaction rim of olivine (Ol) passing into tremolite (Tr) and serpentine (Sp). (**C**) Tremolitite with coarse tremolite crystals (Tr) and interstitial chlorite (Chl). (**D**) Serpentinite with typical interpenetrating texture, sample 030221/1a (site CPA 148). (**E**) Talc-schist with magnesian chlorite (center). (**F**) Chloritite from a black wall reaction zone, sample CPA 148b. (**G-H**) Metabasic sample with actinolite (Ac), epidote (Ep), sphene (Sph) and clinozoisite, sample MAR 44b (G in plane-polarized light).

Fig. 5: Microphotographs of thin sections of metasedimentary rocks of the Tapes Complex. All shown with crossed nicols, unless indicated. (**A-B**) Metagreywacke with plagioclase and metabasic lithoclasts in a fine-grained, chloritic matrix, sample MAR 27 (A in plane-polarized light). (**C**) Metagreywacke with metabasic (Bs) and epidote (Ep) clasts in a laminated, chloritic matrix, sample MAR 52e. (**D**) Detail of metabasic clast, showing ophitic texture with plagioclase laths immersed in large epidote crystals. (**E**) Preserved sedimentary lamination in quartz-chlorite schist (plane-polarized light). (**F**) Detail of previous, showing alternation of chlorite- and quartz-rich layers, as well as magnetite crystals. (**G**) Metamarl composed of carbonate (Ca) and epidote (Ep), and interbedded with quartz-chlorite layers (Qz-Chl). (**H**) Interbedded chlorite-schist and chert.

Fig. 6. Outcrop photographs (A-B) and thin sections (C-F) of the Tapes Chico Syenite. (**A**) Porphyritic quartz syenite. (**B**) Quartz syenite at the dated outcrop MAR 51, with an amphibolite xenolith. (**C**) Euhedral hornblende between large alkali feldspar and plagioclase phenocrysts, plane-polarized light. (**D**) Thin section from MAR 51, showing perthitic orthoclase, plagioclase, quartz and hornblende, crossed nicols. (**E**) Granite with interstitial hornblende and biotite between large microcline, perthitic orthoclase and plagioclase crystals, as well as quartz (crossed nicols). (**F**) Sphene in quartz syenite (crossed nicols).

Fig. 7. Major element composition of Tapes Complex rocks. (**A-F**) Major elements versus silica concentration for rocks with ultrabasic, basic and sedimentary protolith. (**G**) Alkali vs. silica diagram of Le Maitre et al. (1989), showing composition of basic rocks and dated Tapes Chico quartz-syenite.

Fig. 8. Rare Earth Element (REE) distribution for analyzed samples of the Tapes Complex. (**A**) PAAS-normalized REE+Y distribution for metasedimentary (black) and metabasic rocks (green). (**B**) Chondrite-normalized REE patterns for metasedimentary (black) and metabasic rocks (green) and N-MORB, E-MORB and OIB basalts (Sun and McDonough, 1989). (**C**) Chondrite-normalized REE patterns for metaigneous rocks. (**D**) Detail of previous, showing the samples with low REE concentration in more detail.

Fig. 9. Frequency of Nd model ages for both metasedimentary and metaigneous rocks of the Tapes Complex, and corresponding Nd evolution diagrammes. In the latter, typical fields of different terranes in Uruguay and southern Africa are shown (see Pamoukaghlián et al., 2017; Will et al., 2020, and references therein). The depleted mantle isotope evolution line (DMG) is after Goldstein et al. (1984), and the two-stage model ages are calculated according to Keto and Jacobsen (1987). CHUR: CHondritic Uniform Reservoir.

Fig. 10. Sm-Nd isochron diagram for mafic and ultramafic rocks of group 2 (see Fig. 9A-B), Tapes Complex.

Fig. 11. εNd (t) vs. $^{87}Sr/^{86}Sr$ diagram and $^{87}Sr/^{86}Sr$ versus Sr concentration plot for metasedimentary and metaigneous rocks of the Tapes Complex. Inferred alteration trends for metaultramafic and metabasic rocks are shown. The εNd composition of the CHUR (0.512638, Jacobsen and Wasserburg, 1980), and the present-day $^{87}Sr/^{86}Sr$ composition of the UR (Uniform Reservoir of 0.7045, DePaolo and Wasserburg, 1976) are shown.

Fig. 12. (**A-B**) $^{207}Pb/^{204}Pb$ vs. $^{206}Pb/^{204}Pb$ and $^{208}Pb/^{204}Pb$ vs. $^{206}Pb/^{204}Pb$ present-day ratios of Tapes Complex samples. Fields according to Zartman and Doe (1981). The "lower crust" field, in which most samples plot, is highlighted. (**C**) $^{207}Pb/^{204}Pb$ vs. $^{206}Pb/^{204}Pb$ diagram for six samples (four from the Mariscala and two from the Zapicán area) with mafic and ultramafic protolith, which define a linear array and a calculated μ of 9.808 and an age of ca. 2100 Ma for separation from their common source area.

Fig. 13. Upper panel: U-Pb SIMS zircon age of the Tapes Chico Syenite, quartz syenite sample U16-21 from site MAR 51 (Fig. 2). Lower panel: $\delta^{18}O$ versus age for analyzed zircons with 95-105 % concordance. The grey band indicates the syenite age and its 2σ uncertainty. The average mantle $\delta^{18}O$ value is 5.3 ± 0.6 ‰ VSMOW according to Valley et al. (1998).

Fig. 14. U-Pb SIMS detrital zircons ages for metagreywacke MAR 27 (Fig. 2). (A) Concordia diagram of the analyzed grains. (B) Zircon age spectrum and relative age probability curve. (C) SEM-BSE images of analyzed grains, location of spots and corresponding $^{238}U/^{206}Pb$ ages.

Fig. 15. $^{207}Pb/^{204}Pb$ vs. $^{206}Pb/^{204}Pb$ diagram for galena deposits of the PUG (La Oriental and Valencia mines), showing an intercept with the growth curve at 1242 Ma, interpreted here as dating metamorphism and deformation (data from Bossi and Navarro, 2001, see text).

Fig. 16. Comparison between sedimentary provenance data of the Tapes Complex and the Calymmian volcanosedimentary units (Mina Verdun and Parque UTE groups). (**A**) Th-Sc-Zr/10 plot of Bhatia and Crook (1985) for 1.43 Ga samples of the MVG (data from Poiré et al., 2005) and the younger, ca. 1.3 Ga Tapes Complex. Note the shift toward less evolved sources. (**B**) Chondrite-normalized REE patters for pelites of the MVG (grey field, Poiré et al., 2005) and greywackes (080204/2-3 and MAR48/2) and pelite (080204/5) of the Tapes Complex. Samples of the latter unit lack a negative Eu anomaly (arrowed). (**C**) Comparison between $^{238}U/^{206}Pb$ detrital zircon ages of the 1.48-1.43 Ga PUG (Mallmann et al., 2007) and the Tapes Complex. Note younger ages close to the age of the Namaqua orogeny of the latter samples and the absence of Paleoproterozoic-Archean zircon ages in these rocks. The age ranges of South American and southwestern African orogenic cycles that are known from the NPT are indicated.

Fig. 17. (A) Geological evolution (simplified) of the Nico Pérez and Apiaí terranes (data from Siga Jr. et al. 2011, Campanha et al., 2008, 2015, 2019). Key: (1) shelf succesion, (2) glacial rocks, (3) extensional environment, (4) compressional setting, (5) orogenic event. (B) Geological map of southern Brazil and Uruguay, showing the Ribeira and Dom Feliciano belts, Río de la Plata and São Francisco Cratons (modified from Passarelli et al., 2011). CFT: Cabo Frío Terrane, CT: Curitiba Terrane, JFT: Juiz de Fora Terrane, PST: Paraíba do Sul Terrane, SGT: São Gabriel Terrane, TT: Tandilia Terrane. Key: (1) Brusque and Porongos groups, (2) Votuverava Group. Note the likely displacement of the NPT to the NW along the Ibaré Shear Zone (ISZ), and possible continuation in the Apiaí Terrane further to the NE.

Fig. 18. Tectonostratigraphic map of SE South America and southern Africa, in a pre-drift Gondwana configuration, modified from Gaucher et al. (2005). Southern African terranes/subprovinces (Cornell et al., 2006; Miller, 2008; Frimmel et al., 2013; Macey et al., 2017; Hall et al., 2018): KT: Konkiep Terrane, MT: Marmora Terrane, MmT: Malmesbury Terrane, RT: Richtersveld Terrane/Subprovince. RBI: Rehoboth Basement Inlier. Southern African shear zones (SZ, Cornell et al., 2006): BRSZ: Boven Rugzeer, BTSZ: Brakbosch-Trooilapspan, NSZ: Neusberg, PSZ: Pofadder, PWSZ: Piketberg-Wellington. ST: Schakalsberge Thrust. South American terranes are after Bossi and Cingolani (2009), Gaucher et al. (2011), Ramos et al. (2018), Will et al. (2019) and Ballivián Justiniano et al. (2020): CDT: Cuchilla Dionisio Terrane, NPT: Nico Pérez Terrane, PAT: Piedra Alta Terrane, TT: Tandilia Terrane. South American shear zones: CSZ: Colonia, DCSZ: Dorsal de Canguçú, ISZ: Ibaré, SBSZ: Sierra Ballena, SYSZ: Sarandí del Yí (only main dextral event shown), SVSZ: Sierra de la Ventana. U-Pb ages of 1392 Ma and 1187 Ma for gabbros in the western PAT according to Santos et al. (2017).

Fig. 19. Tentative geodynamic model for the assembly and amalgamation of the Río de la Plata and Kalahari cratons. PUG: Parque UTE Group. MVG: Mina Verdún Group. Proto-CDT: Proto-Cuchilla Dionisio Terrane (protoliths of the Cerro Olivo Complex). RT: Richtersveld Terrane. SYSZ: Sarandí del Yí Shear Zone. For the 1.48-1.40 Ga interval the two competing hypotheses are presented (see text).

1860

1861 **Table 1**. Lithogeochemical data for metasedimentary and metaigneous rocks of the
1862 Tapes Complex.

1863 **Table 2**. Sm-Nd whole rock isotope data for the Tapes Complex. Preferred T_{DM} values
1864 are indicated in bold numbers.

1865 **Table 3**. Summary of Rb-Sr and Pb-Pb whole rock isotope data for the Tapes Complex.

1866 **Table 4.** U-Pb SIMS zircon data for samples MAR 27 (metagreywacke of the Tapes
1867 Complex) and U-16-21 (Tapes Chico Syenite), and zircon O and Hf isotope data of the
1868 latter.

1869

1870

1871

Sample	**011021/8**	**030221/1a**	**080204/2**	**080204/3**	**080204/5**	**080204/6**	**020131/5**	**CPA172/2**	**CPA172/3**	**254-4[a]**	**254-7[a]**	**MAR22**	**MAR44b**	**MAR48/2**	**562[b]**	**472[b]**
Point	MAR 15	CPA 148	MAR 25	MAR 27	MAR 30	MAR 33	CPA 147	CPA 172	CPA 172	CPA 254	CPA 254	MAR 22	MAR 44	MAR 48	~ZAP 42	~ZAP 42
Lithology	Olivinic tremolitite	Serpenti-nite	Metagrey-wacke	Metagrey-wacke	Meta-pelite	Meta-basite	Chloritic tremolitite	Tremolitite	Talc-chlor. schist	Chlor. talc schist	Chlorite talc schist	Metamarl	Meta-basite	Metagrey-wacke	Serpentinite	Talc schist
Major elements (wt. %)																
SiO_2	51.58	43.15	46.22	51.37	49.82	46.79	49.19	57.43	37.29	52.54	51.67	48.87	48.53	48.52	38.44	37.88
Al_2O_3	0.27	1.33	12.93	15.97	15.29	16.79	4.85	0.81	12.81	5.47	5.42	9.92	6.32	13.62	2.16	2.61
Fe_2O_3(T)	7.56	7.14	11.51	10.76	16.17	8.25	5.4	5.44	8.3	6.85	7.46	7.19	16.76	11.52	15.88	13.59
MnO	0.119	0.078	0.16	0.123	0.251	0.117	0.173	0.134	0.06	0.06	0.06	0.213	0.196	0.185	0.18	0.16
MgO	26.9	35.09	11.18	6.3	2.66	7.05	24.33	21.4	29.63	27.44	26.83	8.4	10.04	5.96	29.94	32.3
CaO	8.5	0.06	6.09	3.08	1.96	15.9	8.04	12.21	0.1	0.46	0.62	19.13	14.27	5.89	2.13	1.7
Na_2O	0.06	0.02	2.14	4.08	4.25	1.21	0.08	0.17	0.01	0.05	0.03	0.6	0.25	3.19	0.01	0.05
K_2O	0.02	0.02	0.09	0.16	1.21	0.04	0.04	0.05	0.01	0.04	< 0.01	0.71	0.1	0.56	0.01	0.03
TiO_2	0.007	0.051	0.778	1.221	3.872	0.549	0.081	0.028	0.117	0.317	0.3	0.32	0.502	1.826	0.5	0.31
P_20_5	0.03	0.02	0.12	0.2	0.73	0.08	< 0.01	< 0.01	0.03	0.26	0.27	0.07	0.13	0.34	0.08	0.04
LOI	4.18	11.15	6.67	5.38	3.92	2.75	5.97	2.69	11.29	6.58	7.22	4.55	1.61	8.46	9.61	9.94
Total	99.23	98.11	97.9	98.63	100.1	99.52	98.15	100.4	99.65	100.1	99.87	99.96	98.71	100.1	98.92	98.61
Trace elements (ppm)																
Sc	3	5	20	22	16	41	5	4	14	14.1	13.6	8	12	16	na	na
V	11	19	120	152	183	223	15	18	41	76	59	46	108	145	33.8	64.3
Cr	1920	1520	540	360	< 20	210	960	850	< 20	2430	2390	50	70	80	520.8	888.2
Co	100	77	72	42	35	24	51	27	89	76	75	13	30	37	39.7	138.3
Ni	1690	2570	600	160	< 20	80	1270	1730	2070	1090	1090	20	50	80	909.5	2390
Rb	< 1	< 1	< 2	4	22	< 2	< 2	< 2	< 2	< 20	< 20	6	< 2	8	<2	<2
Sr	111	< 2	126	288	108	165	18	10	3	22	32	194	259	292	102.9	24.8
Y	4.9	1.6	10	20	29	13	12	4	2	4	6	20	18	18	12.4	5.8
Zr	4	6	49	117	328	30	8	7	16	53	50	92	45	138	47.1	24.3
Nb	< 0.2	0.3	5	12	35	2	8	< 1	2	na	na	4	5	15	na	na
Ba	895	5	63	84	444	11	7	6	4	7	30	197	26	267	<3	5.4
La	8.7	0.85	9.7	32.4	37.3	3.4	1.3	1.5	1.2	6.2	15.5	19.1	11.8	25	6.1	3.3
Ce	3.73	1.86	17.1	55.7	73.1	4.9	2.5	3.1	1.4	17	17	34	38.4	47.3	11.6	6.1
Pr	1.13	0.24	2.36	7.4	9.36	0.96	0.7	0.29	0.38	na	na	4.14	6.19	6.13	1.4	0.8
Nd	4.1	0.86	10.6	29.4	39.1	4.6	3.8	1.1	1.8	< 5	12	15.5	25.5	26.1	6.3	4

Sm	0.62	0.23	2.7	5.6	8.7	1.4	1.3	0.3	0.4	1.7	2.7	3	4.1	5.8	1.6	1
Eu	0.173	0.049	0.91	1.64	2.11	0.6	0.15	0.07	0.06	0.5	0.7	0.49	1.48	2.13	0.5	0.4
Gd	0.7	0.23	2.5	4.6	7.6	1.7	1.3	0.4	0.4	na	na	2.5	2.9	4.9	na	na
Tb	0.09	0.04	0.4	0.7	1.1	0.3	0.3	< 0.1	< 0.1	< 0.5	< 0.5	0.4	0.4	0.8	na	na
Dy	0.45	0.2	2.1	3.8	6.1	2.1	1.7	0.4	0.3	na	na	2.6	2.6	3.8	na	na
Ho	0.09	0.04	0.4	0.7	1.2	0.4	0.4	0.1	< 0.1	na	na	0.6	0.5	0.7	na	na
Er	0.25	0.12	1	1.8	3.1	1.2	1	0.3	0.2	na	na	1.7	1.5	1.7	na	na
Tm	0.036	0.042	0.17	0.28	0.44	0.22	0.19	0.08	0.05	na	na	0.31	0.24	0.28	na	na
Yb	0.23	0.14	0.9	1.5	2.5	1.2	1.1	0.4	0.2	0.6	0.7	1.6	1.3	1.3	na	na
Lu	0.031	0.023	0.13	0.21	0.33	0.18	0.17	0.06	< 0.04	0.07	0.08	0.22	0.18	0.19	na	na
Hf	0.1	0.1	1.3	2.8	7.6	0.8	0.3	< 0.2	0.5	1	1	2.2	1.1	3.2	na	na
Ta	0.03	0.06	0.3	0.8	2.7	0.4	0.9	< 0.1	0.2	< 1	< 1	0.2	0.3	1	0.2	<0.1
Pb	< 5	< 5	< 5	< 5	< 5	< 5	< 5	< 5	< 5	< 5	< 5	6	10	< 5	<5	28.7
Th	0.11	0.2	0.6	1.6	4.3	0.2	0.3	0.3	1.3	2.3	2	6.2	2.4	1.6	0.7	0.3
U	0.07	0.99	0.1	0.4	0.8	0.1	< 0.1	< 0.1	< 0.1	0.9	< 0.5	1.2	1.3	0.3	0.3	<0.1

[a] From Gaucher et al. (2014b)
[b] From Bossi and Schipilov (2007)
na: not analyzed

Sample	Point	Lithology	Lab[a]	Assumed age (Ma)	Sm (ppm)	Nd (ppm)	$^{143}Nd/^{144}Nd$	$^{147}Sm/^{144}Nd$ measured	$^{147}Sm/^{144}Nd$ calculated	εNd (0)	$^{143}Nd/^{144}Nd$ initial	εNd (t)	T_{DM}, [b] 1-stage	T_{DM}, [c] 2-stage
Metamafic/ultramafic rocks														
011021/8	MAR 15	Olivinic tremolitite	1	1400	0.71	4.84	0.511771	0.08936	0.08859	-16.91	0.510956	2.49	**1678**	
020131/5	CPA 147	Tremolitite	1	1400	1.56	4.91	0.511751	0.19202	0.191871	-17.3	0.509986	-16.49	9924	**3338**
080204/6	MAR 33	Epidotic tremolitite	1	1400	1.44	4.69	0.512796	0.18583	0.185466	3.08	0.51109	5.12	1908	**1549**
CPA 80	CPA 80	Actinolitite	2	1400	2.9	12.3	0.511596	0.144149	0.142378	-20.33	0.510286	-10.62	3329	**2838**
CPA 148	CPA 148	Serpentinite	2	1400	4.4	24.2	0.511505	0.110214	0.109794	-22.1	0.510495	-6.53	**2414**	
CPA 172/2	CPA 172	Tremolitite	1	1400	0.35	1.95	0.510967	0.10685	0.108373	-32.6	0.50997	-16.81	3167	**3345**
MAR 17	MAR 17	Tremolitite	2	1400	3.7	16.5	0.51177	0.135926	0.135421	-16.93	0.510524	-5.96	2690	**2455**
MAR 21b	MAR 21	Actinolitite	2	1400	0.6	3.6	0.510982	0.109504	0.100632	-32.3	0.510056	-15.12	**2928**	
MAR 44 b	MAR 44	Epidotic amphibolite	1	1400	4.96	31.72	0.511408	0.0947	0.094424	-23.99	0.510539	-5.66	2227	**2431**
MAR 47/1	MAR 47	Tremolitite	1	1400	0.65	2.25	0.511678	0.17464	0.174458	-18.73	0.510073	-14.79	5760	**3186**
MAZ 47/1	MAZ 47	Tremolitite	1	1400	0.83	3.01	0.511686	0.16704	0.166522	-18.57	0.510154	-13.2	4755	**3053**
ZAP 26	ZAP 26	Microgabbro	2	1400	15.1	88.3	0.511068	0.103319	0.103256	-30.63	0.510118	-13.91	**2878**	
ZAP 42	ZAP 42	Serpentinite	1	1400	0.82	3.12	0.511986	0.15846	0.158727	-12.72	0.510526	-5.93	3234	**2453**
ZAP 42	ZAP 42	Serpentinite	1	1400	0.74	2.83	0.511976	0.15821	0.157919	-12.91	0.510523	-5.98	3214	**2457**
ZAP 43	ZAP 43	Tremolitite	1	1400	2.27	8.03	0.511821	0.15234	0.17072	-15.94	0.510251	-11.32	4737	**2897**
ZAP 43	ZAP 43	Tremolitite	1	1400	2.53	7.69	0.511826	0.15216	0.198687	-15.84	0.509998	-16.25	13757	**3328**
ZAP 44 b	ZAP 44	Talc schist	1	1400	1.87	7.04	0.511452	0.16069	0.1604	-23.14	0.509977	-16.68	4884	**3339**
Zuccolo	CPA 154	Talc schist	1	1400	0.28	1.2	0.51172	0.14219	0.14091	-17.91	0.510424	-7.93	2999	**2616**
Metasedimentary rocks														
011021/15	MAR 17	Metawacke	1	1300	3.33	17.07	0.511691	0.11813	0.117807	-18.47	0.510685	-5.35	**2321**	
080204/2	MAR 25	Metagreywacke	1	1400	3.81	15.26	0.511958	0.15092	0.150785	-13.26	0.510571	-5.04	2892	**2380**
080204/3	MAR 27	Metagreywacke	1	1300	5.28	26.25	0.511565	0.1216	0.121465	-20.93	0.510528	-8.43	**2623**	
080204/9	MAR 45	Limestone	1	1300	0.71	3.79	0.511606	0.1128	0.113128	-20.13	0.51064	-6.23	**2342**	
CPA 68	CPA 68	Metawacke	2	1300	3.3	15	0.51157	0.13308	0.132853	-20.83	0.510436	-10.23	2985	**2724**
CPA 82	CPA 82	Metawacke	2	1300	2.1	9.6	0.511865	0.135561	0.132107	-15.08	0.510737	-4.33	2403	**2240**
CPA 87	CPA 87	Metagreywacke	2	1300	2.7	11.1	0.5115	0.147396	0.146887	-22.2	0.510246	-13.95	3779	**3030**
CPA 161b	CPA 161	Metawacke	2	1300	5.2	28.6	0.511032	0.110623	0.109782	-31.33	0.510095	-16.91	**3115**	

MAR 22 b	MAR 22	Limestone	1	1300	0.42	2.59	0.511561	0.09762	0.097926	-21.01	0.510725	-4.57	**2093**	
MAR 16	MAR 16	Metapelite	2	1300	9.8	45.5	0.511767	0.130103	0.130072	-16.99	0.510656	-5.91	2524	**2369**
MAR 20	MAR 20	Metawacke	2	1300	3.6	16.1	0.511485	0.134464	0.135026	-22.49	0.510332	-12.26	3235	**2890**
MAR 22	MAR 22	Marl	1	1300	3.5	18.2	0.511755	0.11619	0.116135	-17.22	0.510763	-3.82	**2180**	
MAR 22	MAR 22	Marl	1	1300	2.87	17.76	0.51176	0.1151	0.09759	-17.13	0.510927	-0.62	**1824**	
MAR 48/2	MAR 48	Metagreywacke	1	1400	4.7	22.23	0.511662	0.12802	0.127678	-19.04	0.510488	-6.68	**2639**	
MIN 50a	MIN 50	Biotite-chlorite schist	2	1300	4	20.4	0.511207	0.118758	0.118397	-27.91	0.510196	-14.92	**3116**	
MIN 50b	MIN 50	Metawacke	2	1300	6.4	42.6	0.510675	0.09111	0.090704	-38.29	0.509901	-20.71	**3076**	

[a]Laboratories: 1: University of Copenhagen, 2: Universidade Federal do Rio Grande do Sul
[b]1-stage Nd model ages were calculated according to Goldstein et al. (1984)
[c]For samples with $^{147}Sm/^{144}Nd>0.13$, the 2-stage Nd model of Keto and Jacobsen (1987) was used for calculation of the Nd model ages

Sample	Point	$^{87}Sr/^{86}Sr$	$\pm 2\sigma$ $*10^{-6}$	$^{206}Pb/^{204}Pb$	$\pm 2\sigma^{+}$	$^{207}Pb/^{204}Pb$	$\pm 2\sigma^{+}$	$^{208}Pb/^{204}Pb$	$\pm 2\sigma^{+}$	$^{207}Pb/^{206}Pb$	$\pm 2\sigma^{+}$	$^{208}Pb/^{206}Pb$	$\pm 2\sigma^{+}$	r_1 **	r_2 ††
011021/8	MAR 15	0.729396	9	17.652	0.020	15.515	0.019	37.154	0.049	0.87896	0.00034	2.10482	0.00092	0.951	0.945
011021/15	MAR 17	0.711905	8	18.323	0.058	15.364	0.050	40.959	0.133	0.83849	0.00037	2.23538	0.00107	0.991	0.989
020131/5	CPA 147	0.751763	6	17.575	0.022	15.310	0.020	39.920	0.055	0.87110	0.00018	2.27143	0.00085	0.987	0.964
080204/2	MAR 25	0.705677	9	16.664	0.025	15.173	0.023	37.392	0.060	0.91051	0.00025	2.24386	0.00092	0.985	0.967
080204/3	MAR 27	0.706251	6	16.962	0.030	15.211	0.027	38.412	0.071	0.89676	0.00024	2.26461	0.00090	0.989	0.977
080204/6	MAR 33	0.704832	7	16.504	0.031	15.357	0.029	36.863	0.072	0.93049	0.00027	2.23360	0.00092	0.989	0.978
080204/9	MAR 45	0.712540	5	18.437	0.030	15.659	0.026	37.825	0.065	0.84931	0.00018	2.05157	0.00079	0.992	0.975
CPA 172/2	CPA 172	0.737715	7	17.062	0.022	15.295	0.021	38.692	0.055	0.89644	0.00023	2.26770	0.00090	0.982	0.961
CPA 172/3	CPA 172	0.719576	6	22.507	0.028	15.714	0.021	64.085	0.090	0.69816	0.00016	2.84733	0.00113	0.986	0.960
MAR 22	MAR 22	0.717183	9	17.401	0.020	15.454	0.019	38.425	0.050	0.88813	0.00031	2.20826	0.00099	0.959	0.942
MAR 22 b	MAR 22	0.724397	7	19.620	0.023	15.668	0.019	41.429	0.054	0.79855	0.00028	2.11157	0.00089	0.959	0.949
MAR 44 b	MAR 44	0.717390	6	17.890	0.014	15.564	0.014	37.644	0.037	0.87000	0.00021	2.10425	0.00086	0.965	0.920
MAR 48/2	MAR 48	0.707751	8	18.543	0.037	15.620	0.032	39.421	0.083	0.84235	0.00024	2.12594	0.00082	0.990	0.983
MAZ 47/1	MAZ 47	0.719293	7	17.959	0.033	15.524	0.030	38.600	0.076	0.86444	0.00031	2.14941	0.00106	0.983	0.968
ZAP 42	ZAP 42	0.722431	7	18.145	0.025	15.561	0.022	39.004	0.060	0.85761	0.00023	2.14957	0.00116	0.982	0.937
ZAP 43	ZAP 43	0.709274	9	17.413	0.027	15.395	0.025	38.427	0.064	0.88409	0.00027	2.20678	0.00099	0.982	0.964
ZAP 44 b	ZAP 44	0.724827	7	17.553	0.013	15.638	0.013	41.715	0.041	0.89093	0.00021	2.37653	0.00104	0.963	0.905
Zuccolo	CPA 154	0.722334	15	20.567	0.062	15.369	0.047	37.852	0.116	0.74729	0.00026	1.84045	0.00080	0.993	0.990

** $r_1=^{206}Pb/^{204}Pb$ vs. $^{207}Pb/^{204}Pb$ error correlation (Ludwig, 1988)
†† $r_2=^{206}Pb/^{204}Pb$ vs. $^{208}Pb/^{204}Pb$ error correlation (Ludwig, 1988)
+Errors are two standard deviations absolute (Ludwig, 1988)
Fractionation of Pb was controled by repreated analysis of the SRM NBS 981 standard (values of Todt et al., 1993) and amounted to 0.103 +/- 0.007%/a.m.u. (2σ, n=5)

													Ages (Ma)						$\delta^{18}O$		εHf(t)	T_{DM}
Sample/ spot #	**[U] ppm**	**[Th] ppm**	**[Pb] ppm**	**Th/U**	**$^{207}Pb/^{235}U$**	**±σ %**	**$^{206}Pb/^{238}U$**	**±σ %**	**ρ**	**$^{207}Pb/^{206}Pb$**	**±σ %**	**$^{207}Pb/^{206}Pb$**	**±σ**	**$^{207}Pb/^{235}U$**	**±σ**	**$^{206}Pb/^{238}U$**	**±σ**	**Disc. %**	**‰ VSMOW**	**±σ**		**Ma**
Sample MAR 27-Tapes Complex metagreywacke																						
n3798-01	132.8	68.4	42.4	0.51	3.27876	1.44	0.25674	0.99	0.69	0.092624	1.05	1480.2	19.7	1476.0	11.3	1473.1	13.1	-0.5	na	na	na	na
n3798-02	324.5	30.1	104.7	0.09	3.92777	1.09	0.28647	1.00	0.92	0.099442	0.44	1613.7	8.1	1619.4	8.8	1623.9	14.3	0.7	na	na	na	na
n3798-03	253.3	116.3	72.5	0.46	2.75906	1.18	0.23492	0.99	0.84	0.085180	0.65	1319.6	12.5	1344.5	8.9	1360.2	12.2	3.4	na	na	na	na
n3798-04	163.8	199.3	66.1	1.22	3.78745	1.25	0.27745	0.99	0.79	0.099006	0.76	1605.5	14.1	1590.1	10.1	1578.5	13.9	-1.9	na	na	na	na
n3798-05	78.3	60.9	26.1	0.78	3.20764	1.48	0.25430	1.02	0.69	0.091482	1.08	1456.7	20.3	1459.0	11.6	1460.6	13.4	0.3	na	na	na	na
n3798-06	85.1	70.5	28.6	0.83	3.18522	1.50	0.25467	1.01	0.67	0.090710	1.11	1440.5	21.0	1453.6	11.6	1462.5	13.2	1.7	na	na	na	na
n3798-07	69.5	70.6	24.7	1.02	3.15864	1.63	0.25840	1.01	0.62	0.088654	1.28	1396.7	24.3	1447.1	12.7	1481.7	13.4	6.8	na	na	na	na
n3798-08	30.3	21.9	9.9	0.72	3.12014	2.02	0.25119	1.01	0.50	0.090089	1.75	1427.4	33.0	1437.7	15.6	1444.6	13.1	1.3	na	na	na	na
n3798-09	28.3	37.8	10.5	1.34	2.90348	2.83	0.25331	1.01	0.36	0.083130	2.64	1272.3	50.7	1382.8	21.6	1455.5	13.2	16.1	na	na	na	na
Sample U16-21-Tapes Chico quartz syenite																						
U16-21@1	133	229	20	1.72	0.79802	2.75	0.0963	2.46	0.89	0.06009	1.23	606.7	26.4	595.7	12.5	592.8	14.0	2.3	6.43	0.55	-26.32	2844
U16-21@02	124	388	24	3.14	0.79531	1.70	0.0963	1.51	0.89	0.05987	0.79	599.0	17.1	594.2	7.7	592.9	8.6	1	6.34	0.56	-30.39	3062
U16-21@03	120	176	18	1.47	0.81303	1.73	0.0979	1.50	0.87	0.06022	0.85	611.7	18.3	604.2	7.9	602.2	8.7	1.6	6.46	0.53	-29.01	2995
U16-21@05	191	284	29	1.49	0.81471	1.64	0.0984	1.51	0.92	0.06007	0.64	606.3	13.7	605.1	7.5	604.8	8.7	0.2	6.32	0.58	-27.05	2893
U16-21@06	182	275	28	1.51	0.82762	1.63	0.1001	1.50	0.92	0.05998	0.63	602.7	13.6	612.3	7.5	614.9	8.8	-2	5.45	0.56	-52.03	4221
U16-21@07	145	222	23	1.53	0.84686	2.07	0.1016	1.76	0.85	0.06048	1.10	620.8	23.5	622.9	9.7	623.5	10.4	-0.4	6.68	0.56	-30.81	3109
U16-21@08	91	87	12	0.96	0.80988	1.75	0.0990	1.50	0.86	0.05932	0.90	578.9	19.5	602.4	8.0	608.7	8.7	-5.1	6.02	0.56	-27.88	2941
U16-21@09	135	201	20	1.49	0.79481	1.72	0.0959	1.50	0.87	0.06009	0.83	606.9	18.0	593.9	7.8	590.5	8.5	2.7	6.46	0.55	-27.85	2924
U16-21@10	169	295	26	1.74	0.79714	1.76	0.0966	1.55	0.88	0.05985	0.84	598.2	18.0	595.2	8.0	594.4	8.8	0.6	6.44	0.55	-29.08	2993
U16-21@11	208	320	31	1.54	0.79696	1.63	0.0967	1.51	0.92	0.05978	0.63	595.5	13.5	595.1	7.4	595.0	8.6	0.1	6.54	0.53	-28.21	2947
U16-21@12	135	126	18	0.93	0.81036	1.79	0.0983	1.59	0.89	0.05982	0.82	596.9	17.7	602.7	8.2	604.2	9.2	-1.2	6.11	0.56	-28.8	2986
U16-21@13	123	136	16	1.10	0.76842	1.84	0.0933	1.56	0.85	0.05975	0.97	594.5	20.9	578.9	8.1	574.9	8.6	3.3	5.89	0.6	-27.69	2903
U16-21@14	63	44	8	0.70	0.82853	1.84	0.1006	1.50	0.82	0.05975	1.06	594.4	22.8	612.8	8.5	617.8	8.9	-3.9	6.21	0.53	-34.9	3322
U16-21@15	58	80	26	1.37	4.45162	1.59	0.2976	1.50	0.94	0.10848	0.53	1774.1	9.6	1722.0	13.3	1679.5	22.3	5.3	6.24	0.55	-12.75	3067
U16-21@04	55	47	23	0.85	4.55100	1.61	0.3073	1.50	0.93	0.10741	0.58	1756.0	10.6	1740.3	13.5	1727.4	22.8	1.6	na	na	-13.34	3084

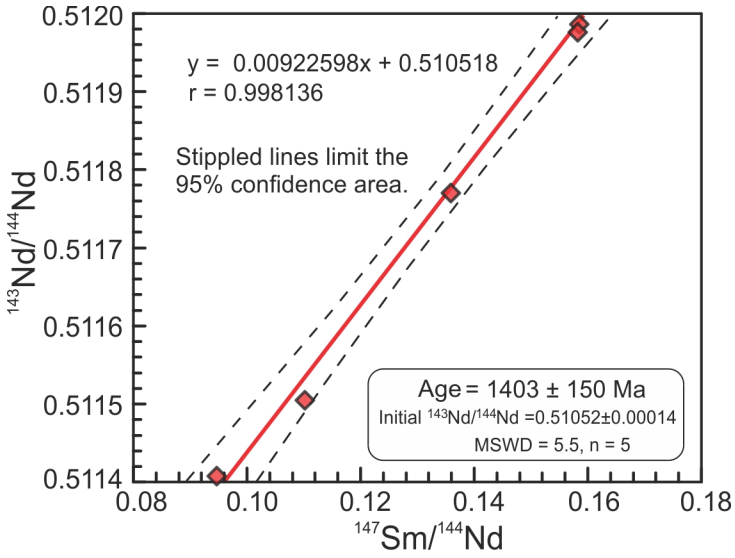

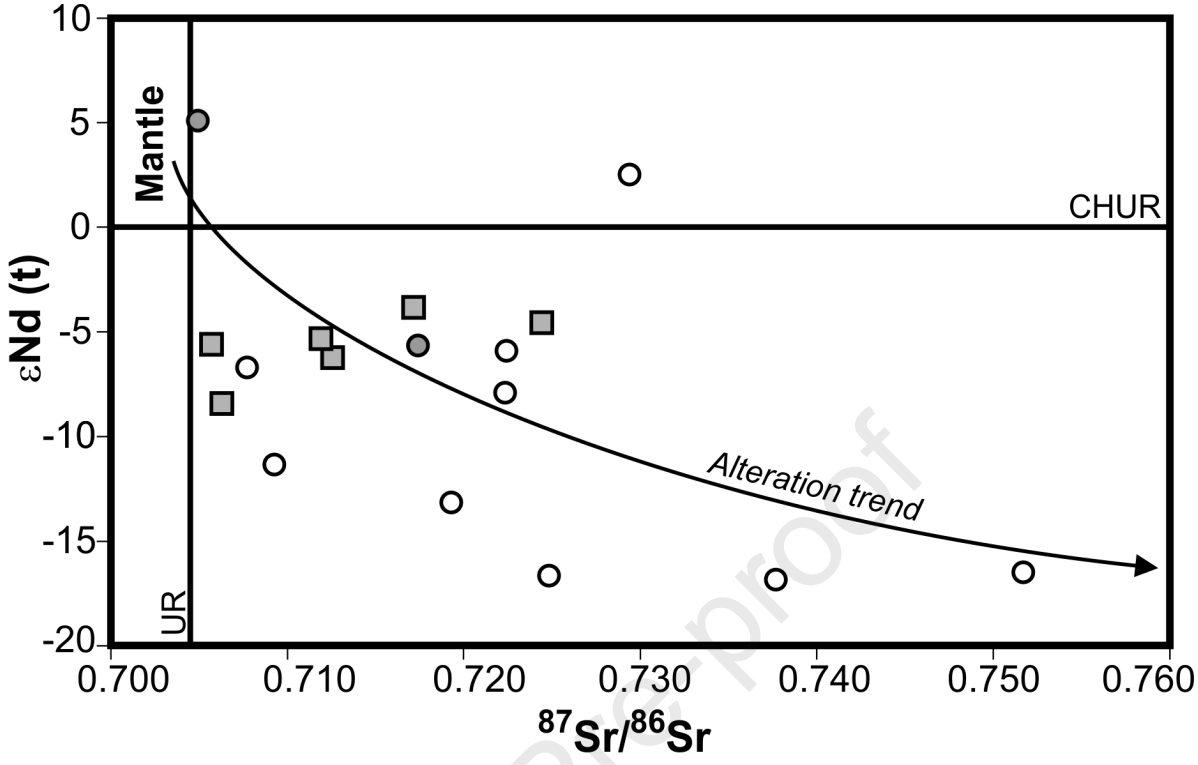

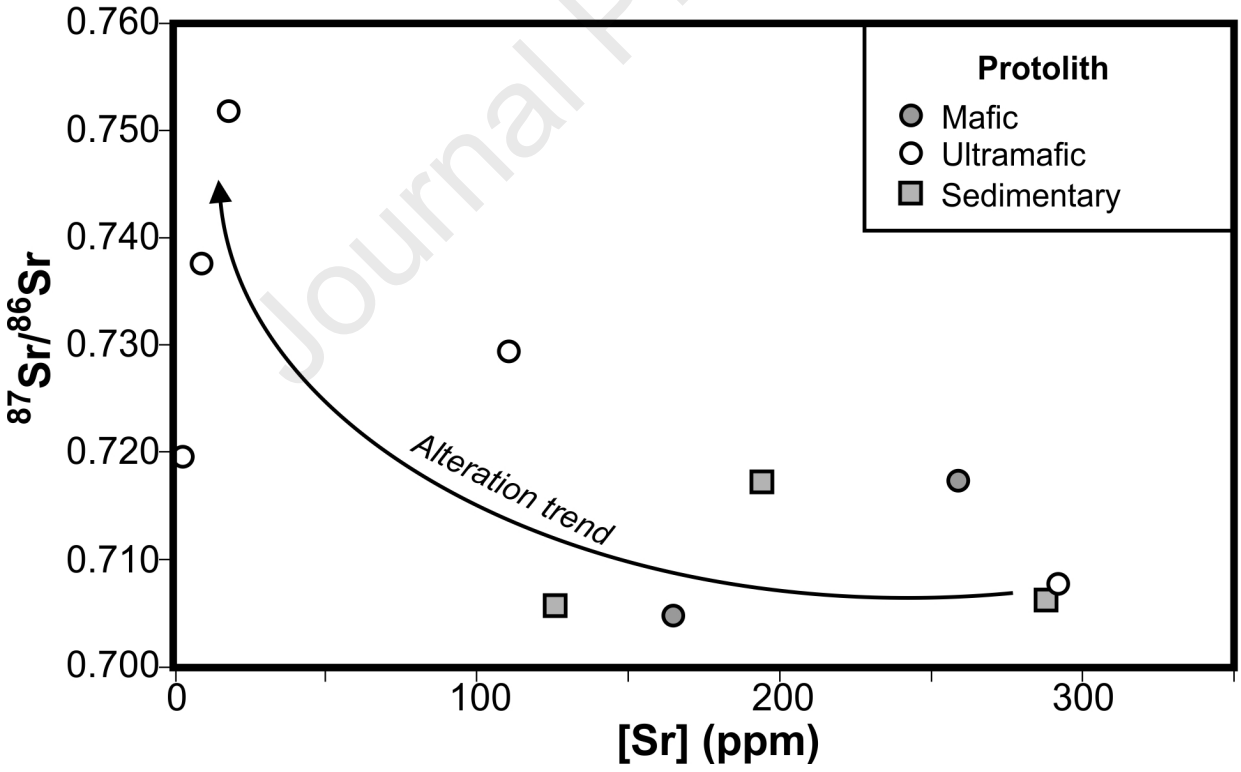

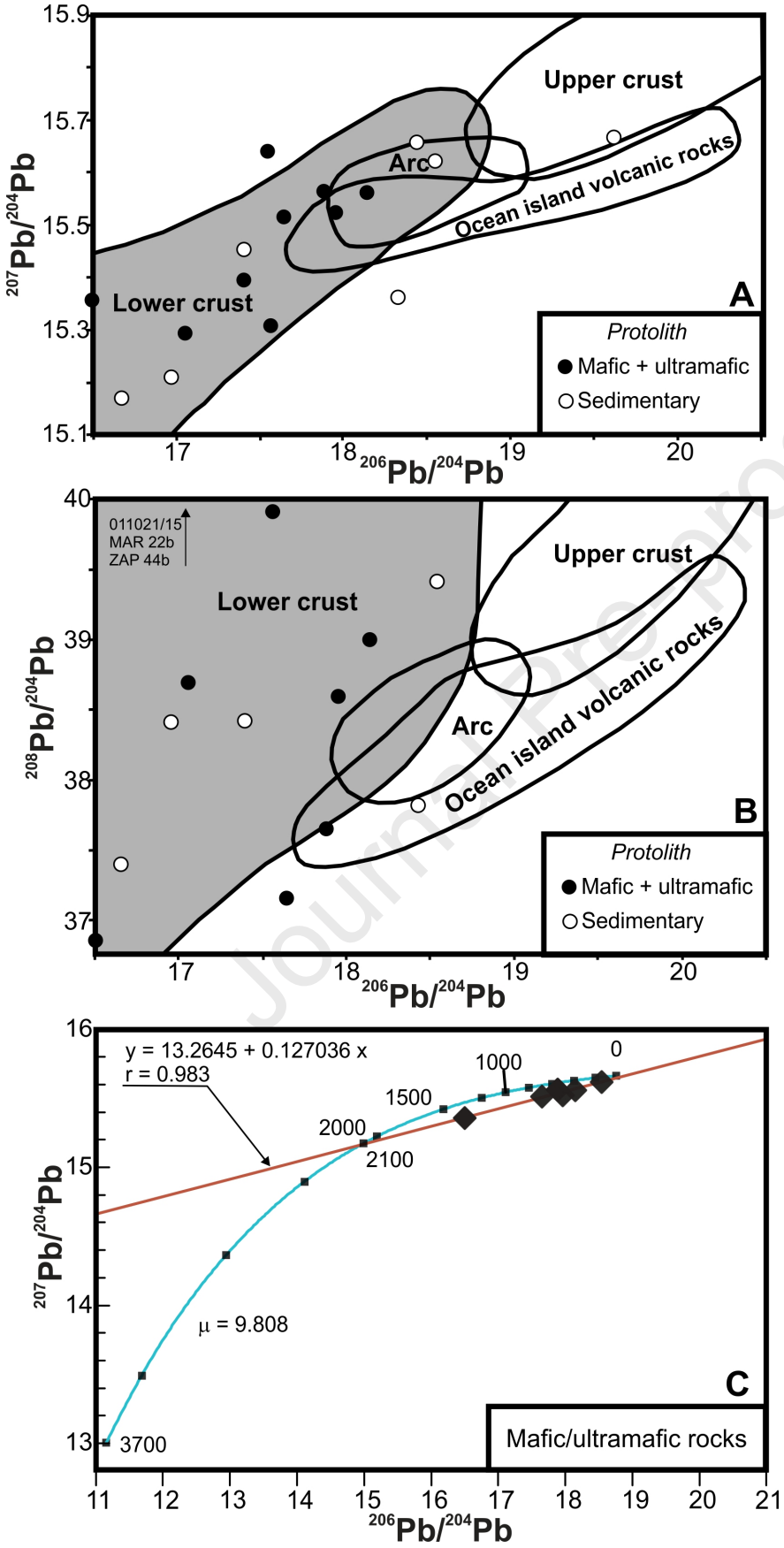
15.9
15.7
15.5
15.3
15.1
$^{207}Pb/^{204}Pb$
Upper crust
Arc
Ocean island volcanic rocks
Lower crust
A
Protolith
Mafic + ultramafic
Sedimentary
17
18
19
20
$^{206}Pb/^{204}Pb$
40
39
38
37
$^{208}Pb/^{204}Pb$
011021/15
MAR 22b
ZAP 44b
Upper crust
Lower crust
Arc
Ocean island volcanic rocks
B
Protolith
Mafic + ultramafic
Sedimentary
17
18
19
20
$^{206}Pb/^{204}Pb$
16
15
14
13
$^{207}Pb/^{204}Pb$
y = 13.2645 + 0.127036 x
r = 0.983
0
1000
1500
2000
2100
μ = 9.808
3700
C
Mafic/ultramafic rocks
11
12
13
14
15
16
17
18
19
20
21
$^{206}Pb/^{204}Pb$

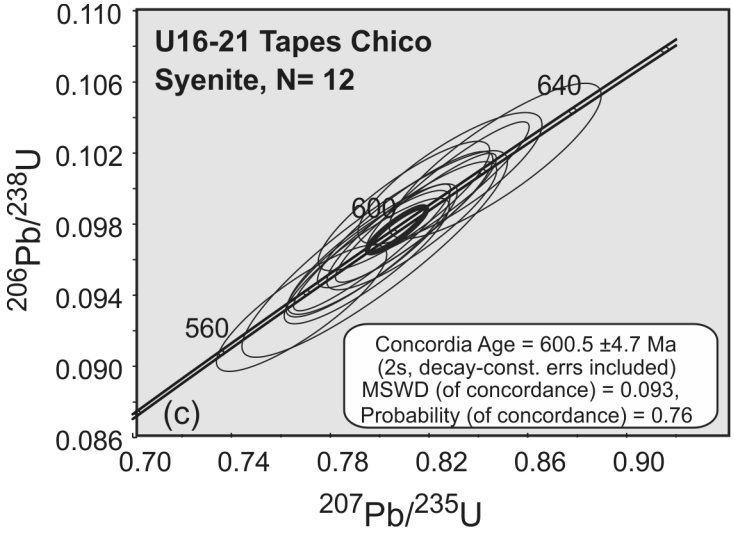

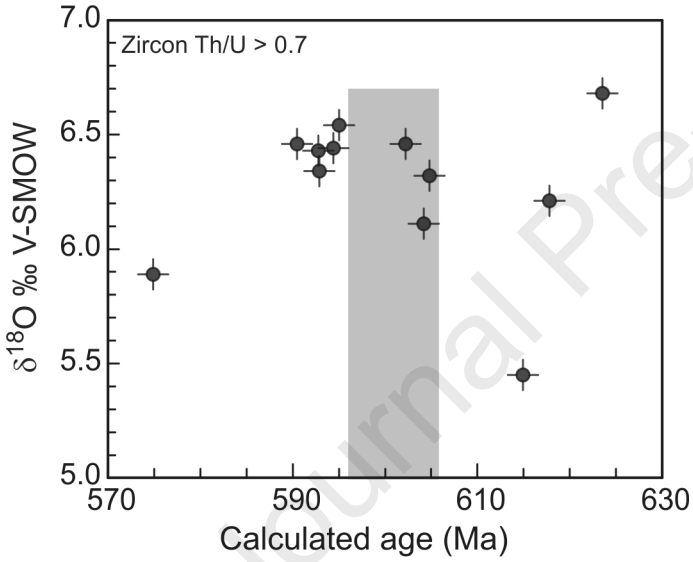

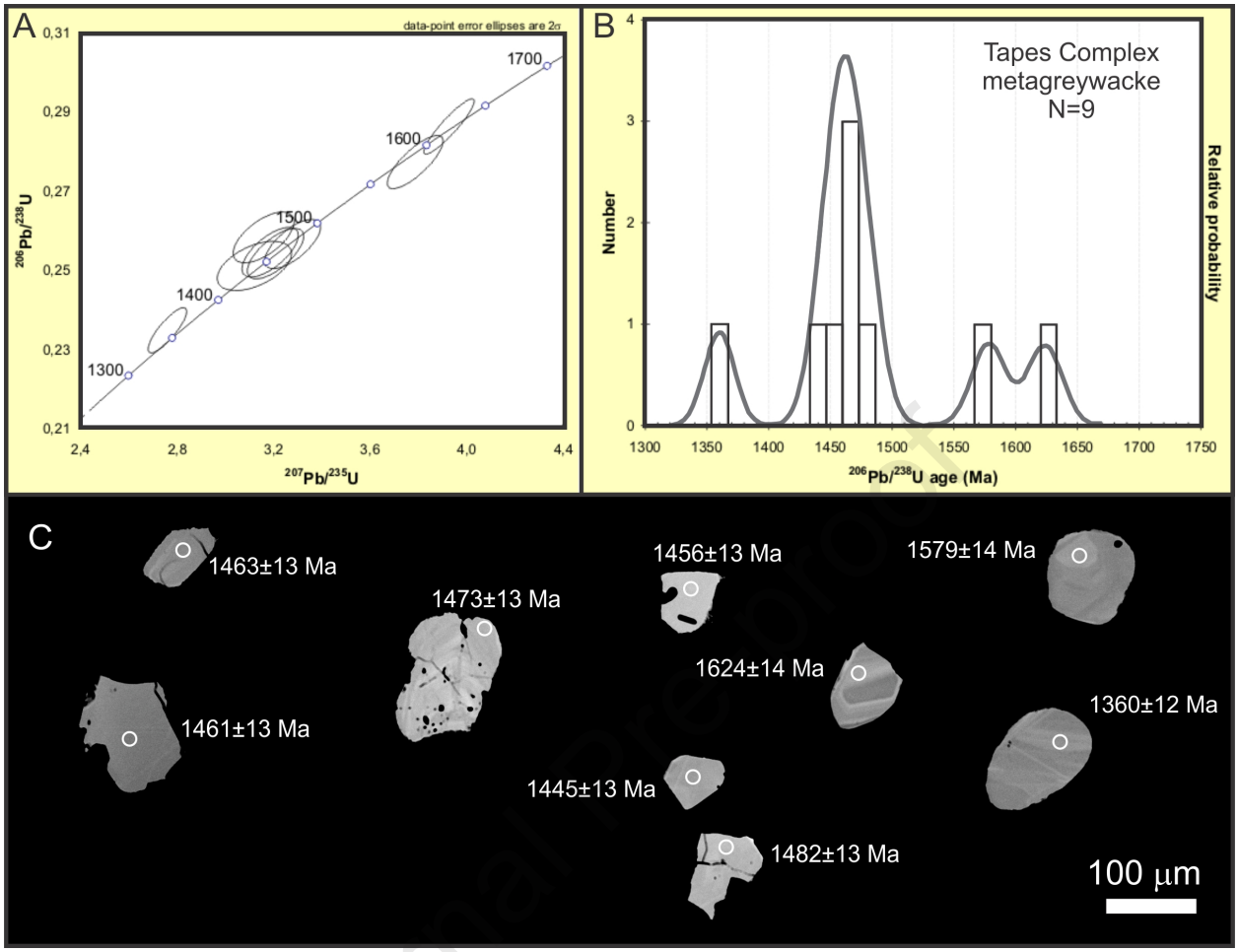

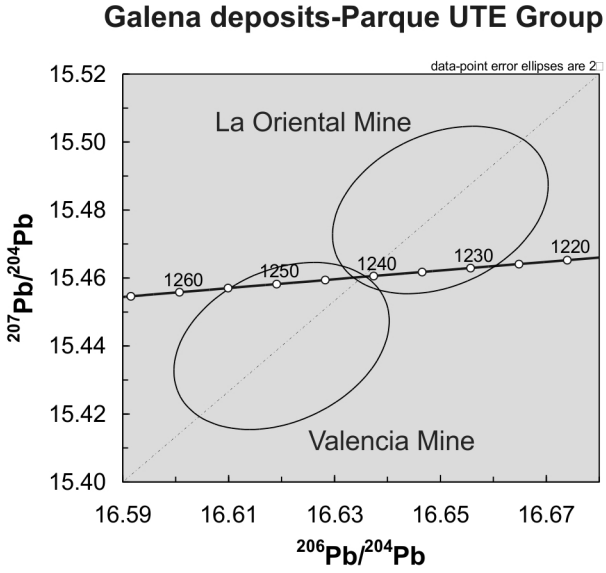

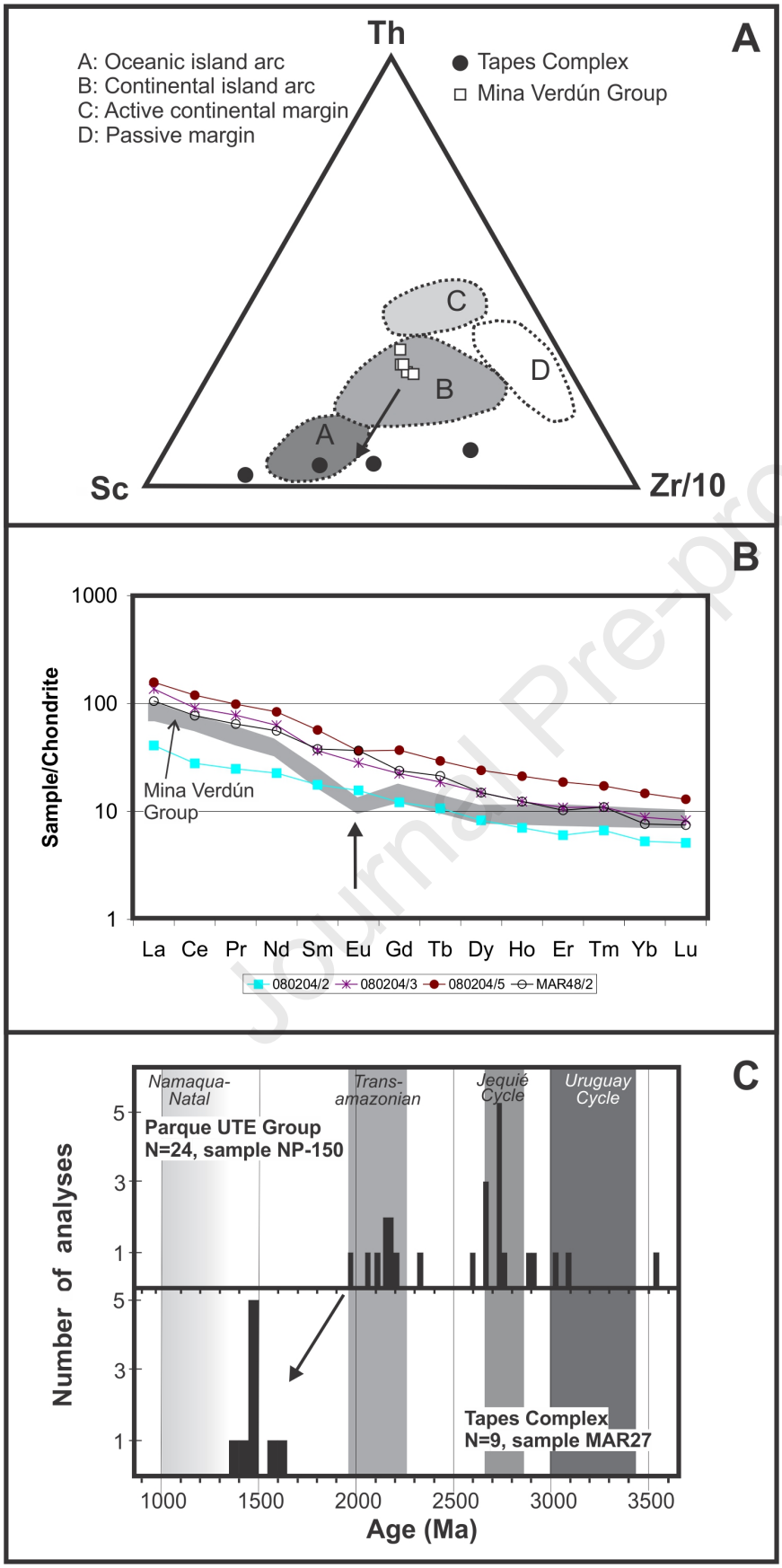

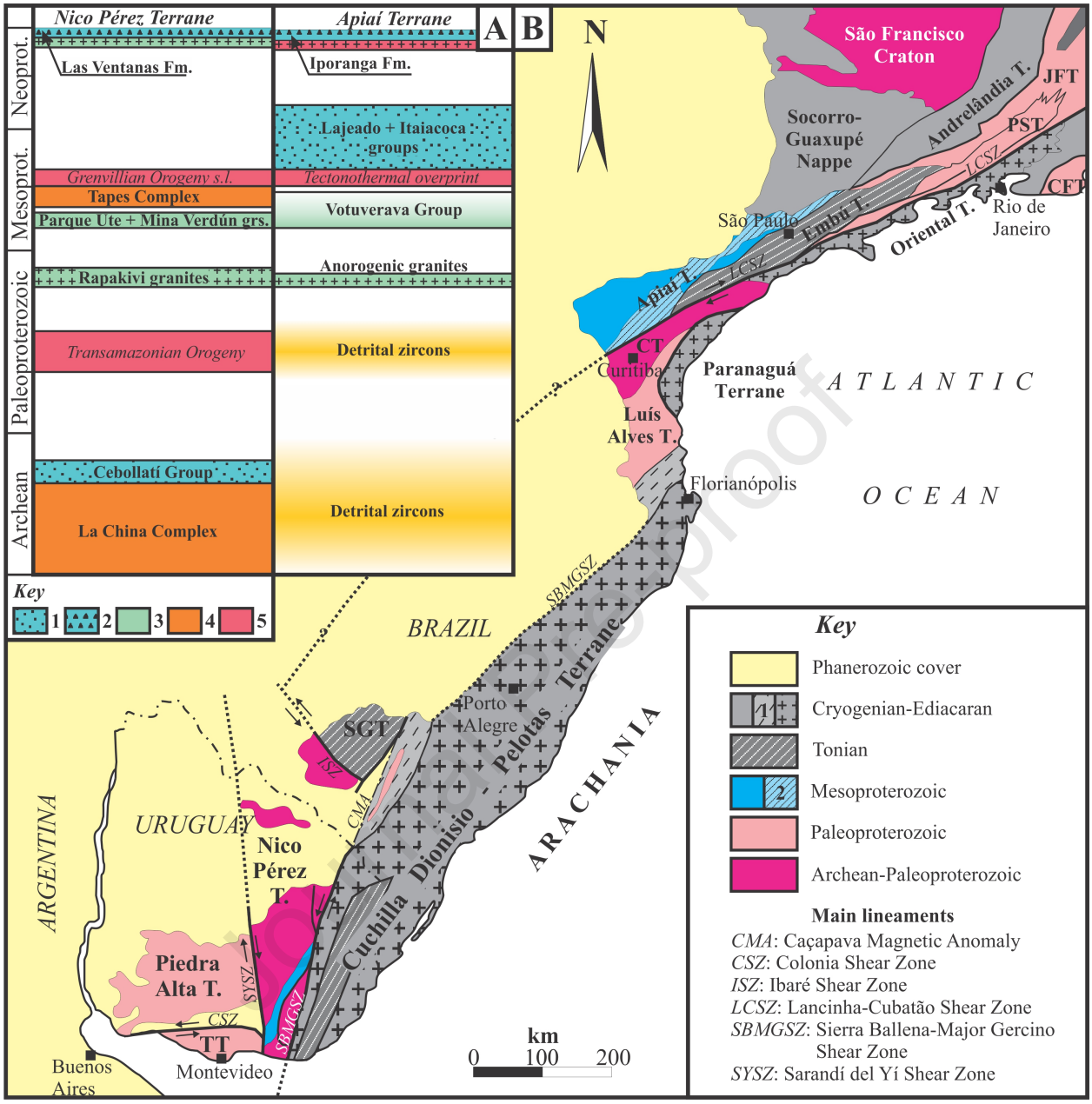
Nico Pérez Terrane
Apiaí Terrane
A
B
Neoprot.
Mesoprot.
Paleoproterozoic
Archean
Las Ventanas Fm.
Iporanga Fm.
Lajeado + Itaiacoca groups
Grenvillian Orogeny s.l.
Tectonothermal overprint
Tapes Complex
Votuverava Group
Parque Ute + Mina Verdún grs.
Anorogenic granites
Rapakivi granites
Transamazonian Orogeny
Detrital zircons
Cebollatí Group
La China Complex
Detrital zircons
Key
1
2
3
4
5
N
São Francisco Craton
Socorro-Guaxupé Nappe
Andrelândia T.
JFT
PST
LCSZ
CFT
São Paulo
Embu T.
Oriental T.
Rio de Janeiro
Apiaí T.
LCSZ
CT
Curitiba
Paranaguá Terrane
Luís Alves T.
Florianópolis
ATLANTIC
OCEAN
BRAZIL
SBMGSZ
Porto Alegre
SGT
ISZ
CMA
Pelotas Terrane
ARACHANIA
URUGUAY
Nico Pérez T.
Dionisio Cuchilla
ARGENTINA
Piedra Alta T.
SYSZ
CSZ
TT
SBMGSZ
Buenos Aires
Montevideo
km
0
100
200
Key
Phanerozoic cover
1
Cryogenian-Ediacaran
Tonian
2
Mesoproterozoic
Paleoproterozoic
Archean-Paleoproterozoic
Main lineaments
CMA: Caçapava Magnetic Anomaly
CSZ: Colonia Shear Zone
ISZ: Ibaré Shear Zone
LCSZ: Lancinha-Cubatão Shear Zone
SBMGSZ: Sierra Ballena-Major Gercino Shear Zone
SYSZ: Sarandí del Yí Shear Zone

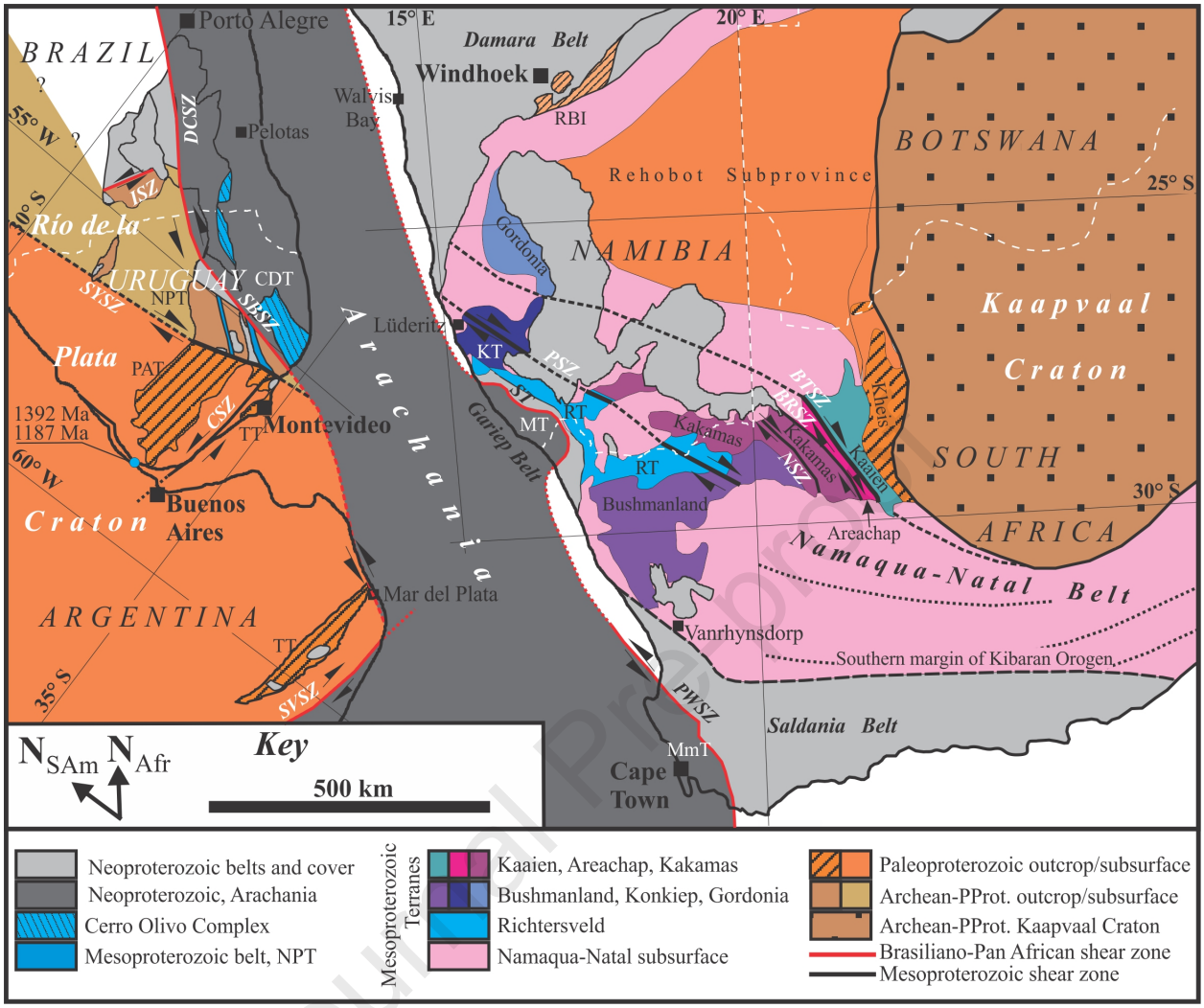

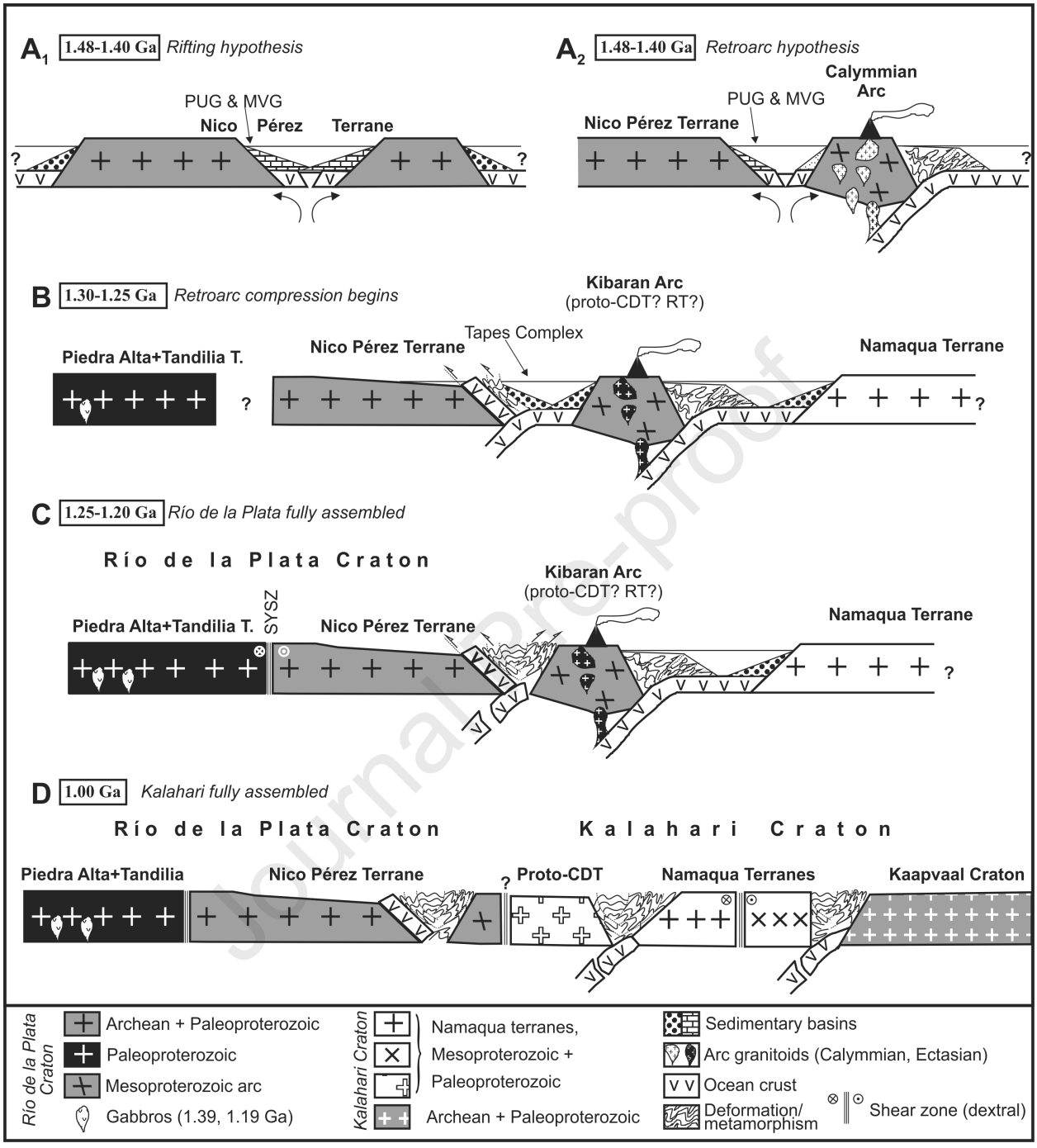

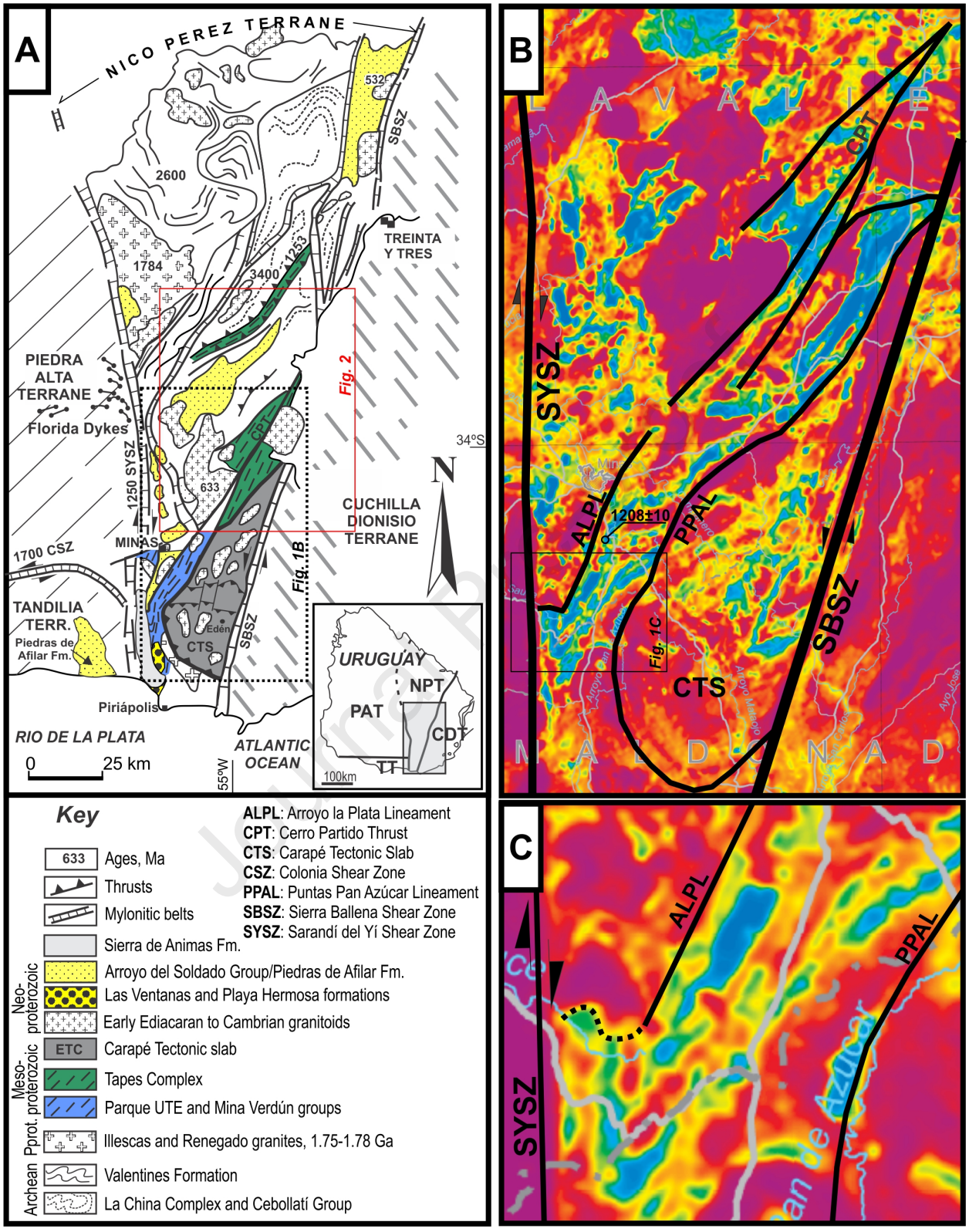
A
NICO PEREZ TERRANE
532
SBSZ
2600
TREINTA
Y TRES
1784
1253
3400
PIEDRA
ALTA
TERRANE
Florida Dykes
Fig. 2
CPT
34°S
N
1250 SYSZ
633
CUCHILLA
DIONISIO
TERRANE
1700 CSZ
MINAS
Fig. 1B
TANDILIA
TERR.
Piedras de
Afilar Fm.
Edén
CTS
SBSZ
URUGUAY
NPT
PAT
CDT
TT
100km
Piriápolis
RIO DE LA PLATA
ATLANTIC
OCEAN
0
25 km
55°W
B
L A V A L L E J A
CPT
SYSZ
ALPL
1208±10
PPAL
SBSZ
Fig. 1C
CTS
M A L D O N A D
C
ALPL
PPAL
SYSZ
Key
633
Ages, Ma
Thrusts
Mylonitic belts
Sierra de Animas Fm.
Arroyo del Soldado Group/Piedras de Afilar Fm.
Las Ventanas and Playa Hermosa formations
Early Ediacaran to Cambrian granitoids
ETC
Carapé Tectonic slab
Tapes Complex
Parque UTE and Mina Verdún groups
Illescas and Renegado granites, 1.75-1.78 Ga
Valentines Formation
La China Complex and Cebollatí Group
Neo-proterozoic
Meso-proterozoic
Pprot.
Archean
ALPL: Arroyo la Plata Lineament
CPT: Cerro Partido Thrust
CTS: Carapé Tectonic Slab
CSZ: Colonia Shear Zone
PPAL: Puntas Pan Azúcar Lineament
SBSZ: Sierra Ballena Shear Zone
SYSZ: Sarandí del Yí Shear Zone

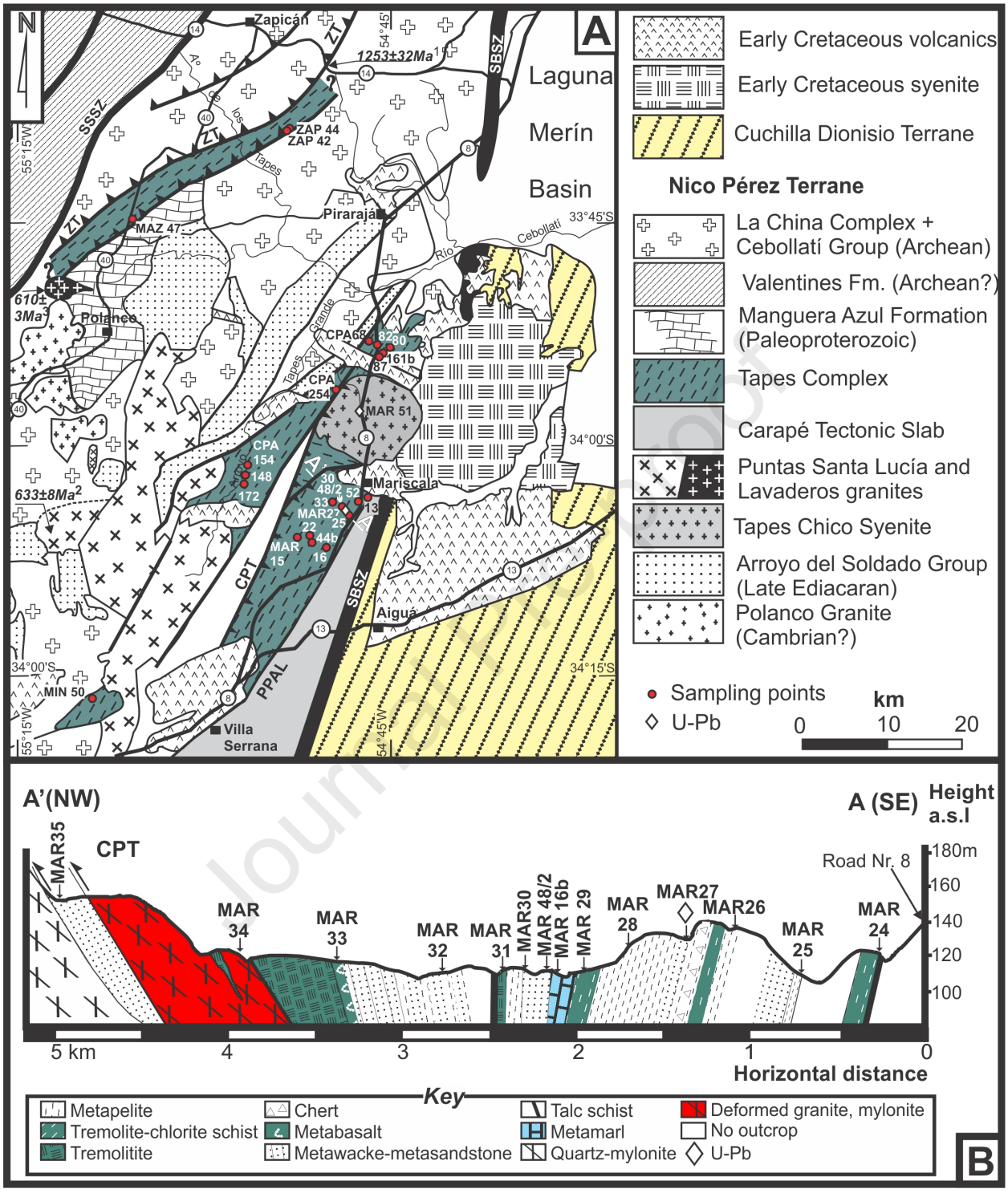
A
Laguna
Merín
Basin
Zapicán
1253±32Ma
SBSZ
SSSZ
ZT
ZAP 44
ZAP 42
MAZ 47
610±3Ma
Polanco
Piraraja
Cebollatí
Río
CPA68
82
80
161b
87
CPA 4254
MAR 51
CPA 154
148
172
633±8Ma
30
48/2
52
33
MAR27
22
25
44b
MAR 15
16
13
Mariscala
CPT
Aiguá
PPAL
MIN 50
Villa Serrana
Tapes
Arroyo Grande
33°45'S
34°00'S
34°15'S
55°15'W
54°45'W
Early Cretaceous volcanics
Early Cretaceous syenite
Cuchilla Dionisio Terrane
Nico Pérez Terrane
La China Complex + Cebollatí Group (Archean)
Valentines Fm. (Archean?)
Manguera Azul Formation (Paleoproterozoic)
Tapes Complex
Carapé Tectonic Slab
Puntas Santa Lucía and Lavaderos granites
Tapes Chico Syenite
Arroyo del Soldado Group (Late Ediacaran)
Polanco Granite (Cambrian?)
Sampling points
U-Pb
km
0
10
20
A'(NW)
A (SE)
Height a.s.l
MAR35
CPT
MAR 34
MAR 33
MAR 32
MAR 31
MAR30
MAR 48/2
MAR 16b
MAR 29
MAR 28
MAR27
MAR26
MAR 25
MAR 24
Road Nr. 8
180m
160
140
120
100
5 km
4
3
2
1
0
Horizontal distance
Key
Metapelite
Tremolite-chlorite schist
Tremolitite
Chert
Metabasalt
Metawacke-metasandstone
Talc schist
Metamarl
Quartz-mylonite
Deformed granite, mylonite
No outcrop
U-Pb
B

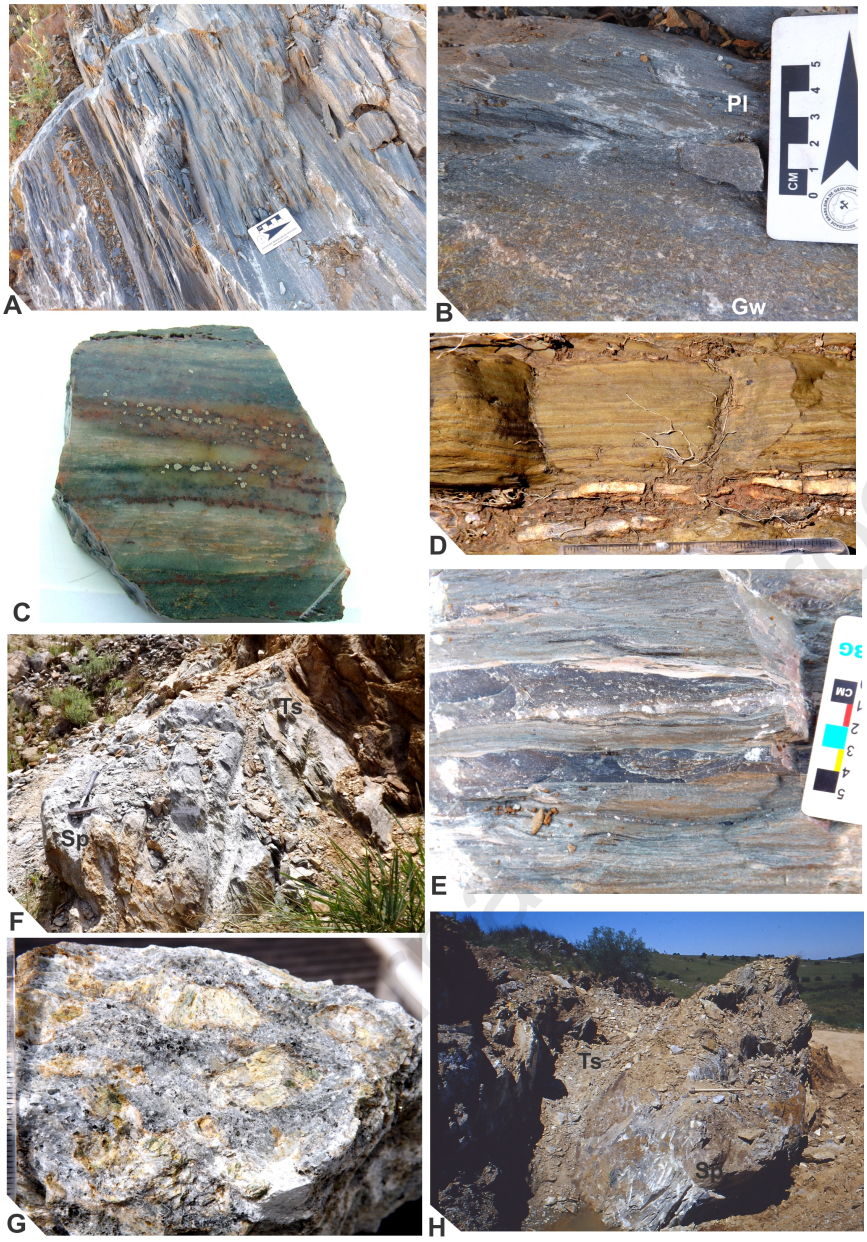

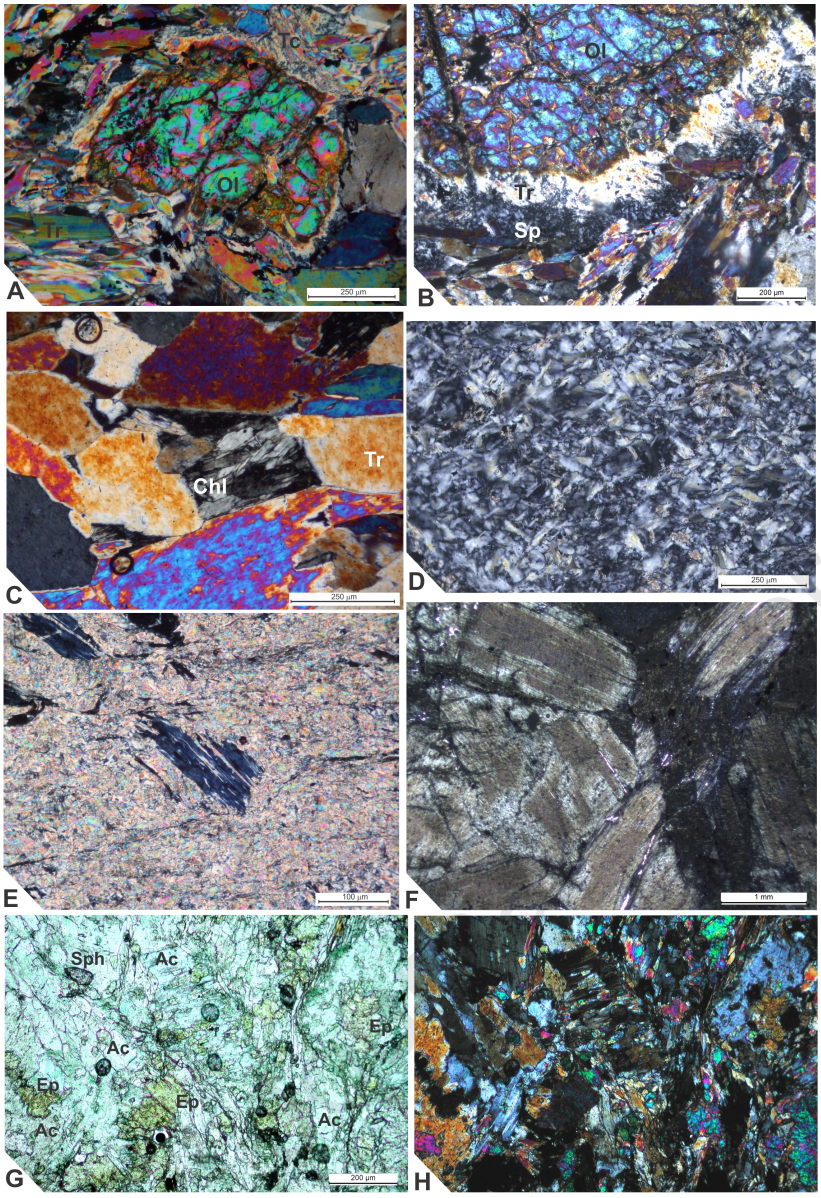
A
Tc
Ol
Tr
250 µm
B
Ol
Tr
Sp
200 µm
C
Chl
Tr
250 µm
D
250 µm
E
100 µm
F
1 mm
G
Sph
Ac
Ac
Ep
Ep
Ep
Ac
Ac
200 µm
H

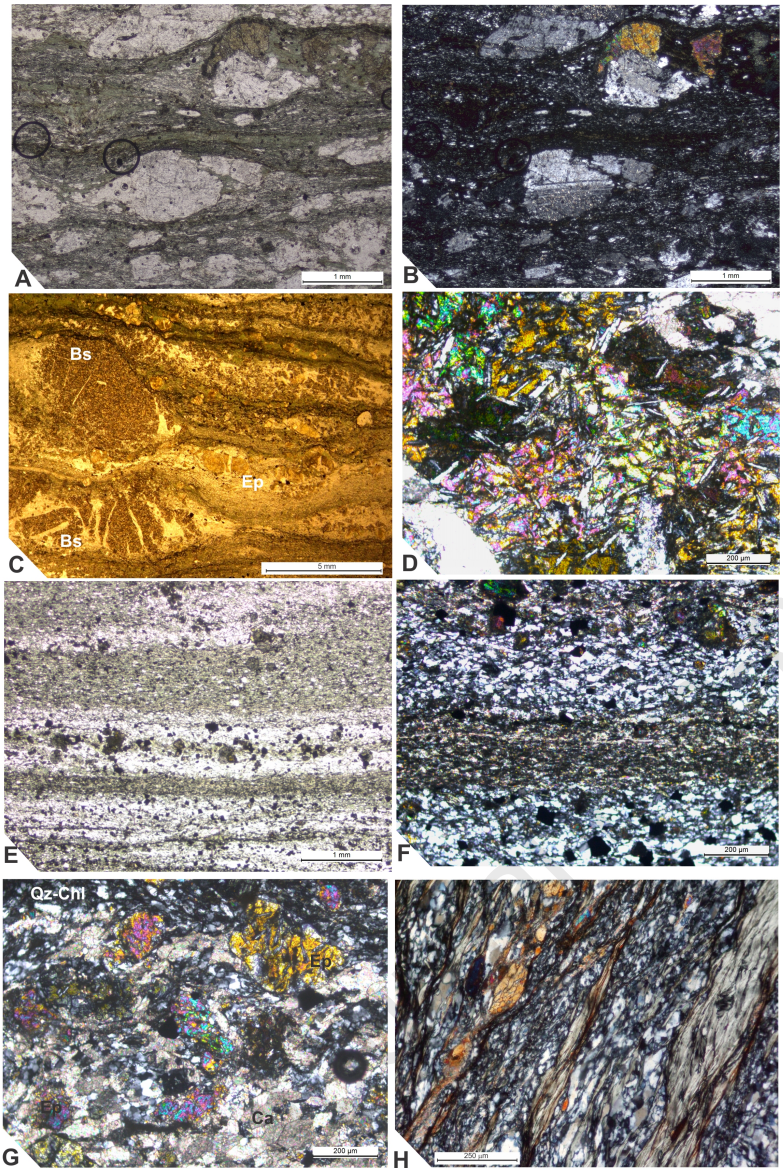
A
1 mm
B
1 mm
Bs
Ep
Bs
C
5 mm
D
200 µm
E
1 mm
F
200 µm
Qz-Chl
Ep
Ep
Ca
G
200 µm
H
250 µm

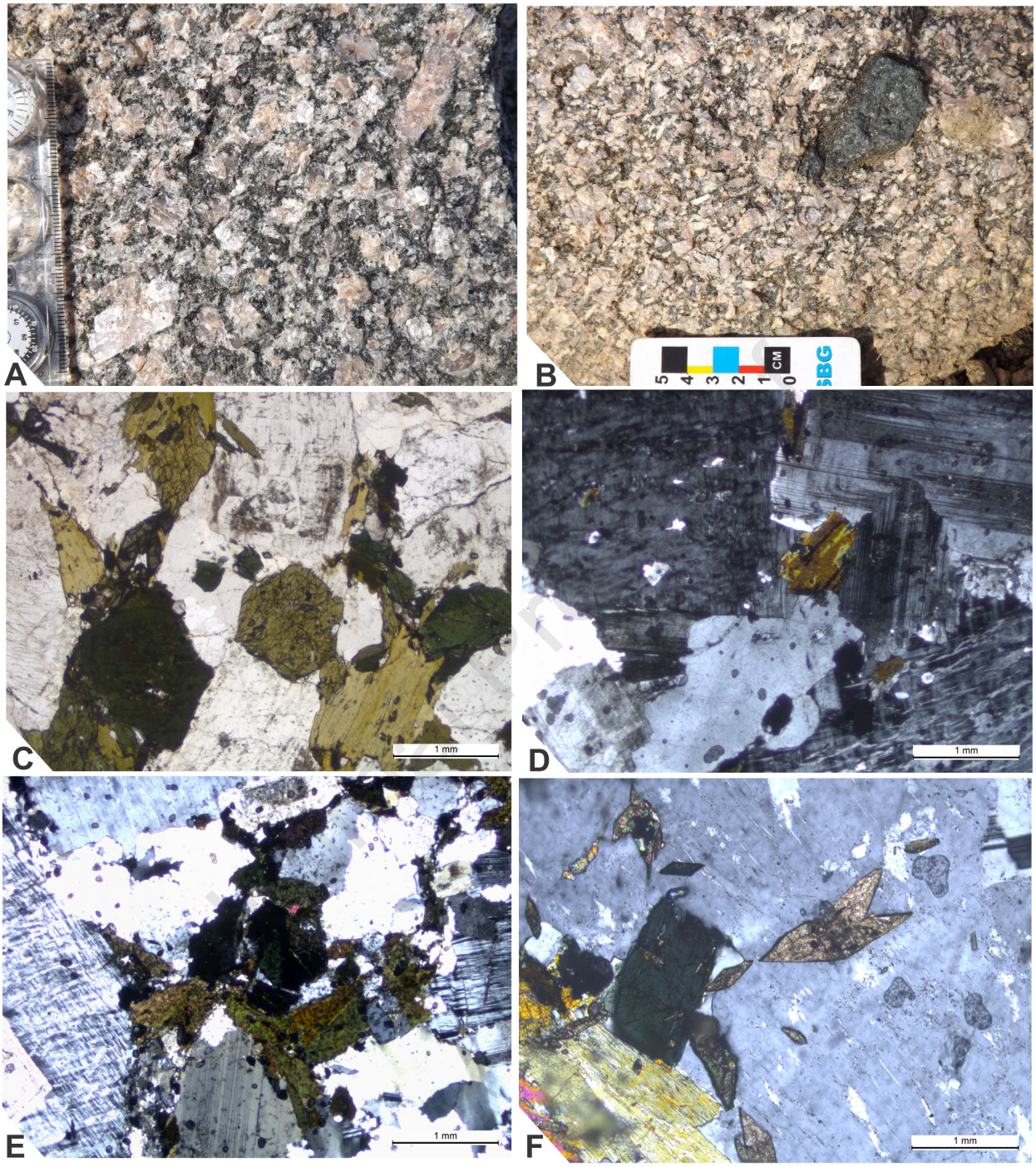
A
B
5 4 3 2 1 0 CM
IBG
C
1 mm
D
1 mm
E
1 mm
F
1 mm

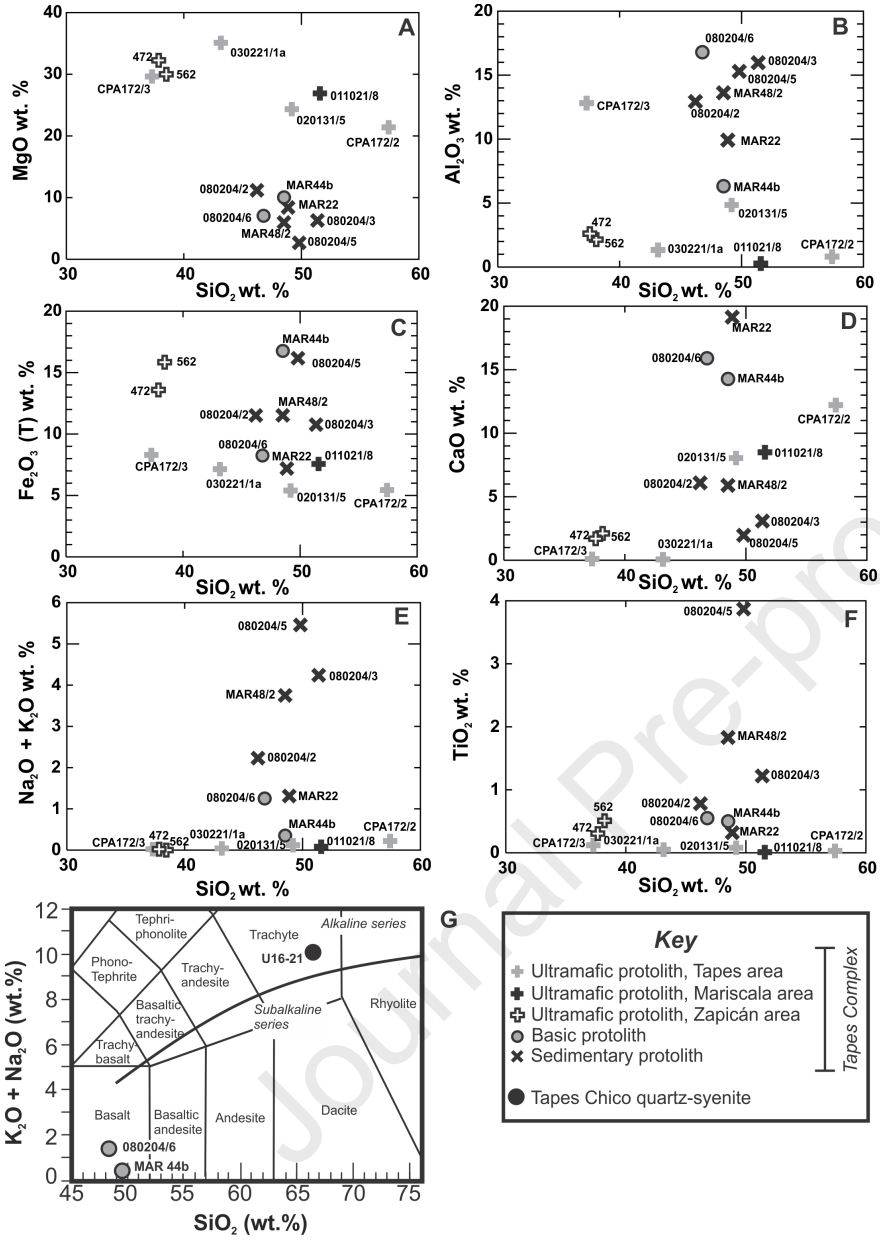

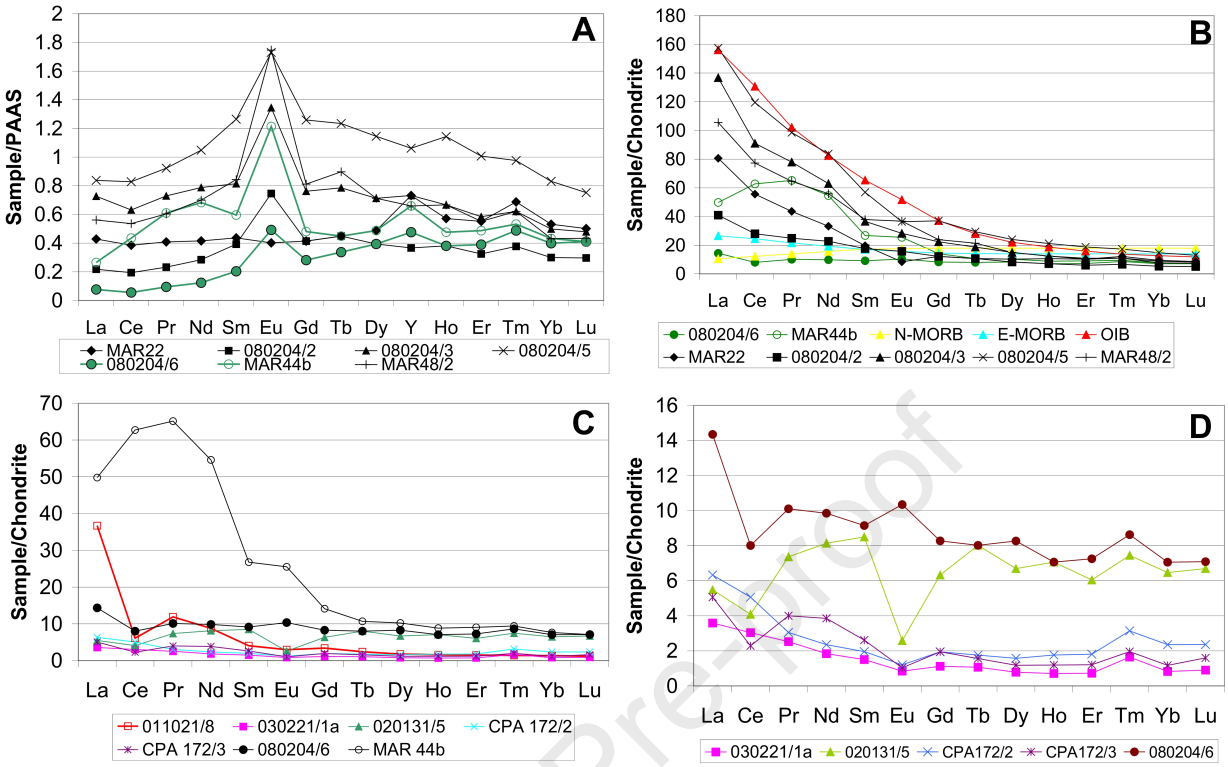

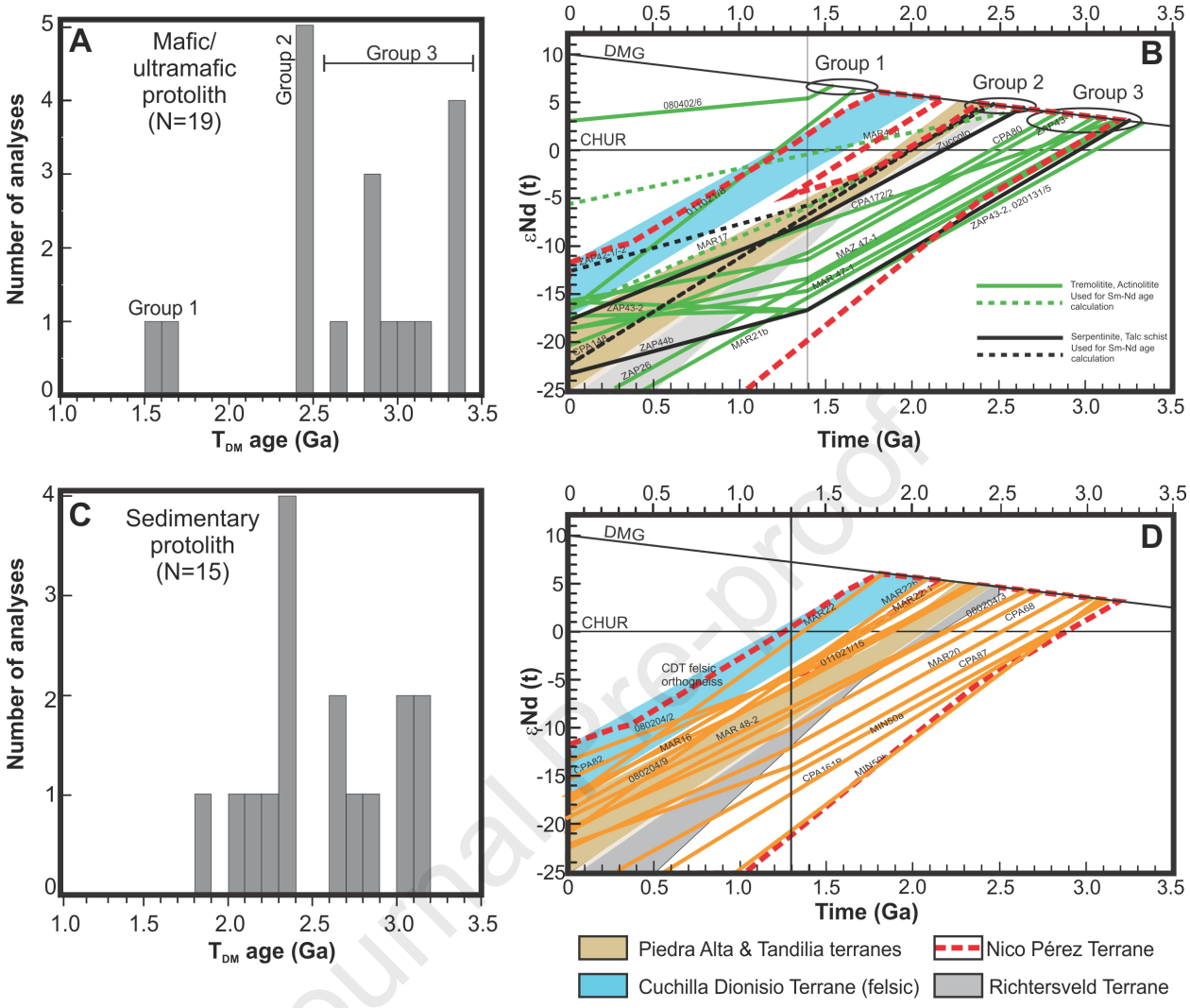

Highlights

- Mesoproterozoic siliciclastic-ultramafic belt bordering the Río de la Plata Craton
- Deposition in a retroarc foreland basin between 1.36-1.25 Ga
- Provenance from an active, ophiolite-bearing Kibaran orogen and Archean rocks
- Affinities with Namaqua terranes of the Kalahari Craton
- New insights into the accretion of Río de la Plata and Kalahari cratons to Rodinia

Declaration of interests

☒ The authors declare that they have no known competing financial interests or personal relationships that could have appeared to influence the work reported in this paper.

☐The authors declare the following financial interests/personal relationships which may be considered as potential competing interests: